

**Studies on New Self-assembled Structures**  
**Created by ABC Linear Triblock Terpolymers**  
**with Composition Distribution**

組成分布を持つ線状 ABC 3 元ブロック共重合体が  
作る新規構造に関する研究

*A Dissertation Submitted to Nagoya University  
for the Partial Fulfillment of the Requirement of  
the Degree of Doctor of Philosophy  
in the Department of Applied Chemistry*

**Yusuke Asai**

浅井 裕介

March 2017



## **TABLE OF CONTENTS**

### **CHAPTER 1.**

#### **General Introduction**

- 1.1 Introduction
- 1.2 Outlines
- 1.3 References

### **CHAPTER 2.**

#### **Synthesis and Characterization**

- 2.1 Synthesis of ISP triblock terpolymers
- 2.2 Characterization and analysis
  - 2.2.1 Size Exclusion Chromatography
  - 2.2.2 Nuclear Magnetic Resonance Spectroscopy
  - 2.2.3 Osmometry
  - 2.2.4 Differential Scanning Calorimetry
  - 2.2.5 Transmission Electron Microscopy
  - 2.2.6 Electron Tomography
  - 2.2.7 Small Angle X-ray Scattering
  - 2.2.8 Microbeam Small Angle X-ray Scattering
- 2.3 References

### **CHAPTER 3.**

#### **Formation of Tetragonally-Packed Rectangular Cylinders from ABC Block Terpolymers Blends**

- 3.1 Introduction
- 3.2 Experiments and Measurements
- 3.3 Results and Discussion
- 3.4 Conclusion
- 3.5 References

**CHAPTER 4.**

**Creation of Cylindrical Morphologies with Extremely Large Oblong Unit  
Lattices from ABC Block Terpolymer Blends**

- 4.1 Introduction
- 4.2 Experiments and Measurements
- 4.3 Results and Discussion
- 4.4 Conclusion
- 4.5 References

**CHAPTER 5.**

**Asymmetric Double Tetragonal Domain Packing from ABC Triblock  
Terpolymer Blends with Chain Length Difference**

- 5.1 Introduction
- 5.2 Experiments and Measurements
- 5.3 Results and Discussion
- 5.4 Conclusion
- 5.5 Appendix
- 5.6 References

**CHAPTER 6.**

**Tricontinuous Double Diamond Networks from Binary Blends of ABC Triblock  
Terpolymers**

- 6.1 Introduction
- 6.2 Experiments and Measurements
- 6.3 Results and Discussion
- 6.4 Conclusion
- 6.5 Appendix
- 6.6 References

Contents

**CHAPTER 7.**

Summary

List of Publications

Acknowledgement



# CHAPTER 1

## General Introduction

### 1.1 Introduction

Polymers or macromolecules consisting of many repeated subunits, have been deeply associated with human beings. Many classes of living organisms such as phospholipids, DNA and proteins are composed of polymers, while some other materials such as wool, cellulose, rubber, plastics, silicone and so on, are also well-known as polymers. Basically they are divided into two categories; “natural polymers” and “synthetic polymers”. Living organisms, wool and cellulose which can be naturally produced in living bodies are included into a classification of “natural polymers”, while nylon, Teflon, Bakelite are good examples of “synthetic polymers” which are synthesized by scientists and engineers. Synthetic polymers have a relatively shorter history than natural polymers. In the mid-1800s, Charles Goodyear accidentally produced a vulcanized rubber by allowing a mixture of pre-rubber and sulfur to touch a stove. Since then, many commercial polymers such as artificial silk (1883), Bakelite (1907), Neoprene (1930) and Nylon (1935) were developed turn by turn. However, the “too high molecular weight” substances had been recognized as “colloids” or associated molecules until 1920s when Hermann Staudinger proposed the concept of polymers in the sense we use today.<sup>1</sup> Although he had a hard time, his new concept brought the great expansion of the polymer science later in the 20<sup>th</sup> century. Now, polymer is recognized as one of the three major materials present in our modern environment along with metal and ceramics. Although polymer is the most familiar material for human beings in nowadays, the development of polymer science is undoubtedly the latest. Polymer science has been developed with the

## Chapter 1

advance in synthetic technology.

As early as 1910s, the original concept of anionic polymerization was first proposed by some researchers in Germany.<sup>2,3</sup> In 1929, Karl Ziegler reported that anionic polymerization of diene initiated with sodium or lithium metal occurred without chain transfer or termination.<sup>4</sup> Although several other studies on the anionic polymerizations of vinyl monomers were reported in the late 1940s, Michael Szwarc first developed the living anionic polymerization in 1956.<sup>5,6</sup> Szwarc used sodium naphthalenide as an initiator for the polymerization of styrene in tetrahydrofuran (THF) and found that the initiation occurs via electron transfer from the sodium naphthalenide radical anion to styrene monomer, where the styryl radical anion forms upon addition of an electron from the initiator so as to create a dianion. For living anionic polymerization, the reactive site is remarkably stable, followed by occurring the propagation by the controlled sequential addition of monomers. Owing to this stability, termination of growing chains and side reactions are practically negligible. This technique has been widely used all over the world and the progress of the synthetic technique has grown up the scientific interest for polymeric materials.

### **1.2 Self-assembly of block copolymers**

“Block copolymer” is one of the fascinating research targets because of highly useful properties, including the wide variety of morphologies in the condensed ordered state, rheological properties related to the morphology and the responses to the external fields. A block copolymer is a polymer containing two or more distinct monomer segments. The simplest architecture among many block copolymers is the linear AB diblock copolymer. When the two distinct blocks are thermodynamically incompatible, covalent bonding between the distinct chains prevents macrophase separation, instead causes microphase separation which gives periodic structures with mesoscopic length scales. A first experimental report on

## Chapter 1

microphase separated structures of block copolymers with clear electron transmission micrographs was presented by Matsuo *et al.* in 1969,<sup>7</sup> where they presented that poly(styrene-*b*-butadiene) (SB) block copolymers form several featured structures depending on their volume fractions. In 1980, Leibler demonstrated the morphological phase diagram of the model AB diblock system based on the mean-field theory.<sup>8</sup> In his theory, there are two major variables to control the phase behavior: one is  $\chi N$  where  $\chi$  is the Flory Huggins parameter characterizing A-B interactions, and  $N$  is the degree of polymerization and the other is the volume fraction  $\phi_A$  ( $=1-\phi_B$ ). According to the regular solution theory, the Flory-Huggins parameter  $\chi$  is represented by

$$\chi = \frac{V}{RT} (\delta_A - \delta_B)^2 \quad (1-1)$$

where  $V$  is the segment volume,  $R$  is the gas constant, and  $\delta_i$  ( $i=A$  or  $B$ ) is the Hildebrand solubility parameter. In practice,  $\chi$  has the temperature dependence,

$$\chi = \frac{\alpha}{T} + \beta \quad (1-2)$$

In eq.(1-2), increasing  $\chi$  means a reduction of A-B contacts. If  $N$  is sufficiently large, phase separation may be accomplished with some loss of translational and configurational entropy by local compositional ordering. The  $\chi N$  controls the order/disorder state of block copolymers, and for a symmetric diblock copolymer system ( $\phi_A=0.5$ ), the order-disorder transition (ODT) is predicted to occur at  $(\chi N)_{\text{ODT}} \doteq 10.5$ , as shown in Figure 1.1.

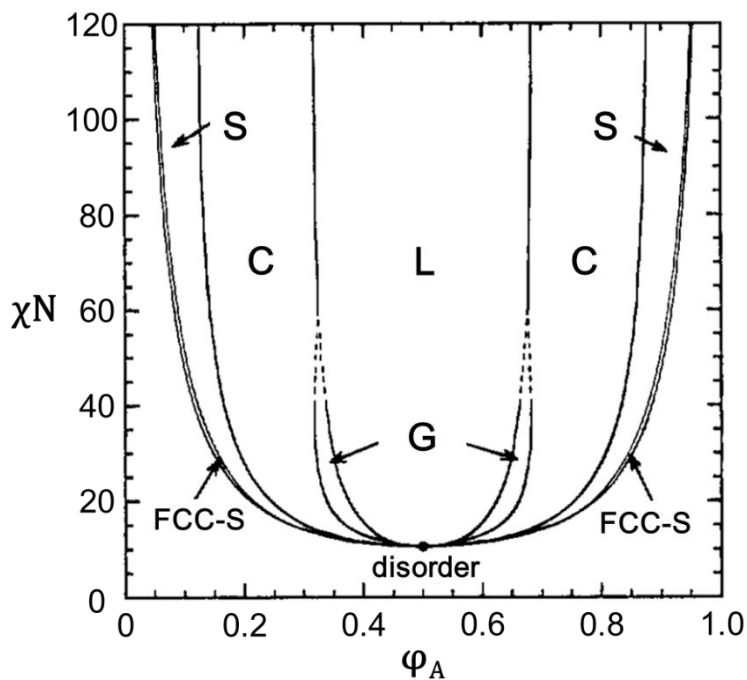


**Figure 1.1** Morphological Phase diagram of diblock copolymers. Reproduced from Matsen.<sup>9</sup>

S: spherical structure, C: cylindrical structure, G: gyroid phase, L: lamellar structure.

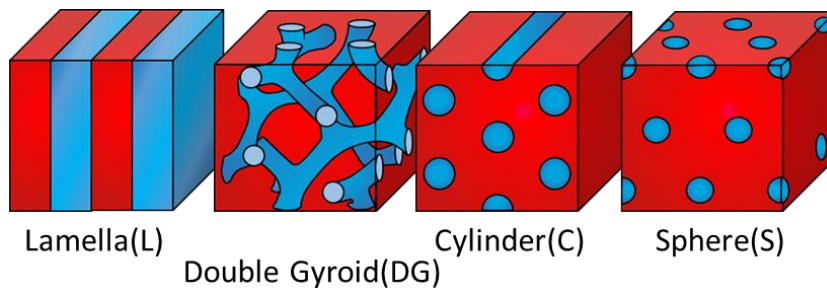


**Figure 1.2** Representative four microphase-separated structures in diblock copolymers.

The other principal parameter,  $\phi$ , determines the particular microphase separated structure in an ordered phase. Leibler anticipated that three microstructures should be obtained by varying  $\phi$  in the strong segregation limit: lamellae (L), hexagonally-packed cylinders (C) and spheres with BCC lattice (S) as described in Figure 1.2.<sup>8</sup> Later, the cocontinuous structures such as the double gyroid (DG) and the double diamond (DD) phases were found at composition between L and C as equilibrium structures.<sup>10,11</sup> However, the double diamond

## Chapter 1

structure was turned out not to be a thermodynamically-stable one after intensive structure analysis.<sup>12-15</sup> In the past, a large number of studies on the morphological features of AB diblock copolymers have been conducted experimentally and theoretically<sup>7-37</sup>, and hence there are a large amount of accumulation concerning the technique, knowledge and know-how of the sample preparation and structure analysis. They intensify the recent application studies of block copolymers.<sup>26,29,38-41</sup>

Even more complex but fascinating self-assembled structures are obtained from block copolymers with more than two block types, e.g. ABC, ABCA, ABCD and non-linear molecular architecture such as ABC star-shaped polymers. These block copolymers have been widely investigated experimentally and theoretically by many researchers.<sup>42-75</sup> Especially, ABC triblock terpolymers are the most well studied multicomponent block copolymer system. By merely adding the third component to AB diblock copolymer, the complexity and variety of the morphology significantly increase. For example, core-shell morphologies of cylinders, spheres and gyroid, perforated lamellae and orthorhombic network structures etc. have been obtained.<sup>71-75</sup> This variety was due to the fact that the middle B block in linear ABC triblocks has to possess a bridge conformation between A and C components when the endblocks are immiscible pairs. Furthermore, the addition of one block increases the morphological parameters; three interaction parameters ( $\chi_{AB}$ ,  $\chi_{BC}$ ,  $\chi_{AC}$ ), volume fractions ( $\phi_A$ ,  $\phi_B$ ,  $\phi_C$ ), and block sequences (ABC, ACB, BAC). Here some examples of the morphological transitions depending on the parameters are displayed and compared.

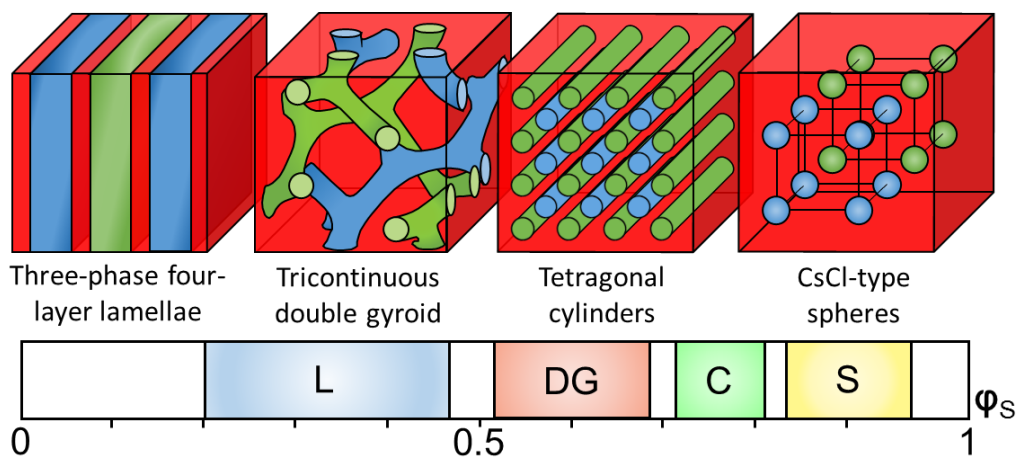


**Figure 1.3** Morphologies for symmetric ABC linear triblock terpolymers with non-frustrated system. Reproduced from Ref[25].

As a model ABC triblock terpolymer system,  $\chi_{AB} \sim \chi_{BC} < \chi_{AC}^*$ , where the A/C interface does not exist, Matsushita and coworkers systematically explored the phase map with the symmetric end block components ( $\phi_A = \phi_C$ ).<sup>25,76</sup> They synthesized poly(isoprene-*b*-styrene-*b*-2-vinylpyridine)(ISP) triblock terpolymers via living anionic polymerizations and hence the polymers used in their studies were highly monodisperse. By varying the  $\phi_S$ , ISP triblock terpolymers developed three-phase four-layer lamellae, ordered tricontinuous double gyroid (OTDG), tetragonal-packed cylinders and CsCl-type spheres (Figure 1.3). All these structures have been categorized as a series of “super lattice structures”, where two microdomains, i.e., I and P domains are exchangeable. However, it should be pointed out here that a new cylinder arrangement appeared. This is due to the present symmetric molecular design. In short, a tetragonal-packing of alternating A and C cylinders in an ABC triblock terpolymer is more favorable than a hexagonal one. Needless to say, the tetragonal packing does not fill space well, but in reality the system chose this arrangement so as to guarantee domain symmetry by sacrificing domain packing efficiency accompanied by conformational entropy loss of centered S chain. As a result, the frustration on the entropy of bridging chains reduces the

cylinder region in the phase map and enlarges the OTDG region.<sup>77</sup> As for the other ABC triblock terpolymers such as poly(butadiene-*b*-styrene-*b*-2-vinylpyridine) (PB-PS-PVP) and poly(methyl methacrylate-*b*-styrene-*b*-butadiene) (PMMA-PS-PB) by Abetz and co-workers,<sup>72,78</sup> and poly(isoprene-*b*-styrene-*b*-ethylene oxide) (PI-PS-PEO) by Epps and coworkers<sup>79-81</sup>, the phase behaviors partly analogous to that of the ISP system were presented. Theoretical calculations were also performed for non-frustrated ABC triblock terpolymers<sup>58,59,77,82</sup>, which will be explained below, and provides complete phase triangles as shown in Figure 1.4. The relative locations of each structure in the triangle agree reasonably well with experimental results.

\*The present terpolymer system possessing the condition,  $\chi_{AB} \sim \chi_{BC} < \chi_{AC}^*$ , is sometimes called “non-frustrated” system in the sense opposed to “frustrated” system explained on the next paragraph, where the condition;  $\chi_{AB}$  or  $\chi_{BC} \gg \chi_{AC}$ , holds.

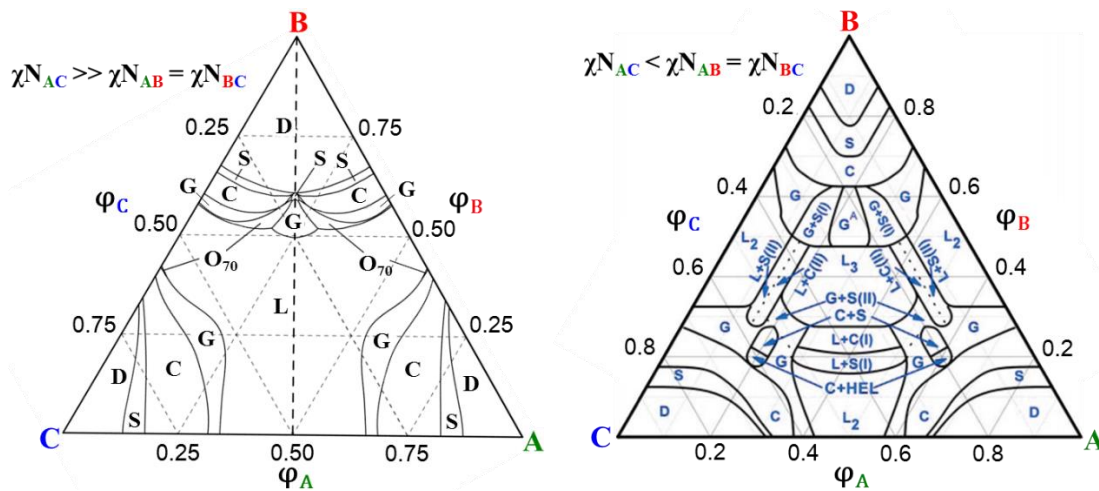


**Figure 1.4** Comparison of phase triangles between non-frustrated system (left) and frustrated system (right). Reproduced from Ref[82,84].

For frustrated ABC triblock terpolymers ( $\chi_{AB}$  or  $\chi_{BC} \gg \chi_{AC}$ ), A/C contacts can be adopted even though the two blocks are not covalently connected. The favorability of creating

A/C interfaces can stem from high incompatibility of the covalently-connected blocks relative to the outer blocks. The interfaces lead to more complex morphological behaviors than those of the corresponding non-frustrated systems. Experimentally, a number of frustrated systems have been investigated by adopting poly(styrene-*b*-butylene-*b*-methyl methacrylate) (SBM)<sup>85,86</sup>, poly(styrene-*b*-2-vinylpyridine-*b*-tert-butyl methacrylate) (SVT)<sup>87,88</sup> and poly(styrene-*b*-butadiene-*b*-caprolactone) (SBC)<sup>89</sup>. These terpolymers have developed a lot of complex structures including helices-on-cylinders, knitting patterns, spheres-on-spheres and so on. Besides on the experimental works, the self-assembly of the frustrated systems has been investigated by theoretical simulations,<sup>58-60,84,90</sup> whose results are reasonably well consistent with many of the experimental observations. The theoretical studies are helpful to understand the self-assembling mechanism of the complex phases and guide experimental studies to create new structures.

### 1.3 Polydispersity effect on morphology

Now going back to the basic nature of block copolymers. Block copolymers are generally characterized by molecular weights, volume fractions and polydispersities; of course the segment lengths, crystallinity, interaction parameters are each one of the important parameters to determine the static and dynamic properties. However, in most of experimental and theoretical researches, the effect of polydispersity was not carried out much. Naturally, if not all, synthetic polymers are polydisperse. It is expected that a high polydispersity significantly influences the static and dynamic properties because many of the properties depend on their chain lengths. Traditionally, anionic polymerization technique has been utilized to synthesize well-defined block polymers with low polydispersity (polydispersity index, PDI, should be lower than 1.1), which is defined as the ratio of weight- to number-average molecular weight  $M_w/M_n$ . Although the anionic polymerization is still a very attractive

and effective approach under control, it requires time and efforts to attain air- and water-free reaction conditions. Recent considerable efforts in synthetic chemistry over the past three decades have achieved the great success of “living” radical polymerizations: atom transfer radical polymerization (ATRP)<sup>91-93</sup>, reversible addition-fragmentation transfer (RAFT)<sup>94,95</sup> and nitroxide-mediated polymerization (NMP)<sup>96,97</sup>. Although their PDIs typically cover around 1.2-1.4, evidently higher than those synthesized via anionic polymerization, these developments enables the preparation of block copolymers having a wide variety of monomer types under less rigorous reaction conditions than anionic polymerizations. In addition, novel block copolymers with various architectures can be synthesized relatively easily.<sup>98-100</sup> These controlled radical polymerization techniques have received considerable attention because of the economically and industrially viable synthetic conditions.

It is well-known that polydispersity significantly affects the physical properties. Because of the difficulty in synthesizing block copolymers with various PDIs, theoretical studies on the morphological behavior of polydisperse block copolymers were conducted ahead of the experimental studies. To my knowledge, in 1989, Brishtein and coworkers first reported a theoretical study of superstructures of block copolymers, taking into account of polydispersity<sup>101</sup>, followed by another 4 papers of this series.<sup>102-105</sup> Although the “polydisperse” in their systems was introduced by “binary blends” of monodisperse block copolymers, their studies are consistent well with experimental data. Hadziioannou and Skoulios demonstrated that lamellar microdomain distance ( $D$ ) in polydisperse block copolymers (PDI:1.1~1.3) does not follow the relationship<sup>106</sup>:  $D \sim M^{2/3}$  where  $M$  denotes the total molecular weight of the copolymer<sup>30,31,107</sup> but the dependence of  $D$  on  $M$  becomes steeper, which earns to higher value of the exponent than  $2/3$ . Their study must be the first report that revealed the polydispersity effect on the domain periodicity, unfortunately, they did not fully mention the “polydispersity effect”. Theoretical studies on the morphologies of polydisperse block copolymers, which are

not “binary blend” systems, have been conducted by many researchers.<sup>108-115</sup> Their studies provided three main conclusions; (1) Polydispersity causes a significant increase in the domain spacing. (2) Increase in polydispersity shifts phase boundaries towards larger  $\phi$ . (3) Polydispersity caused the order-disorder transition (ODT), where  $(\chi N)_{\text{ODT}}$  depends on the compositions. These effects are well accounted by theoretical approaches. Figure 1.5 and 1.6 provide the simple intuitive illustrations for two perturbations introduced by polydispersities, (1) and (2) mentioned above.

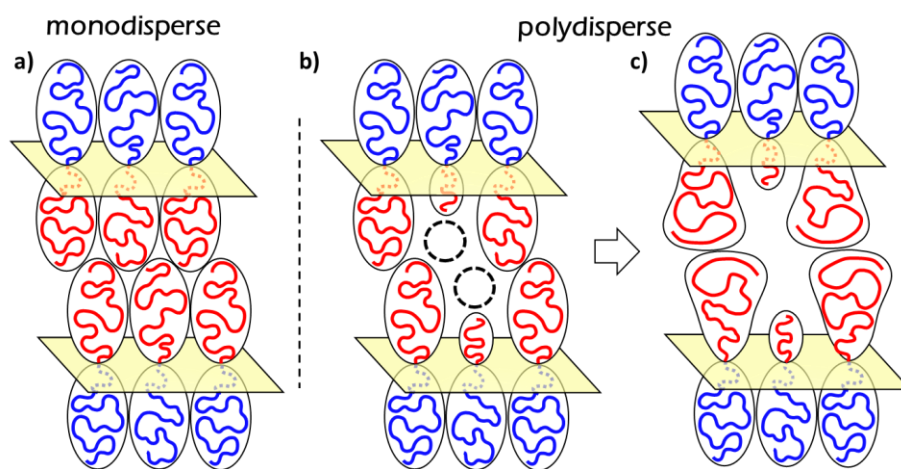


**Figure 1.5** Schematic representation of the mechanism of enlargement of domain thickness by introducing polydispersity. (a) shows the chain conformation of monodisperse AB diblock copolymers within lamellar phase, while (b) and (c) explain the reason for the chain stretching of longer blocks to efficiently fill space.

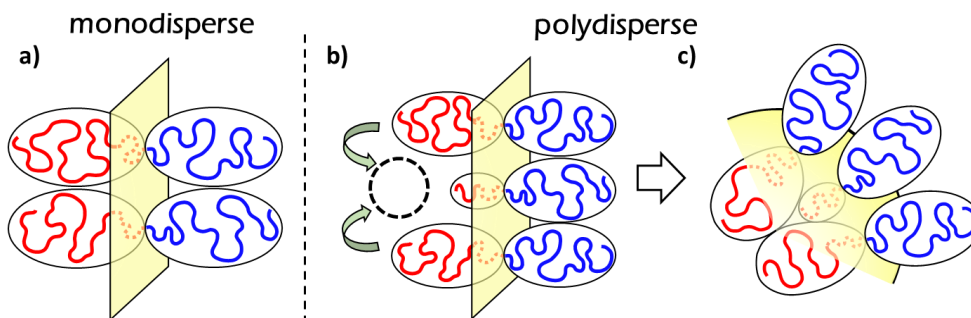


**Figure 1.6** Schematic representation of the mechanism of the morphological transition by polydispersity.

## Chapter 1

introducing polydispersity. (a) shows the chain conformation of monodisperse AB diblock copolymers, while (b) and (c) explains the reason for the transition in which the interface curves toward the polydisperse blocks because shorter blocks cannot fill the space.

(1) The rationale for the increase in domain spacing can be understood by the idea of releasing the stretching entropy of the polydisperse chains. The existence of long and short chains can induce the chain localization where long chains fill the center of the microdomains.

(2) The mechanism of the morphological transition is explained by the competition between interfacial and entropic energies. For polydisperse systems, the component chains with larger polydispersity stretch more than those without polydispersity even though the blocks have the equal compositions. The imbalance of stretching energy between opposing blocks curves the interface concave toward the component with the lower polydispersity to alleviate the imbalance and relax the stretching energy of the polydisperse component.

Lynd and Hillmyer systematically studied the effects of polydispersity on the morphological behavior by a model experiment using AB diblock copolymers comprised of a monodisperse A block and a variable polydisperse B block.<sup>114, 116-118</sup> These polymers were synthesized via a combination of living anionic polymerization and ring-opening polymerization. Their intensive studies produced the three conclusion as mentioned above. Later, Hillmyer expanded the study to the ABC triblock system.<sup>119,120</sup> The polydispersity effects of the systems generally mimic the effects reported in AB diblock copolymers, however, a somewhat different phenomenon appeared due to the chain connectivity. Polydispersity in ABC triblock terpolymers produces a richer phase behavior including core-shell gyroid and *Fddd* network phase. Despite of their efforts, a comprehensive understanding of the morphologies of ABC triblock terpolymers with polydispersity is still lacking because of the synthetic difficulty and large number of parameters.

Blending block copolymers is another effective way to produce polydispersity. Matsushita and coworkers utilized multicomponent blending with monodisperse block copolymers ( $PDI < 1.1$ ) synthesized via living anionic polymerization.<sup>121-125</sup> In fact, their study in 2003 is the first systematic experiment to examine polydispersity effects in block copolymer melts,<sup>121</sup> and the blends of nine polystyrene-*b*-poly(2-vinylpyridine) (SP) diblocks with similar total molecular weights, but with different compositions as depicted in Figure 1.7 were adopted. The blend samples were prepared to be an overall symmetric composition, but different PDI. They revealed that the increase in polydispersity increases the lamellar domain spacing even though the total molecular weight is constant without causing macrophase separation at sufficient high polydispersity. Their systematic studies were also conducted on various types of blend system, the molecular systems were schematically represented in Figure 1.8. Successfully, Matsushita and coworkers investigated the partitioning of block lengths within lamellar domains by neutron reflectivity.<sup>124,125</sup> They prepared selectively deuterated monodisperse SP diblock and PSP triblock copolymers together with undeuterated monodisperse SP and PSP block copolymers. They revealed that longer block chains were localized at the center of the lamellar domains and the shorter block chains remained closer to the interface.

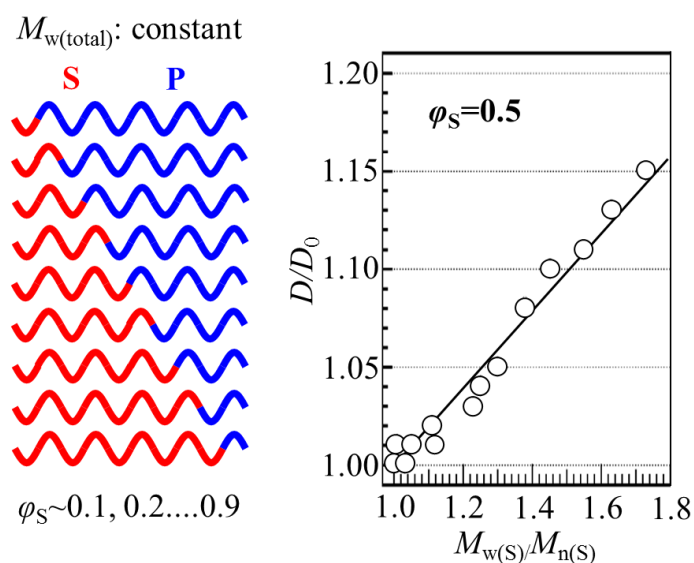


**Figure 1.7** Schematic illustration of the system studied by Matsushita *et al.*<sup>121</sup> Composition distribution dependence of the normalized interfacial thickness for diblock system. Adapted from Ref[121]. Red and blue chains present polystyrene and poly(2-vinylpyridine) components, respectively.

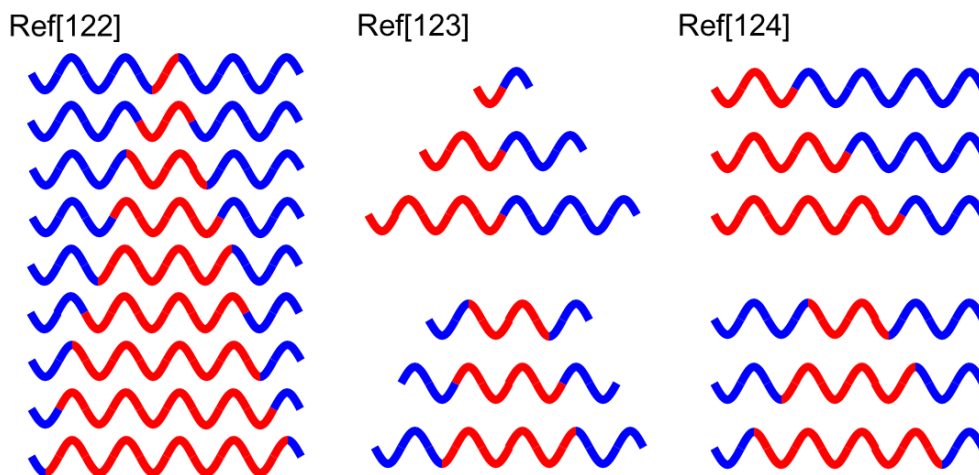


**Figure 1.8** Diagrammatic illustration of systems studied by Noro, Matsushita *et al.*<sup>121-125</sup> Red and blue chains present polystyrene and poly(2-vinylpyridine) components, respectively.

Throughout this section, the effects of “polydispersity” on the morphological behavior of block copolymers were systematically investigated by the intensive experiments from Hillmyer and Matsushita, however there exists considerable difference between their studies. Hillmyer achieved “continuous” distribution by a combination of different synthetic methods, while Matsushita introduced “discrete” distribution by blending monodisperse block copolymers. Studies on the contribution of continuous distribution to physical property has been of growing importance in industry and academic field due to the recent synthesis advance, whereas the studies on block copolymer blends begun in the early 1990’s and interesting phenomena have been found.

## 1.4 Polymer blends including block copolymers

The simplest blend system is the binary blends of AB diblock copolymer and the constituent A (or B) homopolymer. Many experimental<sup>126-134</sup> and theoretical<sup>135-140</sup> studies led to a comprehensive understanding on the phase behavior of the blend systems. The addition of homopolymers is very helpful to tune the composition of block copolymers and furthermore facilitate stabilizing new phases such as perforated lamellae<sup>133</sup> and double diamond structure<sup>134</sup>, which are believed to be a metastable phase in pure diblock copolymers. Addition of a small amount of homopolymers improves grain sizes as well<sup>132</sup>.

The phase behavior strongly depends on the molecular weight of the homopolymer added.<sup>127,128,135</sup> When the molecular weight of the homopolymer is comparable to the constituent block component, a small amount of the homopolymer is miscible in the constituent copolymer domain, but the homopolymers are segregated in the middle of the domains. With decreasing the molecular weight, the block copolymer can contain more homopolymers and they are more uniformly distributed within the domains. When the molecular weights of the homopolymers are much larger than those of the constituent block chains, the homopolymers are excluded from the domains, resulting in macrophase separation. Thus, the homopolymer shorter than the constituent block are required to inspire the interesting phase structures.

The addition of homopolymers becomes more useful for multicomponent block copolymers, more efforts and time being required to synthesize them. A number of characteristic structures have been obtained in the blend systems.<sup>141-146</sup> Besides adding homopolymers into block copolymers, blending block copolymers is another economical and effective method to design new materials.

Especially in the past several decades, binary blends of AB diblock copolymers have received considerable theoretical and experimental attentions.<sup>101-105,149-171</sup> Theoretical

approaches contribute significantly to the understanding of the blend systems since they have a large number of parameters including  $\chi$ , volume fractions of each block copolymer, their molecular weight ratios and the blending ratio. Shi and Noolandi studied the effects of short block chains on the interfacial curvature for long/short AB diblock copolymer binary blends using SCFT simulations.<sup>166</sup> They revealed that the phase behavior can be varied by addition of small amount of the short diblock and that the short block chains segregate to the interface. The segregation means that the long chains always stretch further, being resulted in the morphological transition. Matsen studied binary blends of long and short symmetric AB diblock copolymers.<sup>168</sup> It has been revealed that when the molecular weight ratio exceeds 5, the short and long diblocks become immiscible rather, resulting in a coexistence of a long-lamellar phase and a short-period lamellar or disordered phase. Interestingly, the long-diblock-rich phase contains a substantial amount of short diblocks, while the short-diblock-rich phase is nearly pure. Matsen and Shi studied the phase behavior of binary blends of AB diblock copolymers, where both diblock have the same molecular weight, but possess different compositions.<sup>167,169</sup> They concluded that if the composition of the two blocks are not very different, the simple mixed phase can form, whereas macrophase separation tends to occur when the compositions are quite different.

Experimentally, Hashimoto and coworkers conducted a series of studies on morphological behavior of polystyrene-*b*-polyisoprene (SI) diblock copolymer binary blends.<sup>149-163</sup> They constructed phase diagrams in the parameter of temperature, blending composition and molecular weight ratio of the two constituent diblock copolymers, many achievement are included in them. First, the binary blends exhibit a much richer phase behavior than neat constituent diblocks. Second, binary mixtures give enlarged domain sizes and distances. Third, the phase boundaries are shifted, particularly, ODT phase boundary decreases with increasing the fraction of short diblock. Finally, macrophase separation occurs

## Chapter 1

if the molecular weight ratio exceeds certain value. Interestingly, these results are qualitatively similar to the polydisperse effects as described in the previous section.

Block copolymer blends have expanded to more complicated systems such as ABC/AB, ABC/BC, ABC/AC blends<sup>172-179</sup>, ABC/ABC (BCA) blends<sup>78,180-183</sup>, ABC star/AB blend<sup>184</sup>, BABCB/ABC blend<sup>185</sup>. These specific blends have given a number of interesting morphologies, many of which have never been predicted theoretically. For example, the undulated lamellae was observed in the mixture of three monodisperse ISP triblock terpolymers with the same volume fractions ( $\phi_I, \phi_S, \phi_P \sim 0.33$ ), but with different molecular weights (2.6k, 9.6k, 15k), where, “molecular weight distribution” was actually introduced by blending. The three parent ISP triblocks all created three-phase four-layer lamellar structures with flat surface. By blending the three blocks to keep equal mole fractions of the shortest and longest triblocks, the flat interfaces were transformed into undulated ones where I/S and S/P interfaces are periodically undulated, when PDI exceeds a certain value. It is introduced to know that the “constant mean curvature” policy has been broken to satisfy the requirement for minimization of free energy. Matsushita and coworkers concluded that the loss in displacement entropy permitting weak localization of junction points is smaller than the conformational entropy loss for forming a flat-surface lamellar structure. However, a comprehensive understanding of multicomponent blend system is still lacking because of the cumbersome synthesis.

In this thesis, I have attempted to expand the understanding on the effects of “composition distribution” on the morphology of ABC triblock terpolymers. The composition distribution is introduced by blending ABC triblock terpolymers with constant molecular weights but with different compositions.

## 1.5 Outlines

This thesis covers 4 research topics. Chapter 2 summarizes experimental procedures and structure analysis techniques. In Chapter 3, the effects of composition distribution of ABC linear triblock terpolymers are investigated by blending five ABC triblocks with constant molecular weight and center-block fraction, while different end-block fractions. This system can be considered as a merely “continuous” distribution system. In Chapter 4, binary blends of ABC triblock terpolymers with different chain lengths of the two end-blocks as a function of  $\varphi_C/\varphi_A$  are discussed. The difference in chain lengths of the two-end blocks is the almost the same, that is, symmetric “discrete” composition distribution is adopted. Chapter 5 reports the effects of asymmetric chain length difference of the two-end blocks on the phase behavior. In Chapter 6, the “discrete” distribution is extended to the cocontinuous triply periodic structure region. Finally, Chapter 7 summarizes all the findings obtained in this thesis.

## 1.6 References

1. Staudinger, H. Über Polymerization. *Ber. Dtsch. Chem. Ges.* **1920**, 53, 1073.
2. Schlenk, W.; Thal, A. Über Metallketyle, eine große Klasse von Verbindungen mit dreiwertigem Kohlenstoff. *Ber. Dtsch. Chem. Ges.* **1913**, 46, 2840.
3. Harries, C. Über Kohlenwasserstoffe der Butadienreihe und über einige aus ihnen darstellbare kunstliche Kautschukarten. *Liebigs Ann Chem* **1911**, 383, 213.
4. Ziegler, K.; Colonius, H. Schafer O. Untersuchungen über alkaliorganische Verbindungen II: Zur Kenntnis der Schlenkschen Addition von Alkalimetallen an ungesättigte Kohlenwasserstoffe. *Liebigs Ann Chem* **1929**, 473, 36.
5. Szwarc, M.; Levy, M.; Mikovich, R. Polymerization Initiated by Electron Transfer to Monomer. A New Method of Formation of Block Polymers. *J. Am. Chem. Soc.* **1956**, 78, 2656.
6. Szwarc, M. “Living” Polymers. *Nature* **1956**, 67, 1519.
7. Matsuo, M.; Sagae, S.; Asai, H. Fine Structures of Styrene-Butadiene Block Copolymer Films Cast from Toluene Solution. *Polymer* **1969**, 10, 78-87.
8. Leibler, L. Theory of Microphase Separation in Block Copolymers. *Macromolecules* **1980**, 13, 1602-1617.
9. Matsen, M. W.; Bates, F. S. Unifying Weak- and Strong-Segregation Block Copolymer Theories. *Macromolecules* **1996**, 29, 1091-1098.

## Chapter 1

10. Hasegawa, H.; Tanaka, H.; Yamasaki, K.; Hashimoto, T., Bicontinuous Microdomain Morphology of Block Copolymers. 1. Tetrapod-Network Structure of Polystyrene-Polyisoprene Diblock polymers. *Macromolecules* **1987**, *20*, 1651-1662.
11. Thomas, E. L.; Alward, D. B.; Kinning, D. J.; Martin, D. C. Ordered Bicontinuous Double-Diamond Structure of Star Block Copolymers: A New Equilibrium Microdomain Morphology. *Macromolecules* **1986**, *19*, 2197-2202.
12. Hajduk, D. A.; Harper, P. E.; Gruner, S. M.; Honeker, C. C.; Kim, G.; Thomas, E. L.; Fetters, L. J. The Gyroid: A New Equilibrium Morphology in Weakly Segregated Diblock Copolymers. *Macromolecules* **1994**, *27*, 4063.
13. Matsen, M. W.; Bates, F. S. Origins of Complex Self-Assembly in Block Copolymers. *Macromolecules* **1996**, *29*, 7641-7644.
14. Matsen, M. W.; Bates, F. S. Block copolymer microstructures in the intermediate-segregation regime. *J. Chem. Phys.* **1997**, *106*, 2436.
15. Jinnai, H.; Nishikawa, Y.; Spontak, R. J.; Smith, S. D.; Agard, D. A.; Hashimoto, T. Direct Measurement of Interfacial Curvature Distributions in a Bicontinuous Block Copolymer Morphology. *Phys. Rev. Lett.* **2000**, *84*, 518-521.
16. Inoue, T.; Soen, T.; Hashimoto, T.; Kawai, H. Thermodynamic interpretation of domain structure in solvent-cast films of A-B type. *J. Polym. Sci. Part A-2* **1969**, *7*, 1283-1302.
17. Shibayama, M.; Hashimoto, T.; Kawai, H. Ordered structure in block polymer solutions. 1. Selective solvents. *Macromolecules* **1983**, *16*, 16-28.
18. Hashimoto, T.; Shibayama, M.; Kawai, H. Ordered structure in block polymer solutions. 5. Equilibrium and nonequilibrium aspects of microdomain formation. *Macromolecules* **1983**, *16*, 1434-1443.
19. Khandpur, A. K.; Forster S.; Bates, F. S.; Hamley, I. W.; Ryan, A. J.; Bras, W.; Almdal, K.; Mortensen, K. Polyisoprene-Polystyrene Diblock Copolymer Phase Diagram near the Order-Disorder Transition. *Macromolecules* **1995**, *28*, 8796-8806
20. Lai, C.; Russel, W. B.; Register, R. A.; Marchand, G. R.; Adamson, D. H. Phase Behavior of Styrene-Isoprene Diblock Derivatives with Varying Conformational Asymmetry. *Macromolecules* **2000**, *33*, 3461-3466.
21. Lo, T-Y.; Chao, C-C.; Ho, R-M.; Georgopoulos, P.; Avgeropoulos, A.; Thomas, E. L. Phase Transitions of Polystyrene-b-poly(dimethylsiloxane) in Solvents of Varying Selectivity. *Macromolecules* **2013**, *46*, 7513-7524
22. Kim, M. I.; Wakada, T.; Akasaka, S.; Nishitsuji, S.; Saijo, K.; Hasegawa, H.; Ito, K.; Takenaka, M. Stability of the Fddd Phase in Diblock Copolymer Melts. *Macromolecules* **2008**, *41*, 7667-7670.
23. Rosedale, J. H.; Bates, F. S.; Almdal, K.; Mortensen, K.; Wignall, G. D. Order and Disorder in Symmetric Diblock Copolymer Melts. *Macromolecules* **1995**, *28*, 1429-1443.
24. Lee, S.; Gillard, T. M.; Bates, F. S. Fluctuations, Order, and Disorder in Short Diblock Copolymers. *AIChE Journal* **2013**, *59*, 3502-3513.
25. Matsushita, Y. Studies on Equilibrium Structures of Complex Polymers in Condensed Systems. *J. Polym. Sci., Part B: Polym. Phys.* **2000**, *38*, 1645-1655.

## Chapter 1

26. Lodge, T. P. Block Copolymers: Past Successes and Future Challenges. *Macromol. Chem. Phys.* **2003**, 204, 265-273.
27. Bates, F. S.; Fredrickson, G. H. Block Copolymers-Designer Soft Materials. *Physics Today* **1999**, 52, 32-38.
28. Bates, F. S. Polymer-Polymer Phase Behavior. *Science* **1991**, 251, 898-905.
29. Bates, C. M.; Bates, F. S. 50<sup>th</sup> Anniversary Perspective: Block Polymers-Pure Potential. *Macromolecules* **2016**.
30. Helfand, E.; Wasserman, Z. R. Block Copolymer Theory. 4. Narrow Interphase Approximation. *Macromolecules* **1976**, 9, 879-888.
31. Ohta, T.; Kawasaki, K. Equilibrium morphology of block copolymer melts. *Macromolecules* **1986**, 19, 2621-2632.
32. Matsen, M. W.; Schick, M. Stable and unstable phases of a diblock copolymer melt. *Phys Rev Lett* **1994**, 72, 2660-2663.
33. Matsen, M. W.; Whitemore, M. D. Accurate diblock copolymer phase boundaries at strong segregations. *J. Chem. Phys.* **1996**, 105, 9698-9701.
34. Matsen, M. W. Effect of Architecture on the Phase Behavior of AB-Type Block Copolymer Melts. *Macromolecules* **2012**, 45, 2161-2165.
35. Bates, F. S.; Rosedale, J. H.; Fredrickson, G. H. Fluctuation effects in a symmetric diblock copolymer near the order-disorder transition. *J. Chem. Phys.* **1990**, 92, 6255-6270.
36. Matsen, M. W.; Shick, M. Stable and Unstable Phases of a Diblock Copolymer Melt. *Phys. Rev. Lett.* **1994**, 72, 2660-2663.
37. Semenov, A. N. Theory of Block-Copolymer Interfaces in the Strong Segregation Limit.. *Macromolecules* **1993**, 26, 6617-6621.
38. Hadjichristidis, N.; Pispas, S.; Floudas, G. Block Copolymers: Synthetic Strategies, Physical Properties, and Applications.; Wiley Interscience: New York, 2003.
39. Hawker, C. J.; Russel, T. P. Block Copolymer Lithography Merging Bottom-Up with Top-Down Processes. *MRS Bulletin* **2006**, 30, 952-966.
40. Olson, D.A.; Chen, L.; Hillmyer, M. A. Templating Nanoporous Polymers with Ordered Block Copolymers. *Chem. Mater.* 2008. 20. 869-890.
41. Abe, A.; Albertsson, A.-C.; Coates, G.W.; Genzer, J.; Kobayashi, S.; Lee, K.-S.; Leibler, L.; Long, T.E.; Möller, M.; Okay, O.; Percec, V.; Tang, B.Z.; Terentjev, E.M.; Theato, P.; Vicent, M.J.; Voit, B.; Wiesner, U.; Zhang, X. *Advances in Polymer Science.*; Springer: Berlin.
42. Mogi, Y.; Nomura, M.; Kotsuji, H.; Ohnishi, K.; Matsushita, Y.; Noda, I. Superlattice Structures in Morphologies of the ABC Triblock Copolymers. *Macromolecules* **1994**, 27, 6755-6760.
43. Matsushita, Y.; Tamura, M.; Noda, I. Tricontinuous Double-Diamond Structure Formed by a Styrene-Isoprene-2-Vinylpyridine Triblock Copolymer. *Macromolecules* **1994**, 27, 3680-3682.
44. Breiner, U.; Krappe, U.; Thomas, E. L.; Stadler, R. Structural Characterization of the "Knitting Pattern" in Polystyrene-block-poly(ethylene-co-butylene)-block-poly(methyl methacrylate) Triblock Copolymers. *Macromolecules* **1998**, 31, 135-141.

## Chapter 1

45. Jackson, E. A.; Lee, Y.; Hillmyer, M. A. ABAC Tetrablock Terpolymers for Tough Nanoporous Filtration Membranes. *Macromolecules* **2013**, 46, 1484-1491.
46. Lee, S.; Bluemle, M. J.; Bates, F. S. Discovery of a Frank-Kasper  $\sigma$  Phase in Sphere-Forming Block Copolymer Melts. *Science* **2010**, 330, 349-353.
47. Zhang, J.; Bates, F. S. Dodecagonal Quasicrystalline Morphology in a Poly(styrene-*b*-isoprene-*b*-styrene-*b*-ethylene oxide) Tetrablock Terpolymer. *J. Am. Chem. Soc.* **2012**, 134, 7636-7639.
48. Takano, A.; Soga, K.; Asari, T.; Suzuki, J.; Arai, S.; Saka, H.; Matsushita, Y. Observation of Four-Phase Lamellar Structure from a Tetrablock Quarterpolymer of the ABC Type. *Macromolecules* **2003**, 36, 8216-8218.
49. Bates, F. S.; Hillmyer, M. A.; Lodge, T. P.; Bates, C. M.; Delaney, K. T.; Fredrickson, G. H. Multiblock Polymers: Panacea or Pandora's Box? *Science* **2012**, 336, 434-440.
50. Masuda, J.; Takano, A.; Nagata, Y.; Noro, A.; Matsushita, Y. Nanophase-Separated Synchronizing Structure with Parallel Double Periodicity from an Undecablock Terpolymer. *Phys. Rev. Lett.* **2006**, 97, 098301.
51. Ntaras, C.; Polymeropoulos, G.; Zapsas, G.; Ntetsikas, K.; Lontos, G.; Karanastasis, A.; Moschovas, D.; Rangou, S.; Stewart-Sloan, C.; Hadjichristidis, N.; Thomas, E. L.; Averopoulos, A. Synthesis, Characterization and Self-Assembly of Well-Defined Linear Heptablock Quaterpolymers. *J. Polym. Sci., Part B: Polym. Phys.* **2016**, 54, 1443-1449.
52. Matsushita, Y.; Iwata, H.; Asari, T.; Uchida, T.; ten Brinke, G.; Takano, A. Chain elongation suppression of cyclic block copolymers in lamellar microphase-separated bulk. *J. Chem. Phys.* **2004**, 121, 1129-1132.
53. Polymeropoulos, G.; Bilalis, P.; Hadjichristidis, N. Well-Defined Cyclic Triblock Terpolymers: A Missing Piece of the Morphology Puzzle. *ACS Macro Lett.* **2016**, 5, 1242-1246.
54. Matsushita, Y.; Momose, H.; Yoshida, Y.; Noda, I. Lamellar domain spacing of the ABB graft copolymers. *Polymer* **1997**, 38, 149-153.
55. Shi, W.; Tateishi, Y.; Li, W.; Hawker, C. J.; Fredrickson, G. H.; Kramer, E. J. Producing Small Domain Features Using Mikroarm Block Copolymers with Large Interaction parameters. *ACS Macro Letters* **2015**, 4, 1287-1292.
56. Matsushita, Y.; Hayashida, K.; Takano, A. Jewelry Box of Morphologies with Mesoscopic Length Scales - ABC Star-shaped Terpolymers. *Macromol. Rapid. Commun.* **2010**, 31, 1579-1587.
57. Yamauchi, K.; Takahashi, K.; Hasegawa, H.; Iatrou, H.; Hadjichristidis, N.; Kaneko, T.; Nishikawa, Y.; Jinnai, H.; Matsui, T.; Nishioka, H.; Shimizu, M.; Furukawa, H. Microdomain Morphology in an ABC 3-Miktoarm Star Terpolymer: A Study by Energy-Filtering TEM and 3D Electron Tomography. *Macromolecules* **2003**, 36, 6962-6966.
58. Zheng, W.; Wang, Z-G. Morphology of ABC Triblock Copolymers. *Macromolecules* **1995**, 28, 7215-7223.
59. Sun, M.; Wang, P.; Qiu, F.; Tang, P.; Zhang, H.; Yang, Y. Morphology and phase diagram of ABC linear triblock copolymers Parallel real-space self-consistent-field-theory simulation. *Physical Review E* **2008**, 77, 016701.
60. Liu, M.; Li, W.; Qiu, F.; Shi, A-C. Theoretical Study of Phase Behavior of Frustrated ABC Triblock

## Chapter 1

- Copolymers. *Macromolecules* **2012**, 45, 9522-9530.
61. Suzuki, J.; Takano, A.; Matsushita, Y. Morphology of symmetric ABCD tetrablock quaterpolymers by Monte Carlo simulation. *J. Chem. Phys.* **2016**, 145, 194905.
  62. Jaffer, K.M.; Wickham, R. A.; Shi, A-C. Noncentrosymmetric Lamellar Phase in ABCD Tetrablock Copolymers. *Macromolecules* **2004**, 37, 7042-7050.
  63. Xie, N.; Liu, M.; Deng, H.; Li, W.; Qiu, F.; Shi, A-C. Macromolecular Metallurgy of Binary Mesocrystals via Designed Multiblock Terpolymers. *J. Am. Chem. Soc.* **2014**, 136, 2974-2977.
  64. Liu, H-H.; Huang, C-I.; Shi, A-C. Self-Assembly of Linear ABCBA Pentablock Terpolymers. *Macromolecules* **2015**, 48, 6214-6223.
  65. Marko, J. F. Microphase Separation of Block Copolymer Rings. *Macromolecules* **1993**, 26, 1442-1444.
  66. Matsen, M. W.; Gradner, J. M. Anomalous domain spacing difference between AB diblock homologous A2B2 starblock copolymers. *J. Chem. Phys.* **2000**, 113, 1673-1676.
  67. Mayes, A. M.; de la Cruz, M. O. Microphase separation in multiblock copolymer melts. *J. Chem. Phys.* **1989**, 91, 7228-7235.
  68. Xie, N.; Li, W.; Qiu, F.; Shi, A-S.  $\sigma$  Phase Formed in Conformationally Asymmetric AB-Type Block Copolymers. *ACS Macro Letters* **2014**, 3, 906-910.
  69. Gemma, T.; Hatano, A.; Dotera, T. Monte Carlo Simulations of the Morphology of ABC Star Polymers Using the Diagonal Bond Method. *Macromolecules* **2002**, 35, 3225-3237.
  70. Kirkensgaard, J. J. K.; Pedersena, M. C.; Hyde, S. T. Tiling Patterns from ABC Star Molecules: 3-Colored Foams? *Soft Matter* **2014**, 10, 7182-7184.
  71. Breiner, U.; Krappe, U.; Abetz, V.; Stadler, R. Cylindrical morphologies in asymmetric ABC triblock copolymers. *Macromol. Chem., Phys.* **1997**, 198, 1051-1083.
  72. Huckstadt, H.; Gopfert, A.; Abetz, V. Influence of the block sequence on the morphological behavior of ABC triblock copolymers. *Polymer* **2000**, 41, 9089-9094.
  73. Bailey, T. S.; Pham, H. D.; Bates, F. S.; Morphological Behavior Bridging the Symmetric AB and ABC States in the Poly(styrene-b-isoprene-b-ethylene oxide) Triblock Copolymer System. *Macromolecules* **2001**, 34, 6994-7008.
  74. Epps, T. H.; Bates, F. S. Effect of Molecular Weight on Network Formation in Linear ABC Triblock Copolymers. *Macromolecules* **2006**, 39, 2676-2682.
  75. Kudose, I.; Kotaka, T. Morphological and viscoelastic properties of poly(styrene-b-butadiene-b-4-vinylpyridine) three-block polymers of the ABC type. *Macromolecules* **1984**, 17, 2325-2332.
  76. Mogi, Y.; Kotsuji, H.; Kaneko, Y.; Mori, K.; Matsushita, Y.; Noda, I. Preparation and Morphology of Triblock Copolymers of the ABC Type. *Macromolecules* **1992**, 25, 5408-5411.
  77. Matsen, M. W. Gyroid versus double-diamond in ABC triblock copolymer melts. *J. Chem. Phys.* **1998**, 108, 785-796.
  78. Abetz, V.; Goldacker, T. Formation of superlattices via blending of block copolymers. *Macromol. Rapid Commun.* **2000**, 21, 16-34.

## Chapter 1

79. Bailey, T. S.; Hardy, C. M.; Epps, T. H.; Bates, F. S. A Noncubic Triply Periodic Network Morphology in Poly(isoprene-*b*-styrene-*b*-ethylene oxide) Triblock Copolymers. *Macromolecules* **2002**, *35*, 7007-7017.
80. Epps, T. H.; Bailey, T. S.; Waletzko, R.; Bates, F. S. Phase Behavior and Block Sequence Effects in Lithium Perchlorate-Doped Poly(isoprene-*b*-styrene-*b*-ethylene oxide) and Poly(styrene-*b*-isoprene-*b*-ethylene oxide) Triblock Copolymers. *Macromolecules* **2003**, *36*, 2873-2881.
81. Chatterjee, J.; Jain, S.; Bates, F. S. Comprehensive Phase Behavior of Poly(isoprene-*b*-styrene-*b*-ethylene oxide) Triblock Copolymers. *Macromolecules* **2007**, *40*, 2882-2896.
82. Tyler, C. A.; Qin, J.; Bates, F. S.; Morse, D. C. SCFT Study of Nonfrustrated ABC Triblock Copolymer Melts. *Macromolecules* **2007**, *40*, 4654-4668.
83. Phan, S.; Fredrickson, G. H.; Morphology of Symmetric ABC Triblock Copolymers in the Strong Segregation Limit. *Macromolecules* **1998**, *31*, 59-63.
84. Guo, Z.; Zhang, G.; Qiu, F.; Zhang, H.; Yang, Y.; Shi, A-C. Discovering Ordered Phases of Block Copolymers: New Results from a Generic Fourier-Space Approach. *Phys. Rev. Lett.* **2008**, *101*, 028301.
85. Stadler, R.; Auschra, C.; Beckmann, J.; Krappe, U.; Voigt-Martin, I.; Leibler, L. Morphology and Thermodynamics of Symmetric Poly(A-block-B-block-C) Triblock Copolymers. *Macromolecules* **1995**, *28*, 3080-3097.
86. Jinnai, H.; Kaneko, T.; Matsunaga, K.; Abetz, C.; Abetz, V. A double helical structure formed from an amorphous, achiral ABC triblock terpolymer. *Soft Matter* **2009**, *5*, 2042-2046.
87. Elbs, H.; Abetz, V.; Hadziioannou, G.; Drummer, C.; Krausch, G. Antiferromagnetic Ordering in a Helical Triblock Copolymer Mesostructure. *Macromolecules* **2001**, *34*, 7917-7919.
88. Ludwigs, S.; Boker, A.; Abetz, V.; Muller, A. H. E.; Krausch, G. Phase behavior of linear polystyrene-block-poly(2-vinylpyridine)-block-poly(tert-butyl methacrylate) triblock terpolymers. *Polymer* **2003**, *44*, 6815-6823.
89. Balsamo, V.; von Gyldenfeldt, F.; Stadler, R. "Superductile" Semicrystalline ABC Triblock Copolymers with the Polystyrene Block (A) as the Matrix. *Macromolecules* **1999**, *32*, 1226-1232.
90. Li, W.; Qiu, F.; Shi, A-C. Emergence and Stability of Helical Superstructures in ABC Triblock Copolymers. *Macromolecules* **2012**, *45*, 503-509.
91. Kato, M.; Kamigaito, M.; Sawamoto, M.; Higashimura, T. Polymerization of Methyl Methacrylate with the Carbon Tetrachloride/ Dichlorotris-(triphenylphosphine)ruthenium(II)/ Methylaluminum Bis(2,6-di-tert-butylphenoxide) Initiating System: Possibility of Living Radical Polymerization. *Macromolecules* **1995**, *28*, 1721-1723.
92. Wang, J.-S.; Matyjaszewski, K. Controlled/"Living" Radical Polymerization. Atom Transfer Radical Polymerization in the Presence of Transition-Metal Complexes. *J. Am. Chem. Soc.* **1995**, *117*, 5614.
93. Matyjaszewski, K. Macromolecular Engineering by Controlled/Living Ionic and Radical Polymerizations. *Macromol. Symp.* **2001**, *174*, 51-67.
94. Chiefari, J.; Chong, Y. K.; Ercole, F.; Krstina, J.; Jeffery, J.; Le, T. P. T.; Mayadunne, R. T. A.; Meijs, G. F.; Moad, C. L.; Moad, G.; Rizzardo, E.; Thang, S. H. Living Free-Radical Polymerization by Reversible Addition-Fragmentation Chain Transfer: The RAFT Process. *Macromolecules* **1998**, *31*, 5559.

## Chapter 1

95. Moad, G.; Mayadunne, R. T. A.; Rizzardo, E.; Skidmore, M.; Thang, S. H. Synthesis of Novel Architecture by Radical Polymerization with Reversible Addition Fragmentation Chain Transfer (RAFT Polymerization). *Macromol. Symp.* **2003**, 192, 1-12.
96. Moad, G.; Rizzardo, E.; Solomon, D. H. Selectivity of the Reaction of Free Radicals with Styrene. *Macromolecules* **1982**, 15, 909-914.
97. Hawker, C. J.; Bosman, A. W.; Harth, E. New Polymer Synthesis by Nitroxide Mediated Living Radical Polymerizations. *Chem. Rev.* **2001**, 101, 3661.
98. Rzyayev, J. Molecular Bottlebrushes New Opportunities in Nanomaterials Fabrication. *ACS Macro Lett.* **2012**, 1, 1146-1149.
99. Braunecker, W. A.; Matyjaszewski, K. Controlled/living radical polymerization: Features, developments, and perspectives. *Prog. Polym. Sci.* **2007**, 32, 93-146.
100. Keddie, D. J. A guide to the synthesis of block copolymers using reversible-addition fragmentation chain transfer (RAFT) polymerization. *Chem. Soc. Rev.* **2014**, 43, 496-505.
101. Birshtein, T. M.; Lyatskaya, Yu. V.; Zhulina, E. B. Theory of supermolecular structures of polydisperse block copolymers: 1. Planar layers of grafted chains. *Polymer* **1990**, 31, 2185-2196.
102. Zhulina, E. B.; Birshtein, T. M. Theory of supermolecular structures of polydisperse block copolymers: 2. Lamellar superstructure consisting of two-block copolymers. *Polymer* **1991**, 32, 1299-1308.
103. Zhulina, E. B.; Lyatskaya, Yu. V.; Birshtein, T. M. Theory of supermolecular structures of polydisperse block copolymers: 3. Cylindrical layers of bidisperse chains. *Polymer* **1992**, 33, 332-342.
104. Lyatskaya, Yu. V.; Zhulina, E. B.; Birshtein, T. M. Theory of supermolecular structures of polydisperse block copolymers: 4. Cylindrical domains in binary mixtures of diblock copolymers and cylinder – lamellae transition. *Polymer* **1992**, 33, 343-351.
105. Birshtein, T. M.; Lyatskaya, Yu. V.; Zhulina, E. B. Theory of supermolecular structures of polydisperse block copolymers: 5. New double cylindrical structure in binary mixture of cylinder – forming diblock copolymers. *Polymer* **1992**, 33, 2750-2756.
106. Hadziannou, G.; Skoulios, A. Molecular Weight Dependence of Lamellar Structure in Styrene/Isoprene Two- and Three-Block Copolymers. *Macromolecules* **1982**, 15, 258-262.
107. Hasegawa, H.; Hashimoto, T. State of Mixing of Deuterated and Non-Deuterated Block Polymer Chains. *Kobunshi Ronbunshu* **1984**, 41, 759-762.
108. Burger, C.; Ruland, W.; Semenov, A. N. Polydispersity Effects on the Microphase-Separation Transition in Block Copolymers. *Macromolecules* **1990**, 23, 3339-3346.
109. Jiang, Y.; Yan, X.; Liang, H.; Shi, A-C. Effect of Polydispersity on the Phase Diagrams of Linear ABC Triblock Copolymers in Two Dimensions. *J. Phys. Chem. B.* **2005**, 109, 21047-21055.
110. Matsen, M. W. Effect of large degrees of polydispersity on strongly segregated block copolymers. *Eur. Phys. J. E.* **2006**, 21, 199-207.
111. Cooke, D. M.; Shi, A-C. Effects of Polydispersity on Phase Behavior of Diblock Copolymers. *Macromolecules* **2006**, 39, 6661-6671.

## Chapter 1

112. Matsen, M. W. Polydispersity-Induced Macrophase Separation in Diblock Copolymer Melts. *Phys. Rev. Lett.* **2007**, 99, 148304.
113. Lynd, N. A.; Hillmyer, M. A.; Matsen, M. W. Theory of Polydisperse Block Copolymer Melts Beyond the Schulz–Zimm Distribution. *Macromolecules* **2008**, 41, 4531-4533.
114. Lynd, N. A.; Meuler, A. J.; Hillmyer, M. A. Polydispersity and block copolymer self-assembly. *Prog. Poly. Sci.* **2008**, 33, 875-893.
115. Matsen, M. W. Comparison of A-block polydispersity effects on BAB triblock and AB diblock copolymer melts. *Eur. Phys. J. E.* **2006**, 21, 199-207.
116. Lynd, N. A.; Hillmyer, M. A. Influence of Polydispersity on the Self-Assembly of Diblock Copolymers. *Macromolecules* **2005**, 38, 8803-8810.
117. Lynd, N. A.; Hillmyer, M. A. Effects of Polydispersity on the Order–Disorder Transition in Block Copolymer Melts. *Macromolecules* **2007**, 40, 8050-8055.
118. Lynd, N. A.; Hamilton, B. D.; Hillmyer, M. A. The Role of Polydispersity in the Lamellar Mesophase of Model Diblock Copolymers. *J. Polym. Sci. B.* **2007**, 45, 3386-3393.
119. Meuler, A.; Ellison, C. J.; Evans, C. M.; Hillmyer, M. A.; Bates, F. S. Polydispersity-Driven Transition from the Orthorhombic *Fddd* Network to Lamellae in Poly(isoprene-*b*-styrene-*b*-ethylene oxide) Triblock Terpolymers. *Macromolecules* **2007**, 40, 7072-7074.
120. Meuler, A.; Ellison, C. J.; Hillmyer, M. A.; Bates, F. S. Polydispersity-Induced Stabilization of the Core–Shell Gyroid. *Macromolecules* **2008**, 41, 6272-6275.
121. Matsushita, Y.; Noro, A.; Iinuma, M.; Suzuki, J.; Ohtani, H.; Takano, A. Effect of Composition Distribution on Microphase-Separated Structure from Diblock Copolymers. *Macromolecules* **2003**, 36, 8074-8077.
122. Noro, A.; Iinuma, M.; Suzuki, J.; Takano, A.; Matsushita, Y. Effect of Composition Distribution on Microphase-Separated Structure from BAB Triblock Copolymers. *Macromolecules* **2004**, 37, 3804-3808.
123. Noro, A.; Cho, D.; Takano, A.; Matsushita, Y. Effect of Molecular Weight Distribution on Microphase-Separated Structures from Block Copolymers. *Macromolecules* **2005**, 38, 4371-4376.
124. Noro, A.; Okuda, M.; Odamaki, F.; Kawaguchi, D.; Torikai, N.; Takano, A.; Matsushita, Y. Chain Localization and Interfacial Thickness in Microphase-Separated Structures of Block Copolymers with Variable Composition Distributions. *Macromolecules* **2006**, 39, 7654-7661.
125. Torikai, N.; Noro, A.; Okuda, M.; Odamaki, F.; Kawaguchi, D.; Takano, A.; Matsushita, Y. Neutron Reflection Studies on Lamellar Microphase-Separated Structures of Two-Component Block Copolymers with Composition Distribution. *Physica B* **2006**, 385, 709-712.
126. Winey, K. I.; Thomas, E. L.; Fetters, L. J. Ordered morphologies in binary blends of diblock copolymer and homopolymer and characterization of their intermaterial dividing surfaces. *J. Chem. Phys.* **1991**, 95, 9367-9375.
127. Tanaka, H.; Hasegawa, H.; Hashimoto, T. Ordered Structure in Mixtures of a Block Copolymer and Homopolymers. 1. Solubilization of Low Molecular Weight Homopolymers. *Macromolecules* **1991**, 24, 240-251.

## Chapter 1

128. Hasegawa, H.; Tanaka, H.; Hashimoto, T. Ordered Structure in Mixtures of a Block Copolymer and Homopolymers. 2. Effects of Molecular Weights of Homopolymers. *Macromolecules* **1990**, *23*, 4378-4386.
129. Mayes, A. M.; Russel, T. P.; Satija, S. K.; Majkrzak, C. F. Homopolymer Distribution in Ordered Block Copolymers. *Macromolecules* **1992**, *25*, 6523-6531.
130. Dai, K. H.; Kramer, E. J.; Shull, K. R. Interfacial Segregation in Two-Phase Polymer Blends with Diblock Copolymer Additives: The Effect of Homopolymer Molecular Weight. *Macromolecules* **1992**, *25*, 220-225.
131. Koizumi, S.; Hasegawa, H.; Hashimoto, T. Spatial Distribution of Homopolymers in Block Copolymer Microdomains As Observed by a Combined SANS and SAXS Method. *Macromolecules* **1994**, *27*, 7893-7906.
132. Bodycomb, J.; Yamaguchi, D.; Hashimoto, T. A Small-Angle X-ray Scattering Study of the Phase Behavior of Diblock Copolymer Homopolymer Blends. *Macromolecules* **2000**, *33*, 5187-5197.
133. Disko, M. M.; Liang, K. S.; Behal, S. K.; Roe, R. J.; Jeon, K. J. Catenoid-Lamellar Phase in Blends of Styrene-Butadiene Diblock Copolymer and Homopolymer. *Macromolecules* **1993**, *26*, 2983-2986.
134. Takagi, H.; Yamamoto, K.; Okamoto, S. Ordered-bicontinuous-double-diamond structure in block copolymer / homopolymer blends. *EPL*. **2015**, *110*, 48003.
135. Matsen, M. W. Phase Behavior of Block Copolymer/Homopolymer Blends. *Macromolecules* **1995**, *28*, 5765-5773.
136. Semenov, A. N. Phase Equilibria in Block Copolymer-Homopolymer Mixtures. *Macromolecules* **1993**, *26*, 2273-281.
137. Matsen, M. W. Stabilizing New Morphologies by Blending Homopolymer with Block Copolymer. *Phys. Rev. Lett.* **1995**, *74*, 4225-4228.
138. Kielhorn, L.; Muthukumar, M. Spinodal decomposition of symmetric diblock copolymer/homopolymer blends at the Lifshitz point. *J. Chem. Phys.* **1999**, *110*, 4079-4089.
139. Padmanabhan, P.; Martinez-Veracoechea, F. J.; Escobedo, F. A. Computation of Free Energies of Cubic Bicontinuous Phases for Blends of Diblock Copolymer and Selective Homopolymer. *Macromolecules* **2016**, *49*, 5232-5243.
140. Martinez-Veracoechea, F. J.; Escobedo, F. A. The Plumber's Nightmare Phase in Diblock Copolymer Homopolymer Blends. A Self-Consistent Field Theory Study. *Macromolecules* **2009**, *42*, 9058-9062.
141. Izumi, Y.; Yamada, M.; Takano, A.; Matsushita, Y. A New Periodic Pattern with Five-Neighbored Domain Packing from ABC Triblock Terpolymer/ B Homopolymer Blend. *J. Polym. Sci. B.* **2015**, *53*, 907-911.
142. Tureau, M.; Rong, L.; Hsiao, B. S.; Epps, T. H. Phase Behavior of Neat Triblock Copolymers and Copolymer Homopolymer Blends Near Network Phase Windows. *Macromolecules* **2010**, *43*, 9039-9048.
143. Lescanec, R. L.; Fetters, L. J.; Thomas, E. L. Assessing Homopolymer Distribution in ABC Triblock Copolymer Homopolymer Blends through a Transition in Interfacial Geometry. *Macromolecules* **1998**, *31*, 1680-1685.
144. Matsushita, Y. Creation of Hierarchically Ordered Nanophase Structures in Block Polymers Having Various Competing Interactions. *Macromolecules* **2007**, *40*, 771-776.
145. Sugiyama, M.; Shefelbine, T. A.; Vigild, M. E.; Bates, F. S. Phase Behavior of an ABC Triblock Copolymer

## Chapter 1

- Blended with A and C Homopolymers. *J. Phys. Chem. B.* **2001**, 105, 12448-12460.
146. Dotera, T. Tricontinuous Cubic Structures in ABC/A/C Copolymer and Homopolymer Blends. *Phys. Rev. Lett.* **2002**, 89, 205502.
  147. Chen, F.; Kondo, Y.; Hashimoto, T. Control of Nanostructure in Mixtures of Block Copolymers Curvature Control via Cosurfactant Effects. *Macromolecules* **2007**, 40, 3714-3723.
  148. Wu, Z.; Li, B.; Jin, Q.; Ding, D.; Shi, A-C. Microphase and Macrophase Separations in Binary Blends of Diblock Copolymers. *Macromolecules* **2011**, 44, 1680-1694.
  149. Hashimoto, T.; Yamasaki, K.; Koizumi, S.; Hasegawa, H. Ordered structure in blends of block copolymers. 1. Miscibility criterion for lamellar block copolymers. *Macromolecules* **1993**, 26, 2895-2904.
  150. Hashimoto, T.; Koizumi, S.; Hasegawa, H. Ordered structure in blends of block copolymers. 2. Self-Assembly for Immiscible Lamella Forming Copolymers. *Macromolecules* **1994**, 27, 1562-1570.
  151. Koizumi, S.; Hasegawa, H.; Hashimoto, T. Ordered structure in blends of block copolymers. 3. Self-Assembly in Blends of Sphere- or Cylinder Forming Copolymers. *Macromolecules* **1994**, 27, 4371-4381.
  152. Yamaguchi, D.; Bodycomb, J.; Koizumi, S.; Hashimoto, T. Ordered structure in blends of block copolymers. 4. Location of the Short Diblock. *Macromolecules* **1999**, 32, 5884-5894.
  153. Yamaguchi, D.; Shiratake, S.; Koizumi, S.; Hashimoto, T. Ordered structure in blends of block copolymers. 5. Blends of Lamella-Forming Block Copolymers Showing both Microphase Separation Involving Unique Morphological Transitions and Macrophase Separation. *Macromolecules* **2000**, 33, 825-8268.
  154. Yamaguchi, D.; Hashimoto, T.; Han, C. D.; Baek, D. M.; Kim, J. K.; Shi, A-C. Order-Disorder Transition, Microdomain Structure, and Phase Behavior in Binary Mixtures of Low Molecular Weight Polystyrene-block-polyisoprene Copolymers. *Macromolecules* **1997**, 30, 5832-5842.
  155. Yamaguchi, D.; Hashimoto, T. A Phase Diagram for the Binary Blends of Nearly Symmetric Diblock Copolymers. 1. Parameter Space of Molecular Weight Ratio and Blend Composition. *Macromolecules* **2001**, 34, 6495-6505.
  156. Yamaguchi, D.; Hasegawa, H.; Hashimoto, T. A Phase Diagram for the Binary Blends of Nearly Symmetric Diblock Copolymers. 2. Parameter Space of Temperature and Blend Composition. *Macromolecules* **2001**, 34, 6506-6518.
  157. Court, F.; Hashimoto, T. Morphological Studies of Binary Mixtures of Block Copolymers. 1. Cosurfactant Effects and Composition Dependence of Morphology. *Macromolecules* **2001**, 34, 2536-2545.
  158. Court, F.; Hashimoto, T. Morphological Studies of Binary Mixtures of Block Copolymers. 2. Chain Organization of Long and Short Blocks in Lamellar Microdomains and Its Effect on Domain Size and Stability. *Macromolecules* **2002**, 35, 2566-2575.
  159. Yamaguchi, D.; Takenaka, M.; Hasegawa, H.; Hashimoto, T. Macro- and Microphase Transitions in Binary Blends of Block Copolymers with Complementarily Asymmetric Compositions. *Macromolecules* **2001**, 34, 1707-1719
  160. Vaidya, N. Y.; Han, C. D.; Kim, D.; Sakamoto, N.; Hashimoto, T. Microdomain Structures and Phase Transitions in Binary Blends Consisting of a Highly Asymmetric Block Copolymer and a Homopolymer.

## Chapter 1

- Macromolecules* **2001**, 34, 222-234.
161. Court, F.; Yamaguchi, D.; Hashimoto, T. Morphological and Scattering Studies of Binary Mixtures of Block Copolymers Cosurfactant Effects Observed in the Parameter Space of Temperature, Blend Composition, and Molecular Weight Ratio. *Macromolecules* **2008**, 41, 4828-4837.
162. Morita, H.; Kawakatsu, T.; Doi, M.; Yamaguchi, D.; Takenaka, M.; Hashimoto, T. Competition between Micro- and Macrophase Separations in a Binary Mixture of Block Copolymers. A Dynamic Density Functional Study. *Macromolecules* **2002**, 35, 7473-7480.
163. Court, F.; Yamaguchi, D.; Hashimoto, T. Morphological Studies of Binary Mixtures of Block Copolymers Temperature Dependence of Cosurfactant Effects. *Macromolecules* **2006**, 39, 2596-2605.
164. Lipic, P. M.; Bates, F. S.; Matsen, M. W. Non-equilibrium phase behavior of diblock copolymer melts and binary blends in the intermediate segregation regime. *J. Polym. Sci. B.* **1999**, 37, 2229-2238.
165. Sakurai, S.; Umeda, H.; Furukawa, C.; Irie, H.; Nomura, S.; Lee, H. H.; Kim, J. K. Thermally induced morphological transition from lamella to gyroid in a binary blend of diblock copolymers. *J. Chem. Phys.* **1998**, 108, 4333-4339.
166. Shi, A-C.; Noolandi, J. Effects of Short Diblocks at Interfaces of Strongly Segregated Long Diblocks. *Macromolecules* **1994**, 27, 2936-2944.
167. Matsen, M. W.; Bates, F. S. One-Component Approximation for Binary Diblock Copolymer Blends. *Macromolecules* **1995**, 28, 7298-7300.
168. Matsen, M. W. Immiscibility of large and small symmetric diblock copolymers. *J. Chem. Phys.* **1995**, 103, 3268-3271
169. Shi, A-C.; Noolandi, J. Binary Mixtures of Diblock Copolymers. Phase Diagrams with a New Twist. *Macromolecules* **1995**, 28, 3103-3109.
170. Wu, Z.; Li, B.; Ding, D.; Shi, A-C. Phase Behavior of Binary Blends of Diblock Copolymers. *J. Phys. Chem. B.* **2010**, 114, 15789-15798.
171. Liu, M.; Qiang, Y.; Li, W.; Qiu, F.; Shi, A-C. Stabilizing the Frank-Kasper Phases via Binary Blends of AB Diblock Copolymers. *ACS Macro Lett.* **2016**, 5, 1167-1171.
172. Abetz, V.; Simon, P. F. W. Phase Behaviour and Morphologies of Block Copolymers. *Adv Polym Sci.* **2005**, 189, 125-212.
173. Birshstein, T. M.; Polotsky, A. A.; Amoskov, V. M. Theory of Supercrystalline Structures in Mixtures of ABC Triblock and ab, bc, and ac, Diblock Copolymers. *Macromol. Symp.* **1999**, 146, 215-222.
174. Birshstein, T. M.; Zhulina, E. B.; Polotsky, A. A.; Abetz, V.; Stadler, R. Mixed supercrystalline structures in mixtures of ABC-triblock and AB(BC)-diblock copolymers 1. *Macromol. Theory Simul.* **1999**, 8, 151-160.
175. Birshstein, T. M.; Polotsky, A. A. Mixed supercrystalline structures in mixtures of ABC triblock and ab(bc) diblock copolymers 2. *Macromol. Theory Simul.* **2000**, 9, 115-129.
176. Birshstein, T. M.; Polotsky, A. A.; Abetz, V. Mixed Supercrystalline Structures in Mixtures of ABC Triblock and ab(bc) Diblock Copolymers, 3. *Macromol. Theory Simul.* **2001**, 10, 700-718.
177. Goldacker, T.; Abetz, V.; Stadler, R.; Erukhimovich, I.; Leibler, L. Non-centrosymmetric superlattices in block

## Chapter 1

- copolymer blends. *Nature* **1999**, 398, 137-139.
178. Wickham, R. A.; Shi, A-C. Noncentrosymmetric Lamellar Phase in Blends of ABC Triblock and ac Diblock Copolymers. *Macromolecules* **2001**, 34, 6487-6494.
  179. Goldacker, T.; Abetz, V. Core-Shell Cylinders and Core-Shell Gyroid Morphologies via Blending of Lamellar ABC Triblock and BC Diblock Copolymers. *Macromolecules* **1999**, 32, 5165-5167.
  180. Matsushita, Y.; Suzuki, J.; Izumi, Y.; Matsuoka, K.; Takahashi, S.; Aoyama, Y.; Mihira, T.; Takano, A. Formation of undulated lamellar structure from ABC block terpolymer blends with different chain lengths. *J. Chem. Phys.* **2010**, 133, 194901.
  181. Asai, Y.; Yamada, K.; Yamada, M.; Takano, A.; Matsushita, Y. Formation of Tetragonally-Packed Rectangular Cylinders from ABC Block Terpolymers Blends. *ACS Macro Letters* **2014**, 3, 166-169.
  182. Asai, Y.; Takano, A.; Matsushita, Y. Creation of Cylindrical Morphologies with Extremely Large Oblong Unit Lattices from ABC Block Terpolymers. *Macromolecules* **2015**, 48, 1538-1542.
  183. Asai, Y.; Takano, A.; Matsushita, Y. Asymmetric Double Tetragonal Domain Packing from ABC Triblock Terpolymer Blends with Chain Length Difference. *Macromolecules* **2016**, 49, 6940-6946.
  184. Abetz, V.; Jiang, S. Formation of superlattices in blends of 3-miktoarm star terpolymers with diblock copolymers. *e-Polymers* **2004**, 54, 1-9.
  185. Liu, Me.; Xia, B.; Li, W.; Qiu, F.; Shi, A-C. Self-Assembly of Binary Mesocrystals from Blends of BABCB Multiblock Copolymers and ABC Triblock Copolymers. *Macromolecules* **2015**, 48, 3386-3394.

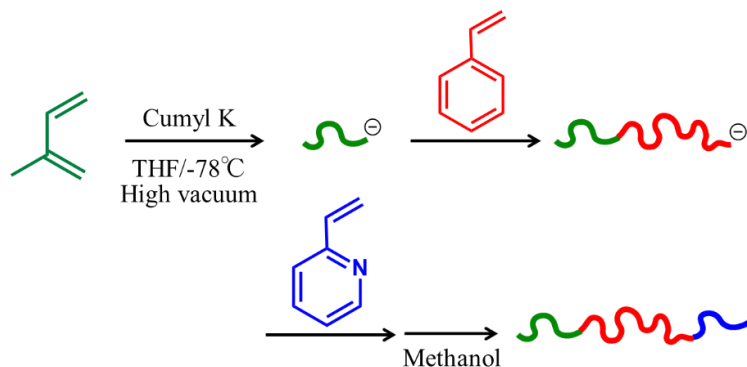
## CHAPTER 2

### Synthesis and Characterization

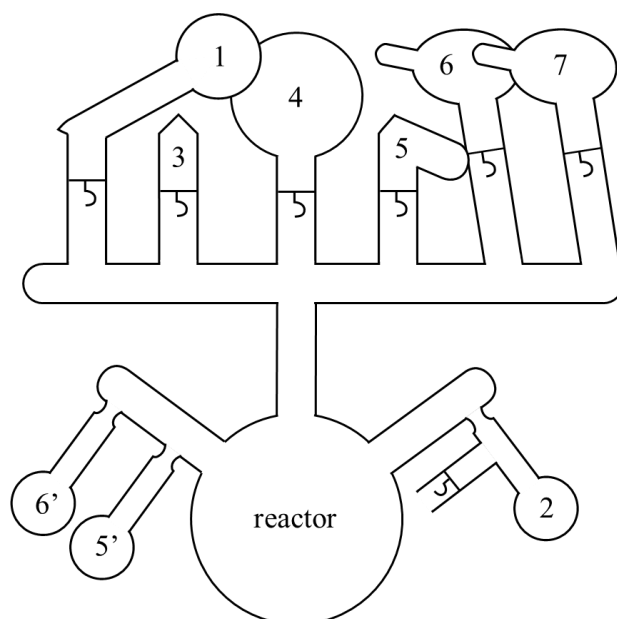
#### 2.1 Synthesis of poly(isoprene-*b*-styrene-*b*-2-vinylpyridine) (ISP) triblock terpolymers.

In this thesis, main concern is investigating the effect of different chain length on the morphology of ABC triblock terpolymers. Naturally, ABC triblock terpolymers have many parameters which influence phase formation; three interaction parameters ( $\chi_{AB}$ ,  $\chi_{BC}$ ,  $\chi_{AC}$ ), volume fractions ( $\phi_A$ ,  $\phi_B$ ,  $\phi_C$ ) and block sequences (ABC, ACB, BAC). In addition, for binary blends of ABC triblock terpolymers with different chain length, exact values of chain length difference are the most important parameters. In order to investigate the effect accurately and quantitatively, monodisperse triblock terpolymers must be needed and hence living anionic polymerization is the most suitable and qualified synthetic method. Living anionic polymerization was developed by Szwarc in 1956,<sup>1-3</sup> and since then this novel method has been widely used all over the world. As for anionic polymerization, the reactive site has remarkable stability, and the propagation reaction occurs by the controlled sequential addition of monomers. Owing to the stability, termination of growing chains and side reactions are negligible practically. However, the living anionic ends can be easily deactivated by air and impure substances. To achieve the polymerizations under highly-controlled condition, particularly high-grade purification of monomers and solvent is essential and it is desirable that polymerization is conducted under high vacuum. Thus, all operations for anionic polymerizations (polymerization, termination, initiator synthesis, purification of monomer and solvents and so on) adopted in this thesis were executed in sealed glass apparatuses under high

vacuum.

**Scheme 2.1.** Synthetic process of an ISP triblock terpolymer.

ISP triblock terpolymers were prepared in tetrahydrofuran (THF) at  $-78^{\circ}\text{C}$  via three-step anionic polymerization using cumyl potassium as an initiator, as presented in Scheme 2.1.<sup>4,5</sup> All operations were carried out in sealed glass apparatuses with breakseals under high vacuum ( $\sim 1 \times 10^{-3}$  Pa). The apparatus for preparation is illustrated in Figure 2.1. The “hook” and “constriction” illustrations express a breakseal and a part which can be burned out, respectively. The detailed synthetic process is mentioned below.

**Figure 2.1.** A glass apparatus for preparing an ISP triblock terpolymer.

## Chapter 2

At the beginning of the synthesis, it is necessary to clean the inner wall of the glass apparatus. The inner wall was rinsed with  $\alpha$ -methyl styrene tetramer potassium in THF (1) to deactivate impurities which can react with an initiator and a living anionic chain end. After cleaning thoroughly, the  $\alpha$ -methyl styrene tetramer potassium solution was collected into the vessel (2) and the nearest constricted part was burned out and remove the (2) part for reuse. Secondary, the initiator, cumyl potassium in THF (3) was poured into the reactor and subsequently THF (4) was added to the reactor. The solution was stirred until the temperature reached  $-78^{\circ}\text{C}$ . Before adding the isoprene monomer (4) to the reactor, the monomer was slightly cooled using liquid nitrogen. The propagation rate of isoprene is relatively low so that the polymerization solution was stirred for several hours to consume the monomer completely. Subsequently, addition of styrene monomer (6) resulted in the preparation of PI-*b*-PS<sup>-</sup>. Small amount of aliquots of PI<sup>-</sup> and PI-*b*-PS<sup>-</sup> were collected in (5') and (6') at each step to determine the exact molecular weights and volume fractions by SEC and <sup>1</sup>H-NMR. Finally, 2-vinylpyridine monomer was added to the reactor and stirred for a few hours. The resulting triblock terpolymers with living anionic ends were terminated with methanol. After the termination, the glass apparatus was opened to the atmosphere. The polymer solutions were strained through a filter paper with 6 $\mu\text{m}$  pores and subsequently filtered by a membrane filter with 200nm pores to remove small glass pieces of breakseals completely. The ISP triblock terpolymers were purified by reprecipitation in water/methanol/acetone/hexane mixed solvent. The compositions of the solvents used for reprecipitation depend on the volume fractions of the synthesized ISP triblock terpolymers. After filtrations, they were dried in vacuo, followed by Freeze-drying in benzene to remove residual solvents as necessary. This procedure was well-established by Fujimoto, Matsushita and Mogi<sup>5-9</sup>. See their articles for further details of the synthesis, especially the procedures for preparation of cumyl potassium<sup>6</sup> and purification of solvent and monomers<sup>7-9</sup>.

Eleven ISP triblock terpolymers were prepared for this thesis. Their molecular characteristics are listed in Table 2.1. The detail of their characterizations will be presented in the next section.

**Table 2.1.** Molecular Characteristics of Polymers Used in This Thesis.

Name	$M_n$ (kg/mol) <sup>a), b)</sup>	$M_n(I) : M_n(S) : M_n(P)$ (kg/mol) <sup>b), c)</sup>	$\phi_I : \phi_S : \phi_P$ <sup>b)</sup>	$M_w/M_n$ <sup>d)</sup>	Chapter
ISP-66	126	8.7 : 63.9 : 53.4	0.08 : 0.52 : 0.40	1.03	3
ISP-58	122	14 : 66 : 42	0.13 : 0.55 : 0.32	1.05	3
ISP-53	150	33 : 81 : 36	0.24 : 0.55 : 0.21	1.07	3
ISP-57	133	41 : 76 : 16	0.34 : 0.55 : 0.10	1.04	3
ISP-61	124	44.5 : 72.5 : 7	0.39 : 0.56 : 0.05	1.06	3, 4
ISP-70	122	6.3 : 74.6 : 41	0.06 : 0.62 : 0.32	1.02	3, 4
ISP-80	223	24 : 149 : 50	0.12 : 0.67 : 0.21	1.02	5
ISP-68	264	103 : 155 : 6	0.42 : 0.56 : 0.02	1.03	5
ISP-72	136	10 : 55.2 : 70.7	0.09 : 0.42 : 0.49	1.02	6
ISP-73	146	68.5 : 62.1 : 15.3	0.51 : 0.40 : 0.09	1.03	6
ISP-77	177	23 : 127 : 27	0.15 : 0.71 : 0.14	1.02	7

<sup>a)</sup>Determined by osmometry. <sup>b)</sup>Determined by <sup>1</sup>H-NMR spectroscopy and the densities of I, S and P at room temperature ( $\rho_I$ : 0.926,  $\rho_S$ : 1.05,  $\rho_P$ : 1.14 g/cm<sup>3</sup>). <sup>c)</sup> Estimated from MALLS. <sup>d)</sup> Estimated from a SEC chromatogram whose elution volumes were calibrated with polystyrene standards. "Chapter" expresses which chapter the ISP polymer is used in.

## 2.2 Characterization and analysis

ISP triblock terpolymers used were characterized by size exclusion chromatography (SEC), proton nuclear magnetic resonance ( $^1\text{H-NMR}$ ) spectroscopy, osmometry and differential scanning calorimetry (DSC). Microphase-separated structures were investigated with transmission electron microscopy (TEM), TEM tomography (TEMT), small angle X-ray scattering (SAXS) and microbeam SAXS ( $\mu\text{-SAXS}$ ). These techniques are briefly reviewed in this section.

### 2.2.1 Size Exclusion Chromatography (SEC)

Size exclusion chromatography (SEC) is used as a standard analytical method to measure the relative weight- ( $M_w$ ) and number-averaged molecular weights ( $M_n$ ) as well as the polydispersity index ( $M_w/M_n$ ).<sup>10</sup> This method separates molecules in dilute solutions by their sizes and in some cases by the interactions with microporous gel materials filled in columns (which is called as interaction chromatography (IC)<sup>11</sup>), by flowing the solution through columns. For polymeric system, molecular weight of a polymer directly relates to the size of the molecule. Larger molecules simply pass through gels because the molecules are too large to access pores, resulting in short elution time (volume). Smaller molecules are trapped in the larger pores than the hydrodynamic volumes of the polymer chains. Hence, a larger polymer flows out first and a small one comes out later.

Empirically, the elution time increases linearly with the logarithm of the molecular weight within the effective column working range, which is defined by the exclusion limit and the permeation limit. The correlation between elution times and molecular weights is determined by calibration using several polymer standard samples with known molecular weights.

SEC is a convenient tool for block copolymers as well. Although SEC cannot

determine directly the molecular weights of block copolymers, this method is quite useful to estimate the polydispersities and the purities of synthesized sample specimens, in addition the reaction progress of block copolymers can be monitored.

SEC measurements were carried out using an HPLC system composed of a pump, LC-20AD (Shimadzu Co.), a column oven, CTO-20A (Shimadzu Co.), a differential refractive index detector, RID-10A (Shimadzu Co.) and a UV detector, SPD-20A (Shimadzu Co.) equipped with three polystyrene gel columns, TSK-gel G4000H<sub>HR</sub> (Tosoh Co.). Tetrahydrofuran (THF) was used as an eluent with 0.1 % addition of tetramethylethylenediamine (TMEDA) with a flow rate of 1ml/min at 40°C. TMEDA was used to suppress adsorption of poly(2-vinylpyridine) on the polystyrene gels. SEC chromatograms of parent ISP triblock terpolymers used in this thesis are displayed below.

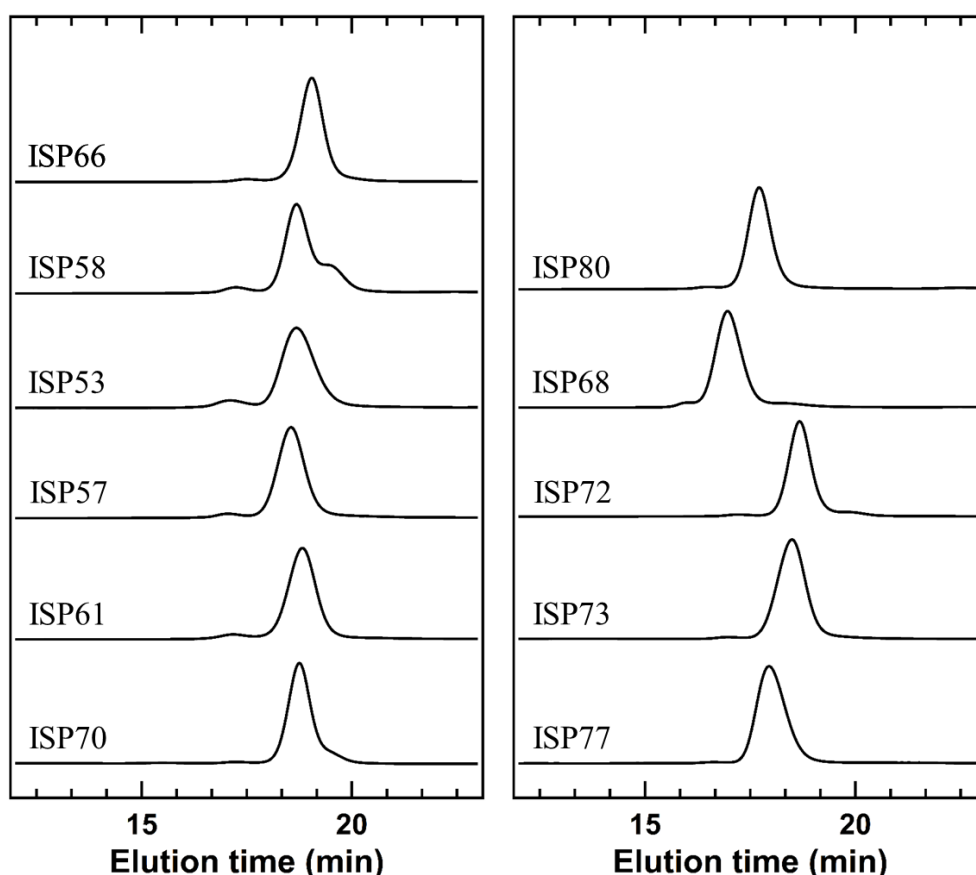


**Figure 2.2.** SEC chromatograms of parent ISP triblock terpolymers.

### 2.2.2 Proton Nuclear Magnetic Resonance (<sup>1</sup>H-NMR) spectroscopy

Nuclear magnetic resonance (NMR) spectroscopy is a common and standard analytical technique that exploits the magnetic properties of certain atomic nuclei.<sup>12</sup> For polymeric system, NMR determines number average molecular weights, weight fractions of block copolymers and the microstructures of the repeating units and etc.

The volume fractions of ISP triblock terpolymers and the microstructures of polyisoprene blocks were determined by <sup>1</sup>H-NMR at 500 MHz using Bruker Topspin 3.2 spectrometer. Polymer samples were dissolved in CDCl<sub>3</sub> with tetramethylsilane (TMS) used as an accepted internal standard.

Representative <sup>1</sup>H-NMR spectra and peak assignments for an ISP triblock terpolymer are shown in Figure 2.3. This NMR spectra confirmed polyisoprene block chain is preferentially conformed of 1,2- and 3,4-addition microstructures (> 90 %), reflecting that polyisoprenes polymerized in polar solvents show high vinyl contents.<sup>13, 14</sup> Indeed, all ISP triblock terpolymers, which were synthesized in THF, listed in Table 2,1 contain less than 8 % 1,4-addition microstructure.

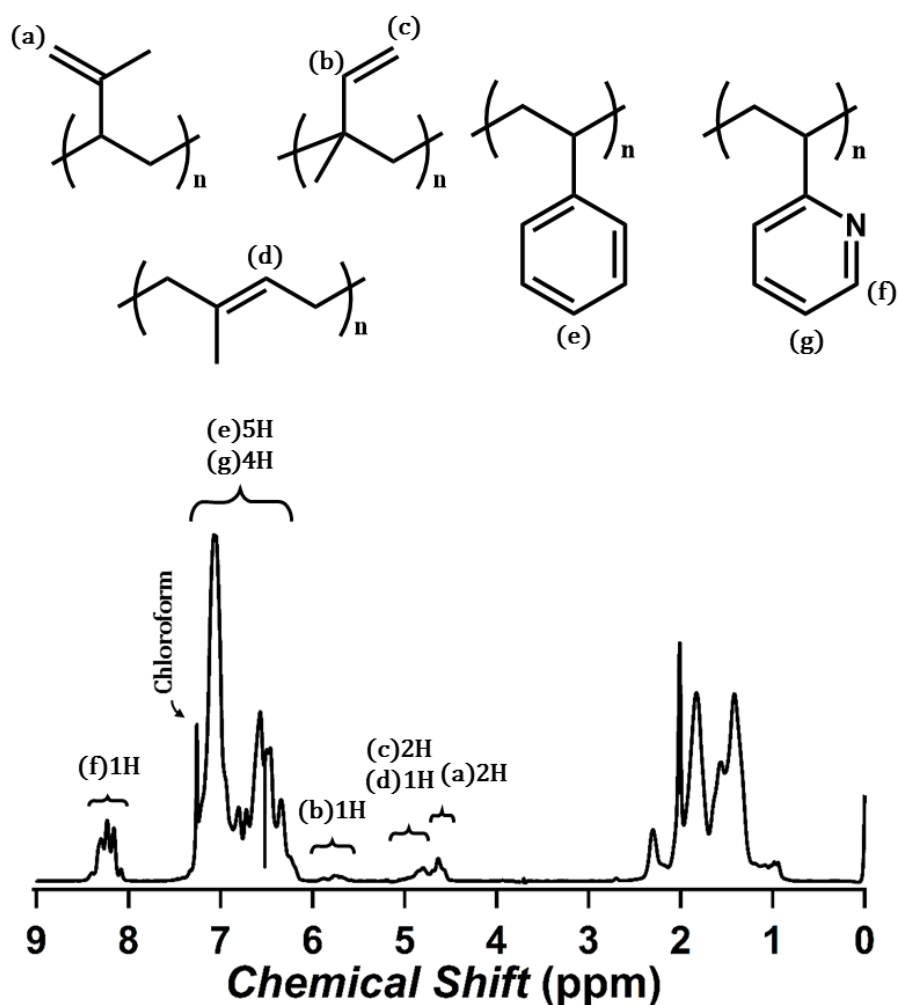


**Figure 2.3.**  $^1\text{H-NMR}$  spectrum of ISP-70. The chemical shifts for the associated protons are indicated using alphabets (a) through (g) and their integrated areas are expressed at the top of the peaks.

### 2.2.3 Osmometry

An osmometer is a device for measuring the osmotic pressure of solutions. For a polymer solution, "Membrane" osmometry is an optimum method to measure the number average molecular weight ( $M_n$ ) of a polymer therein.<sup>10</sup> While SEC measurements determine the relative  $M_n$ s by calibration using standard samples with known molecular weights, osmometry can determine the absolute  $M_n$ s by an extrapolation procedure to infinite dilution.

## Chapter 2

The osmotic pressure,  $\pi$ , is generated by the difference between the chemical potential of the solvent ( $\mu_s$ ) in solution and that of pure solvent ( $\mu_o$ ). To keep the system in equilibrium, the chemical potential of the solvent on the two sides of the membrane requires to be balanced and made equal, resulting in the solvent flow through the membrane into the solution. Osmotic pressure can be expressed with chemical potentials:

$$\mu_o - \mu_s = -\pi V_1 \quad (2-1)$$

where  $V_1$  is the partial molar volume of the solute. Osmotic pressure is also related to molecular weight  $M$  of a polymer as absolute by the van't Hoff equation:

$$\frac{\pi}{c} = RT \left( \frac{1}{M} + A_2 C + A_2 C^2 + \dots \right) \quad (2-2)$$

and if the equation (2-2) is extrapolated to zero concentration:

$$\left( \frac{\pi}{c} \right)_{c \rightarrow 0} = \frac{RT}{M} + A_2 C \quad (2-3)$$

Osmometry was operated on Gonotec OSMOMAT 090. The measurements were carried out in benzene at 37°C using a cellulose membrane (~20kDa). 4 dilute solutions with different concentrations for each sample were prepared. Representative plots of  $\pi/c$  vs  $c$  for ISP triblock terpolymers are shown in Figure 2.4. The intercepts extrapolated by using the data points provide the direct evaluation of  $M_n$  according to eq.(2-3). The difference in the slopes in Figure 2.4 ensures the difference in the second virial coefficients which evidently depend on the compositions of the samples.

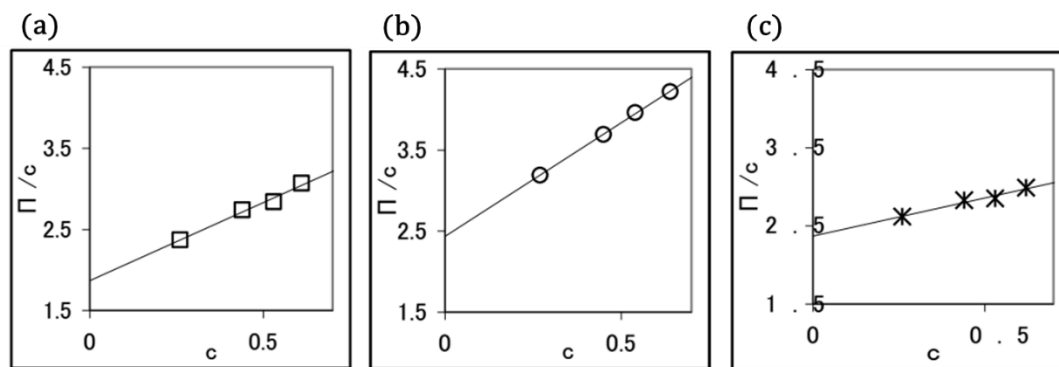


**Figure 2.4.**  $\pi/c$  vs  $c$  plots for ISP triblock terpolymers. (a) ISP-53, (b) ISP-57, (c) ISP-58, (d) ISP-61, (e) ISP-66.

### 2.2.4 Differential Scanning Calorimetry (DSC)

Differential scanning calorimetry (DSC) is a thermodynamical tool for direct assessment of the heat energy uptake. For polymeric system, DSC is generally used to measure crystalline melting temperature, glass transition temperature.

DSC traces were collected on a TA instruments DSC Q 2000 using a temperature ramp rate at 10 °C/min. The examples of DSC thermograms are shown in Figure 2.5 with polyisoprene, polystyrene and poly(2-vinylpyridine) homopolymers and their  $T_g$ s are denoted with inverted triangles. Their  $T_g$ s are in good accordance with literatures.<sup>13,15</sup> Polyisoprene chain prepared in this work is confirmed to show high  $T_g$  than 1,4-rich PI, indicating that it contains higher 1,2-and 3,4-addition fractions.

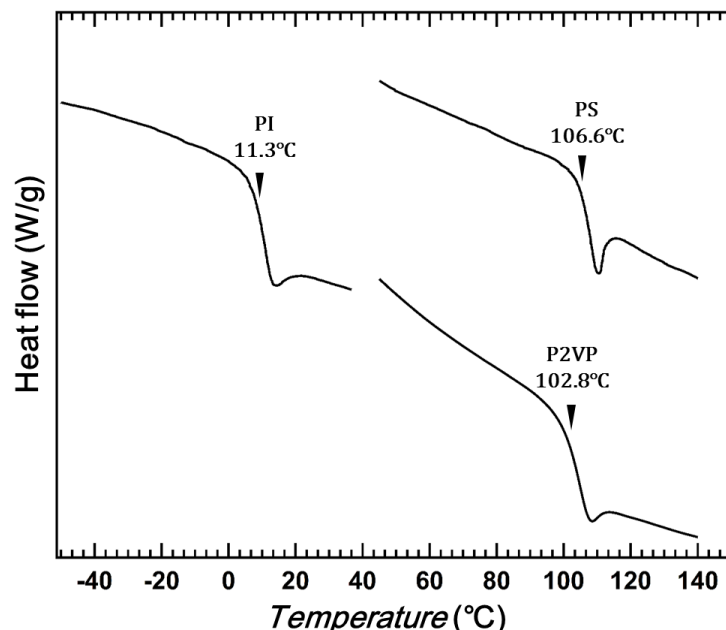


**Figure 2.5.** DSC traces of PI ( $M_n$ :45 kg/mol), PS ( $M_n$ :700 kg/mol), P2VP ( $M_n$ :120 kg/mol). The samples were heated over the expected  $T_g$  and cooled down, then heated to 200°C at a rate of 10 K/min. The traces show the second heating ramp. The  $T_g$ s were determined by the mid-points of the transitions.

### 2.2.5 Transmission Electron Microscopy (TEM)

Transmission electron microscopy (TEM) is a very powerful tool for material science in a nanometer scale. TEM is composed of many components: electron gun, electromagnetic coils, electromagnetic lenses, apertures, specimen holder, detector and vacuum pumps.<sup>16</sup> Figure 2.6 shows a simple sketch of TEM in comparison with that of optical microscopy (OM). A high energy electron beam, which is accelerated down the column, is transmitted through a specimen (ultrathin section) interacting with the specimen as it passes through it. When electrons are accelerated up to a high energy level and focused on a material, they can scatter or backscatter inelastically or elastically, or induce many interactions, source of different signals such as Auger electrons and X-rays. Some of them are used in TEM, where an image is created from the interaction of the electrons transmitted through the specimen. In principle,

## Chapter 2

TEM contrast arises because of the differences in electron density of the elements constituting the sample specimen. TEM enables us to image at a significantly higher resolution than OM because the wavelength of electrons is much shorter than that of light (OM). Thus TEM can provide structural information in the order of a few angstrom or less. Surprisingly, very small molecules such as water molecules, benzene molecules have already been directly observed by TEM. Furthermore, combining TEM with various detectors and apparatuses realizes quantitative analysis, such as electron energy-loss spectroscopy (EELS) and energy dispersive X-ray spectroscopy (EDS).

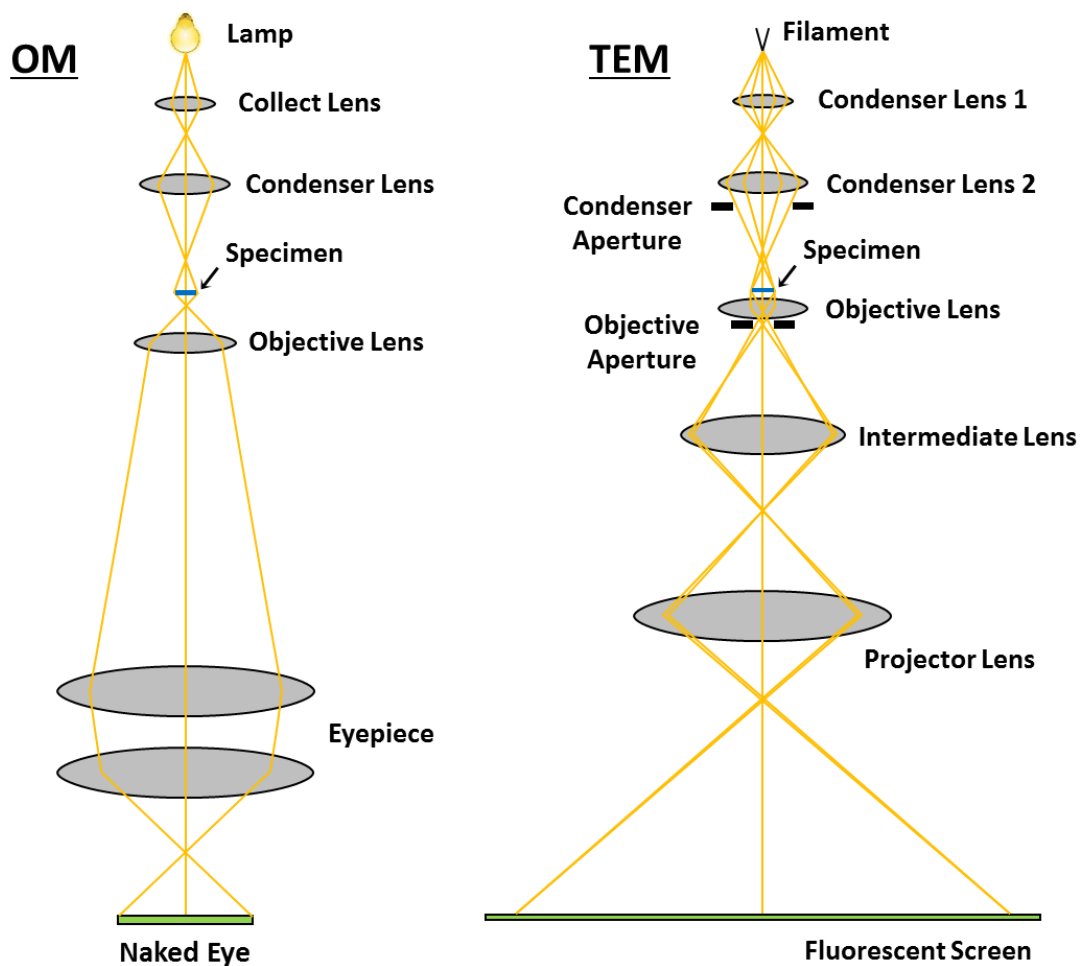


**Figure 2.6** A simple sketch of optical microscopy (OM) and transmission electron microscopy (TEM).

In this thesis, TEM observations were carried out by using JEM-1400 of JEOL Ltd. operated at an accelerating voltage of 120 kV in the bright field mode. Samples for TEM observations are required to be ultrathin: a few tens of nanometers, to obtain high-resolution images. The sample preparation process holds a lot of knowhow and/or experiences and it will be presented in the next sections.

### 2.2.5.1 Sample preparation for morphological observations

Sample films for TEM observations were prepared by solvent casting procedure using tetrahydrofuran (THF). THF is a nonselective solvent for I, S and P components. Unless otherwise noted, THF is used for the film preparation. The sample amount was accurately measured (within 1% error) and the sample was placed into a glass vessel, successively THF (without an antioxidant) was poured into the vessel to be 5 wt% solution. The solution was stirred for at least 6 hours at room temperature. The solution was transferred into a Teflon beaker and the beaker was placed in a glass vessel as shown in Figure 2.7. The glass vessel is sealed with a plastic cap that has a small hole ( $\varphi = 500 \mu\text{m}$  or  $700 \mu\text{m}$ ), where the hole size regulates the speed of solvent evaporation. The solvent was evaporated slowly over 2 weeks at  $25^\circ\text{C}$  in a temperature control oven. Subsequently, the film was dried thoroughly under vacuum for 1 day and then thermally treated at  $150^\circ\text{C}$  for 5 days in vacuo.

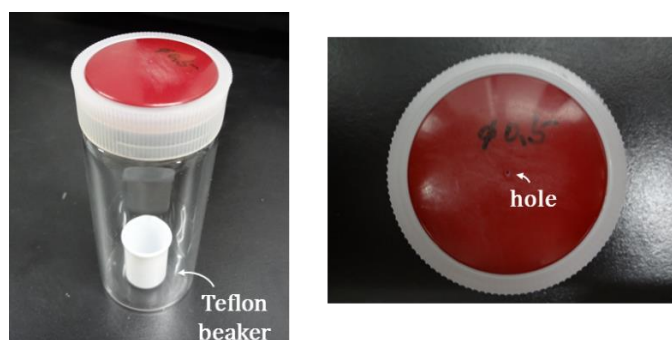


**Figure 2.7.** Images of apparatus for film preparation.

## Chapter 2

For TEM observations, several small pieces of the annealed bulk films were embedded in an epoxy resin. The epoxy resin was prepared in the following way. All materials for embedding were purchased from Nisshin EM Co. Ltd... First, Quetol-812, dodecenyl succinic anhydride (DSA) and methylnadic anhydride (MNA) were mixed at the ratio of 2.02 g: 0.51 g: 1.45 g (12-piece recipe), respectively. The mixture was stirred gently not to contain air bubbles for 30 min, followed by adding 0.08 g of 2,4,6-Tris (dimethylaminomethyl)phenol (DMP-30) as an accelerator. The mixture was stirred gently again for 20 min and became harder, successively the complex yellow liquid was poured into a Teflon mold in which the small pieces of the annealed film were preinstalled. The resin was cured at 90°C for 6 hours in an oven.

### **2.2.6.2 Microtoming**

A microtome is an important tool for morphological observations because it can cut films into thin sections of materials with thicknesses as intended. The preparation of thin slices of polymers is the preferred method to obtain good images for TEM. The typical thicknesses of the slices lie between 40 and 100 nm for TEM observations. Thicker sections (> 150 nm) are required for TEM tomography to earn structural information in the specimens. The careful mechanical construction, e.g. the same manner as a rotational microtome and tight tolerance on the mechanical construction, provides fine thickness control. Although microtoming is a generalized-method, there are a lot of skills to obtain uniform sections. While using a microtome, we should always pay attention to many factors; knife type, cutting speed, blade angle, amount of water, sample angle, dust and so on.

The embedded samples were ultramicrotomed to a thickness of ca. 50 nm using a Leica Ultracut UCT microtome with a Diatome diamond knife at room temperature. The ultrathin sections were floated on water and then transferred onto a Cu 300 mesh grid.

### 2.2.6.3 Staining

Since there exists small difference in contrasts among polymers, staining is an essential protocol to enhance contrasts for polymers in TEM observations. Ruthenium tetroxide ( $\text{RuO}_4$ ), osmium tetroxide ( $\text{OsO}_4$ ) and phosphotungstic acid (PTA) are commonly used as staining reagents.<sup>17-20</sup>  $\text{RuO}_4$  is an effective staining agent for both saturated and unsaturated polymers (polystyrene, polyolefin, polyester).  $\text{OsO}_4$  is useful for unsaturated polymers (polybutadiene, polyisoprene), while PTA stains well nitrogen-containing polymers. In addition to the above three basic staining reagents, there are several staining techniques that have been developed: negative staining, shadowing and replicas. In order to obtain good TEM images, proper selection of staining agents and technique is required.

The combination of  $\text{OsO}_4$  and iodine ( $\text{I}_2$ ) is identified as suitable for I-S-P three component system.<sup>21</sup>  $\text{OsO}_4$  stains heavily polyisoprene, whereas  $\text{I}_2$  selectively stains poly(2-vinyl pyridine). By twostep staining with both the agents, I, S and P phases appear dark, white and gray, respectively. Although  $\text{RuO}_4$  is a well-established agent to stain a benzene-ring, it gives too much contrasts for S against P to identify the phases.

$\text{OsO}_4$  solid (light yellow) was purchased from Nisshin EM Co. Ltd. and it was added to distilled water to prepare 5 wt% aqueous solution.  $\text{I}_2$  solid was purchased from Tokyo Chemical Institute (TCI) Co., Ltd..

For  $\text{OsO}_4$  vapor staining, thin films on a Cu grid were transferred onto a filter paper laid out at the center of a glass vessel as shown in Figure 2.8. 5 wt%  $\text{OsO}_4$  solution was poured into a ditch at the edge of the glass vessel. The vessel was covered with the lid and then heated up at 70°C for 2 hours. After cooling sufficiently, the Cu grid was collected.

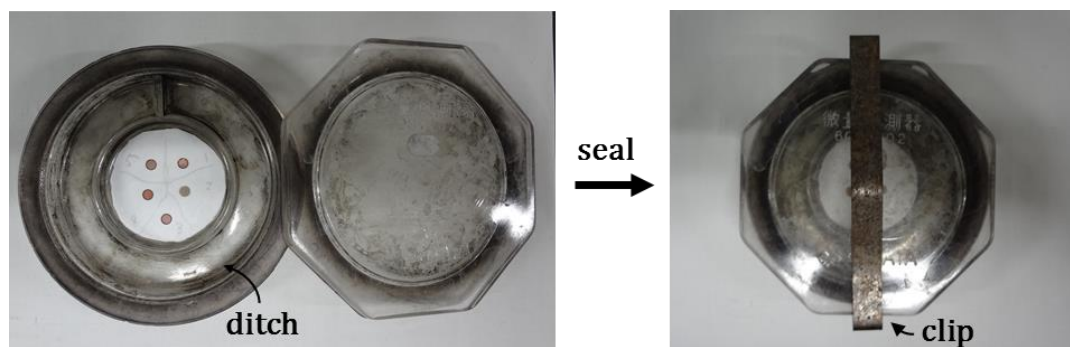


**Figure 2.8** Images of apparatus for  $\text{OsO}_4$  vapor staining.

As for  $\text{I}_2$  vapor staining, a slightly different methodology from that for  $\text{OsO}_4$  vapor staining was adopted. A Cu grid with thin sections was placed to stand on a plastic board as shown in Figure 2.9 and transferred into the center of a glass vessel.  $\text{I}_2$  solid powder was put into a ditch at the edge of the glass vessel. The vessel was covered with the lid and then heated up at  $50^\circ\text{C}$  for 2 hours. The vessel was opened without cooling and the Cu grids were collected. If it was cooled slowly, some small  $\text{I}_2$  particles attach on the sample films. Staining in the order of  $\text{OsO}_4$  and  $\text{I}_2$  is important, because some impurities appear on the thin sections if staining was carried out in the opposite order.

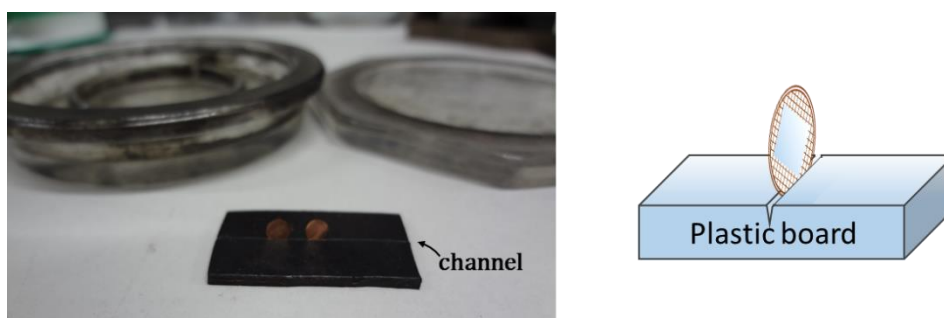


**Figure 2.9** Image and schematic illustration of apparatus for  $\text{I}_2$  vapor staining.

$\text{OsO}_4$  bulk staining significantly enhances contrasts. Before embedding, small pieces of the annealed films are placed into an ampule and a 5 wt%  $\text{OsO}_4$  aqueous solution was poured into it. The ampule was sealed and heated at  $70^\circ\text{C}$  for 2 hours in a water bath. All samples

treated with  $\text{OsO}_4/\text{I}_2$  vapor were pretreated with this  $\text{OsO}_4$  bulk staining. Many experiments confirmed that  $\text{OsO}_4$  bulk staining does not affect the morphology seriously.

Summary figure of sample preparation protocol for TEM observation is shown below.

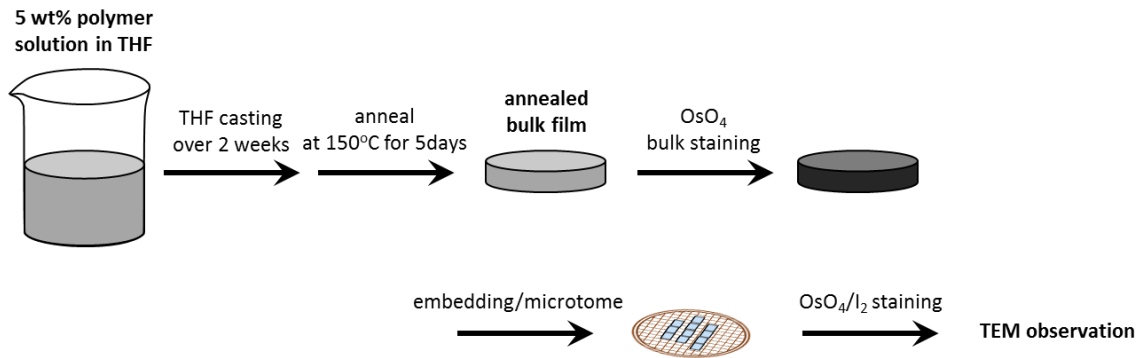


**Figure 2.10.** Sample preparation protocol for TEM observations

Figure 2.11 compares TEM images (of Blend(48/52) in Chapter 4) treated with different staining conditions. Each staining condition is described at the upper section of the corresponding TEM image. The sample stained with  $\text{OsO}_4/\text{I}_2$  vapor for a short time show a reasonably good image to identify the structure, however, the domain interfaces are somewhat obscured. A better image was obtained by the addition of the bulk staining process. Certainly, this image gives a sufficient result, long time  $\text{I}_2$  vapor staining enhances further TEM contrast as shown in Figure 2.12 (c).

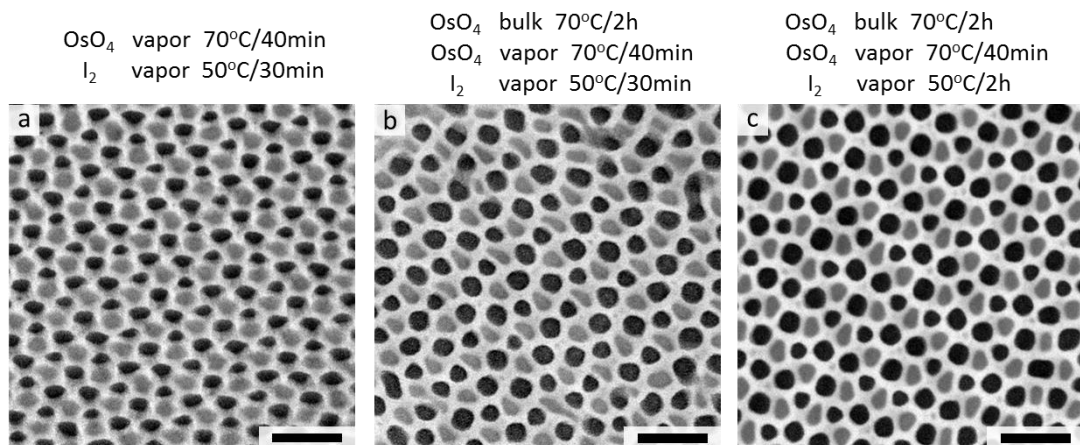


**Figure 2.11** Comparison of TEM images stained with OsO<sub>4</sub>/I<sub>2</sub> on various conditions. TEM images were taken for Blend(48/52) in chapter 4. All scale bars represent 100 nm.

### 2.2.6 Transmission Electron Microscopy Tomography (TEMT)

Recent improvement in the polymerization technique provides complex morphologies, and hence, the identification of these complex morphologies become more difficult, however, conventional microscopy provides only two-dimensional (2D) information. Three-dimensional (3D) information is of growing importance in morphology as polymer science advances.<sup>16,22,23</sup>

In electron tomography, images at different angles are taken by tilting the specimen with regard to the electron beam in the TEM apparatus. The micrographs obtained by careful rotation of specimen were reconstructed to generate 3D images. The small gap inside polepiece and the objective lens restricts the rotation angle in TEMT. This restriction induces “missing cone” where the projection information on the specimen cannot be obtained. To obtain high-accuracy 3D images, decreasing the effect of the missing cone is more important than increasing the number of tilt-series images.

One of the most effective approaches to solve this problem is to employ the second tilt axis, what is called “dual axis tomography”. However, it requires cumbersome experiments such as two tilting experiments for the same sample, and high-precision combination of two 3D data sets is also required. Despite the considerable efforts, it is still hard to fully eliminate the missing region. Another solution for the missing cone problem is the preparation of needle-shaped specimen by using the focused ion beam (FIB). The specimen can be rotated over the angular range of  $\pm 90^\circ$  and hence a complete tilt series can be obtained.

In this thesis, TEM tomography was performed in three chapters. In chapter 3,

single-axis rotated images were collected and reconstructed. In chapter 4, tilted images were taken in dual-axis. In chapter 6, needle-shaped specimens were prepared by FIB and TEM micrographs were collected covering angular range of  $\pm 82^\circ$ . Detail equipment conditions and sample preparations are mentioned in each chapter.

The aligned micrographs were constructed to give 3D image by filtered back projection method using a software, TEMography (System in Frontier, Inc., Japan). The conceptual diagrams of images capturing and 3D reconstruction are described in Figure 2.12 and 2.13.

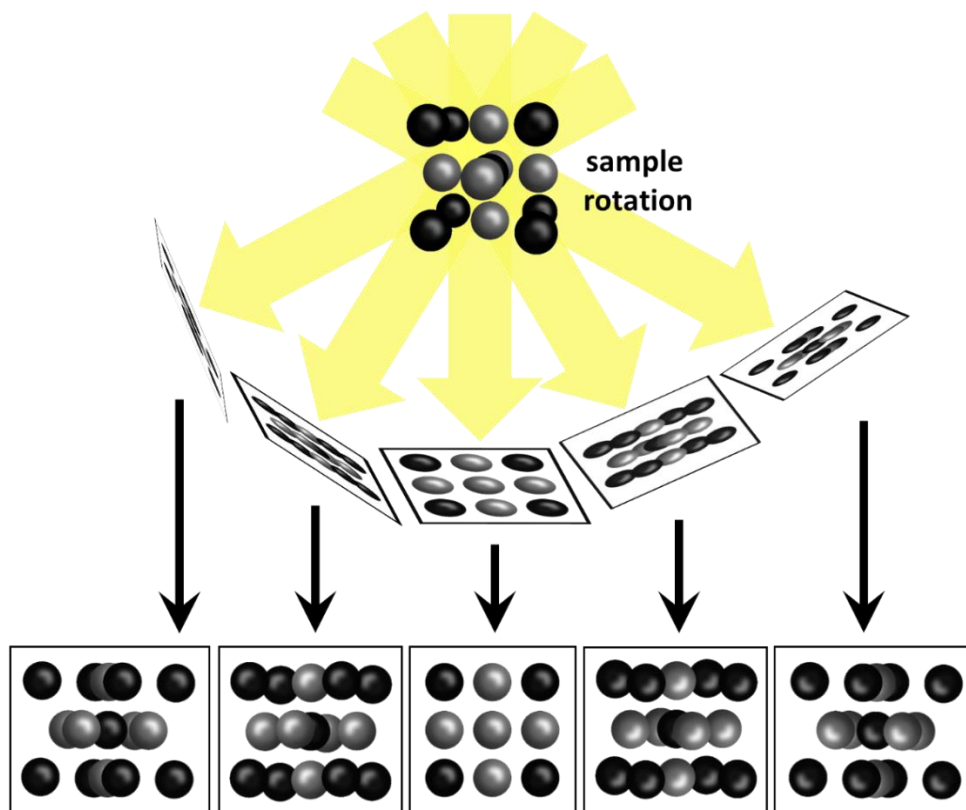


**Figure 2.12.** Conceptual diagram for image capturing accompanied by continuous tilts.

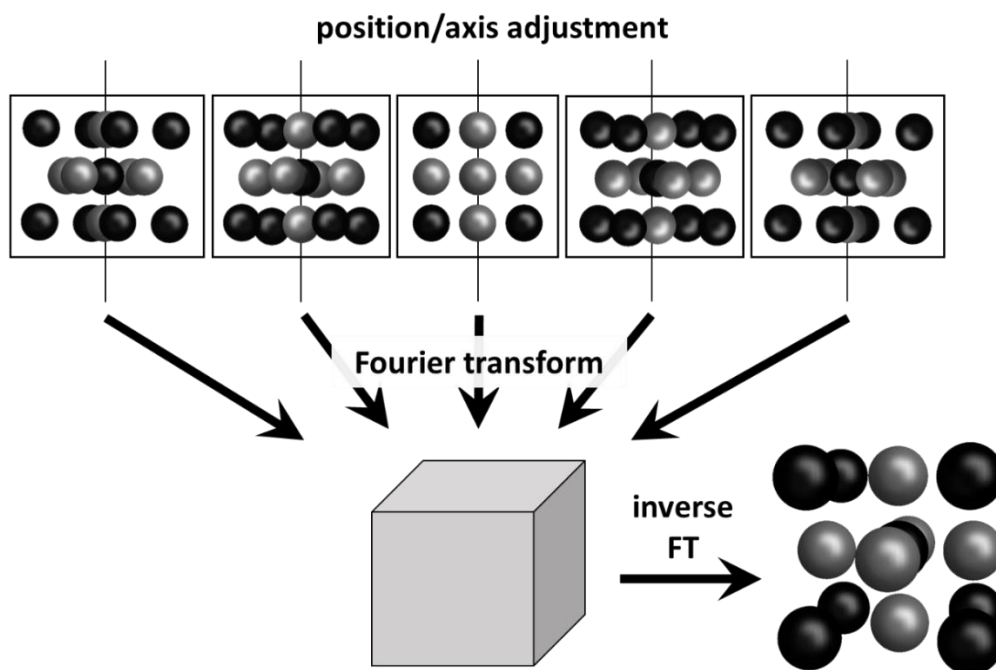


**Figure 2.13.** Conceptual diagram for 3D reconstruction of the aligned micrographs.

### 2.2.7 Small Angle X-ray Scattering (SAXS)

Small-Angle X-ray scattering (SAXS) is a widely-used diffraction technique to probe the nanostructures in soft matters with large scale fluctuations.<sup>24-26</sup> Conceptually, a SAXS experiment is simple: a sample is irradiated with X-rays and the scattered radiation is detected by a detector, as is shown in Figure 2.14. The scattered X-ray derives from the interactions between the incident X-ray and the electrons in a sample, thus, the X-ray beam is sensitive to spatial variations in electron density and can scatter from any interface that has a change in electron density, such as polymer-polymer, polymer-solvent, or solid-pore interfaces. The stronger the contrast in electron density, the higher is the intensity of the scattered beam goes up.

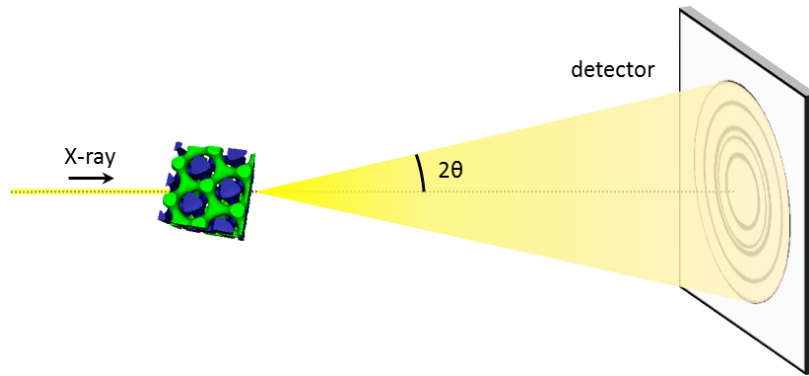


**Figure 2.14.** Schematic illustration of a SAXS apparatus depicting the incident, scattered and transmitted X-ray beams, with the definition of the scattering angle ( $2\theta$ ).

Here reviews the basic principles of X-ray scattering and the related mathematical formulations used in this study.

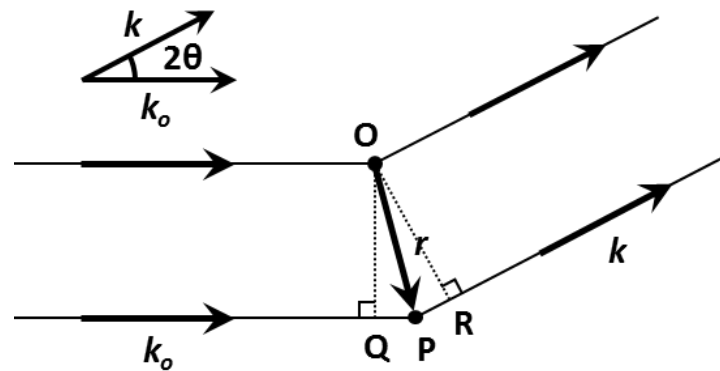


**Figure 2.15.** Schematics for path difference in general scattering experiments.

Figure 2.13 depicts the geometry of the path difference of the scattered waves where the incident X-ray beam described by its wavevector  $k_o$  ( $|k_o| = 2\pi/\lambda$ ) interacts with two bodies (electrons) located at the points O and P. The combined wave amplitude at the detector is the sum of the scattered waves from O and P that have the path difference of  $\overline{QP} + \overline{PR}$ . The phase difference  $l$  is denoted as

$$l = -k_o \cdot r + k \cdot r = -q \cdot r \quad (2-4)$$

where vector  $q$  which is referred to the scattering vector, is defined as

$$\mathbf{q} = \mathbf{k}_0 - \mathbf{k} \quad (2-5)$$

and the absolute value of  $\mathbf{q}$ ,  $|\mathbf{q}| = q$  as a scalar, can be obtained geometrically from Figure 2.15 as

$$q = |\mathbf{q}| = \frac{4\pi}{\lambda} \sin \theta \quad (2-6)$$

On the other hand, if the distance of two scattering bodies is  $D$ , we have the most basic Bragg law as

$$n\lambda = 2D \sin \theta \quad (2-7)$$

Combining eqs. (2-6) and (2-7), we have the following simple relationship

$$D = \frac{2n\pi}{q} \quad (2-8)$$

In X-ray scattering experiments, the scattering interferences for a multi-particle system can be grouped into two kinds: intra-particle and inter-particle interferences. In general, the scattering intensity  $I(\mathbf{q})$  can be expressed as the product of the structure factor  $S(\mathbf{q})$  and the form factor  $P(\mathbf{q})$  as,

$$I(\mathbf{q}) \propto S(\mathbf{q})P(\mathbf{q}) \quad (2-9)$$

The form factor  $P(\mathbf{q})$  can be written as the product of the Lorentz factor, and the thickness or cross-section scattering function,  $P_t(\mathbf{q})$

$$P(\mathbf{q}) = (2\pi A/q^2)P_t(\mathbf{q}) \quad (2-10)$$

where  $A$  denoted the area of the basal plane.

The form factor for homogeneous solid spheres of radius  $R$  is well-known as

$$P_{sphere}(q, R) = \left[ 3 \frac{\sin qR - qR \cos qR}{(qR)^3} \right]^2 \quad (2-11)$$

The expression for a cylinder with radius  $R$  and length  $2L$  can be expressed as

$$P_{cylinder}(q, R) = \int_0^{\pi/2} \frac{\sin^2(qL \cos \alpha)}{(qL \cos \alpha)^2} \frac{4J_1^2(qR \sin \alpha)}{(qR \sin \alpha)^2} \sin \alpha \, d\alpha \quad (2-12)$$

where  $\alpha$  is the angle between the normal to the particle and the scattering vector  $\mathbf{q}$ , and  $J_1$  is

the first order Bessel function.

On the other hand, the structure factor  $S(\mathbf{q})$  derives from the spatial relationship between the scattering substances and accounting for lattice disorder,

$$S(\mathbf{q}) = 1 + n4\pi \int (g(\mathbf{r}) - 1) \frac{\sin qr}{qr} r^2 d\mathbf{r} \quad (2-13)$$

where  $g(\mathbf{r})$  is the pair correlation function.

Table 2.2 summarizes the allowed peak ratios of established equilibrium morphologies for 2-component systems.

**Table 2.2** Peak Ratios of the Typical Block Copolymer Morphologies.

Morphology	Allowed Peak Ratios
Lamella	1, 2, 3, 4, 5....
Double Gyroid	$\sqrt{6}$ , $\sqrt{8}$ , $\sqrt{14}$ , $\sqrt{16}$ $\sqrt{20}$ ....
Hexagonal Cylinders	1, $\sqrt{3}$ , $\sqrt{4}$ , $\sqrt{7}$ , $\sqrt{9}$ , $\sqrt{12}$ ....
BCC sphere	1, $\sqrt{2}$ , $\sqrt{3}$ , $\sqrt{4}$ , $\sqrt{5}$ , $\sqrt{6}$ ....

### 2.2.8 Microbeam Small Angle X-ray Scattering ( $\mu$ -SAXS)

SAXS experiments using microbeam X-ray apparatuses have been developed to observe nanostructures in polymeric materials.<sup>27-29</sup> They provide structural information on a target sample without interference from other structures. As a result, they were used to study the local arrangement of the smectic layers<sup>30</sup>, characteristic cylindrical structures from star-shaped terpolymers<sup>31-32</sup> and the spatial inhomogeneity of a single bilateral wool fiber and so on..<sup>33</sup> Although TEM and conventional SAXS experiments, where X-ray beam size is larger than 500 $\mu$ m diameter, are useful for exploring micro- and nano-structures, the information

obtained is limited. In fact, Conventional SAXS experiments obtain the information of structure averaged over the irradiated area of the sample. Figure 2.16 compares the conventional SAXS and  $\mu$ -SAXS experiments.

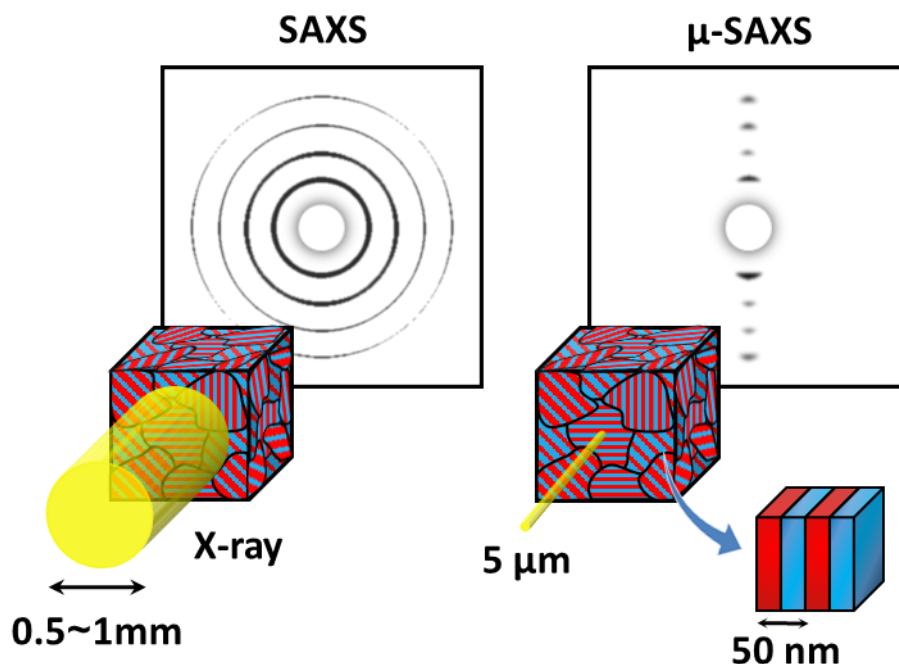


**Figure 2.16.** Schematic illustration of the comparison between conventional SAXS and  $\mu$ -SAXS experiments.

Recent developments of X-ray focusing optics and the high-flux synchrotron light sources have made possible to use an intense X-ray microbeam. In this thesis, all experiments for  $\mu$ -SAXS were performed at BL40XU (High Flux Beamline) of the SPring-8 (Hyogo, Japan) facility. A high-flux beam from a helical undulator was focused with two mirrors laid horizontally and vertically.<sup>34</sup> An high-resolution X-ray beam of 5 $\mu$ m (FWHM) in diameter was obtained with the aid of two pinholes, the first 5  $\mu$ m in diameter and the second 100 $\mu$ m in diameter. The sample-to-detector distance was about 3.0 m, calibrated using a collagen. X-ray

diffraction profiles in a two-dimensional detector are recorded with a CCD camera (1344×1024 pixels), the X-ray beam being monochromated at 0.153 nm (8.08 keV).

As for sample preparation, the annealed bulk films were cut into thin slices with ca. 5~10 μm thickness by using an ultramicrotome. The slices were floated on water surface and then transferred onto a Cu double slit grid that was sprayed with an adhesive beforehand.

## 2.3 References

1. Szwarc, M.; Levy, M.; Mikovich, R. Polymerization Initiated by Electron Transfer to Monomer. A New Method of Formation of Block Polymers. *J. Am. Chem. Soc.* **1956**, 78, 2656.
2. Szwarc, M. "Living" Polymers. *Nature* **1956**, 67, 1519.
3. Baskaran, D.; Muller, A. H. E. Anionic vinyl polymerization – 50 years after Michael Szwarc. *Prog. Polym. Sci.* **2007**, 32, 173-219.
4. Atsushi Noro. Doctor's Thesis. Nagoya University, 2006.
5. Mogi, Y.; Kotsuji, H.; Kaneko, Y.; Mori, K.; Matsushita, Y.; Noda, I. Preparation and Morphology of Triblock Copolymers of the ABC Type. *Macromolecules* **1992**, 25, 5408–5411.
6. Matsushita, Y.; Shimizu, K.; Nakao, Y.; Choshi, H.; Noda, I.; Nagasawa, M. Studies of Styrene and 2-Vinylpyridine Block Copolymers; Preparation and Characterization. *Polym. J.* **1986**, 18, 361.
7. Matsushita, Y.; Choshi, H.; Fujimoto, T.; Nagasawa, M. Preparation and Morphological Properties of a Triblock Copolymer of the ABC Type. *Macromolecules* **1980**, 13, 1053.
8. Fujimoto, T.; Ozaki, N.; Nagasawa, M. Study of the Effects of Additives in Homogeneous Anionic Polymerization of  $\alpha$ -Methylstyrene by n-Butyllithium (To Prepare Polymers Having Narrow Molecular Weight Distribution) *J. Polym. Sci., A.* **1965**, 3, 2259.
9. Matsushita, Y.; Furuhashi, H.; Choshi, H.; Noda, I.; Nagasawa, M.; Fujimoto, T.; Han, C. C. Preparation and Characterization of Block Copolymers of Ordinary and Deuterated Styrenes. *Polym. J.* **1982**, 14, 489.
10. Teraoka, I. *Polymer Solutions.*; Wiley-Interscience: New York, 2002.
11. Pasch, H.; Trathnigg, B. *HPLC of Polymers.*; Springer: Berlin, 1998.
12. Keeler, J. *Understanding NMR Spectroscopy*, 2<sup>nd</sup> ed.; Wiley-Interscience: New York, 2010.
13. Brandrup, J.; Immergut, E. H.; Grulke, E. A.; Abe, A.; Bloch, D. R. *Polymer Handbook*, 4<sup>th</sup> ed.; Wiley-Interscience: New York, 1999.
14. Worsfold, D. J.; Bywater, S. Anionic Polymerization of Isoprene. *Can. J. Chem.* **1964**, 42, 2884-2892.

## Chapter 2

15. Mark, J E. *Physical Properties of Polymers Handbook*, 2<sup>nd</sup> ed.; Springer: Berlin, 2007.
16. Williams, D. B.; Carter, C. B. *Transmission Electron Microscopy*, 2<sup>nd</sup> ed.; Springer: Berlin, 2009.
17. Trent, J. S.; Couchman, P. R.; Scheinbeim, J. I. *Transmission Electron Microscope Studies of Polymers Stained with Ruthenium and Osmium Tetroxide.*; Springer: Berlin, 1983.
18. Echlin, P. *Handbook of Sample Preparation for Scanning Electron Microscopy and X-Ray Microanalysis.*; Springer: Berlin, 2009.
19. Trent, J. S.; Scheinbeim, J. I.; Couchman, P. R. Ruthenium Tetraoxide Staining of Polymers for Electron Microscopy. *Macromolecules* **1983**, 16, 589-598.
20. Trent, J. S. Ruthenium Tetraoxide Staining of Polymers; New Preparative Methods for Electron Microscopy. *Macromolecules* **1984**, 17, 2930-2931.
21. Matsushita, Y.; Hayashida, K.; Takano, A.; Jewelry Box of Morphologies with Mesoscopic Length Scales - ABC Star shaped Terpolymers. *Macromol. Rapid. Commun.* **2010**, 31, 1579-1587.
22. Jinnai, H.; Jiang, X. Electron tomography in soft materials. *Curr. Opin. Solid State Mater. Sci.* **2013**, 17, 135-142.
23. Hayashida, M.; Malac, M.; Practical electron tomography guide: Recent progress and future opportunities. *Micron* **2016**, 91, 49-74.
24. Borsali, R.; Pecora, R. *Soft Matter Characterization.*; Springer: Berlin, 2008.
25. Feigin, L. A.; Svergun, D. I. *Structure Analysis by Small-Angle X-Ray and Neutron Scattering.*; Plenum Press: New York, 1987.
26. Glatter, O.; Kratky, O. *Small Angle X-ray Scattering.*; Academic Press. 1982.
27. Dreher, S.; Zachmann, H. G.; Riekkel, C.; Engstrom, P. Determination of the Chain Orientation in Liquid Crystalline Polymers by Means of Microfocus X-ray Scattering Measurements. *Macromolecules* **1995**, 28, 7071-7074.
28. Nozue, Y.; Kurita, R.; Hirano, S.; Kawasaki, N.; Ueno, S.; Iida, A.; Nishi, T.; Amemiya, Y. Spatial distribution of lamella structure in PCL/PVB band spherulite investigated with microbeam small- and wide-angle X-ray scattering. *Polymer* **2003**, 44, 6397-6405.
29. Kajiura, Y.; Watanabe, S.; Itou, T.; Iida, A.; Shinohara, Y.; Amemiya, Y. Structural analysis of single wool fibre by scanning microbeam SAXS. *J. Appl. Crystallogr.* **2005**, 38, 420.
30. Gurke, I.; Wutz, C.; Gieseler, D.; Janssens, B.; Heidelberg, F.; Riekkel, C.; Kricheldorf, H. R. Micro-focus X-ray scanning on layers of smectic superstructures. *J. Appl. Crystallogr.* **2000**, 33, 718.
31. Hayashida, K.; Kawashima, W.; Takano, A.; Shinohara, Y.; Amemiya, Y.; Nozue, Y.; Matsushita, Y. Archimedean Tiling Patterns of ABC Star-Shaped Terpolymers Studied by Microbeam Small-Angle X-ray

## Chapter 2

- Scattering. *Macromolecules* **2006**, 39, 4869-4872.
32. Hayashida, K.; Dotera, T.; Takano, A.; Y.; Matsushita, Y. Polymeric Quasicrystal Mesoscopic Quasicrystalline Tiling in ABC Star Polymers. *PRL*. **2007**, 98, 195502.
  33. Ohta, N.; Oka, T.; Inoue, K.; Yagi, N.; Kato, S.; Hatta, I. Structural analysis of cell membrane complex of a hair fibre by micro-beam X-ray diffraction. *J. Appl. Crystallogr.* **2005**, 38, 274.
  34. Inoue, K.; Oka, T.; Suzuki, T.; Yagi, N.; Takeshita, K.; Goto, S.; Ishikawa, T. Present status of high flux beamline (BL40XU) at SPring-8. *Nucl. Instrum. Methods* **2001**, A467-468, 674.

## CHAPTER 3

# Formation of Tetragonally-Packed Rectangular Cylinders from ABC Block Terpolymers Blends\*

\*Part of this work was published in “Yusuke Asai, Kotaro Yamada, Mutsuhiko Yamada, Atsushi Takano, Yushu Matsushita *ACS Macro Letters* **2014**, 3, 166-169.”

### 3.1 Introduction

Monodisperse block copolymers with chemically distinct components are known to form microphase-separated structures and a number of studies have been conducted by experimentally<sup>1-4</sup> and theoretically<sup>5-7</sup>. Common features of classical structures such as spherical, cylindrical and lamellar structures are shared by the fact that the polymer/polymer interfaces possesses the constant mean-curvature.

Lately-found somewhat more complex structures such as bicontinuous double gyroid structures for AB diblock copolymers,<sup>8,9</sup> tricontinuous double gyroid structures,<sup>10,11</sup> core-shell morphologies,<sup>12,13</sup> for ABC linear triblock terpolymers, and hierarchical structures in three-component multiblock terpolymers<sup>14</sup> have been known to show new morphological features. All these structures show mesoscopically-sized periodic morphologies, however in some cases such as gyroid structures, their mean curvatures show a significant deviation from the constant mean curvature as precisely reported for a two-component system.<sup>15</sup>

Even if diblock copolymers possess certain polydispersity, in general, they still generate simple and periodic structures due to the spontaneous and uniform mixing of the block copolymers. Hashimoto and coworkers studied the phase behaviors of binary blends of

poly(styrene-*b*-isoprene) (SI) with different compositions,<sup>16</sup> while Lynd and coworkers reported the polydispersity effect on the morphology of poly(ethylene-*alt*-propylene)-*block*-poly(DL-lactide) (PEP-PLA).<sup>17,18</sup> In addition, Noro and coworkers investigated the effects of composition distribution on morphologies of poly(styrene-*b*-2-vinylpyridine) (SP) diblock<sup>19</sup> and PSP triblock copolymer systems<sup>20</sup>. Thus, only light effects caused by the molecular weight or composition distribution on morphology were recognized for two-component block copolymer systems.

On the other hand, however, the situation is significantly different for linear ABC triblock terpolymers, because the B middle block chain has to bridge the A and C end-block components, in contrast to tail type conformation for AB diblock copolymers. The restriction of the chain conformation causes the morphological variation; symmetric ABC triblock terpolymers tend to produce alternating A and C domains embedded in a B matrix phase, suggesting that tetragonal-packed cylinders and BCC spheres are favorable in the symmetric triblock system.<sup>21-23</sup> As a more perturbed system, periodically undulated lamellae have been found in the poly(isoprene-*b*-styrene-*b*-2-vinylpyridine) (ISP) triblock terpolymer blend system with constant volume fractions ( $\phi_I=\phi_S=\phi_P$ ), but with large molecular weight distribution.<sup>24</sup> Furthermore, the morphological behavior of polydisperse poly(isoprene-*b*-styrene-*b*-ethylene oxide) (ISO) triblock terpolymers were investigated by X-ray technique.<sup>25</sup> The main aim of this chapter is the creation of morphologies with non-constant mean-curvatures (non-CMC) induced by composition distribution. The distribution was introduced by blending several ISP triblocks, all of which have the constant total molecular weights, but have different compositions. Tetragonal-packed rectangular-shaped cylinders have been found when the composition distribution exceeds a critical value.

## 3.2 Experiments and Measurements

### 3.2.1 Molecular design

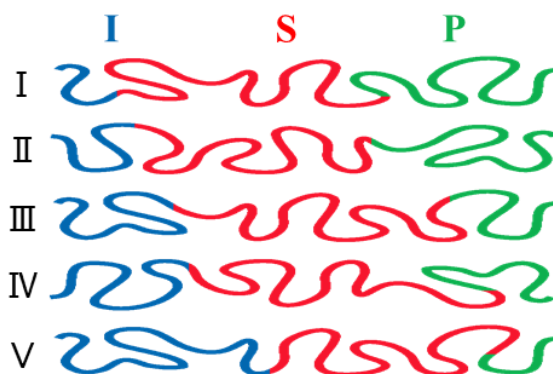
Preparation of poly(isoprene-*b*-styrene-*b*-2-vinylpyridine) (ISP) triblock terpolymer was carried out in the same way as mentioned in Chapter 2. Six ISP triblock terpolymers were synthesized via living anionic polymerization and characterized by SEC, <sup>1</sup>H-NMR, MALLS and Osmometry. Their molecular characteristics are listed in Table 3.1. The five samples from ISP-I to ISP-V are characterized by the almost same total molecular weight, the constant molecular weights of central S block but different chain lengths (compositions) of two end blocks. The schematic illustration of the five ISP triblocks are shown in Figure 3.1. Blending these polymers under a proper rule of blending ratio as listed on Table 3.2, provides the schematic investigation of the effect of composition distribution on the morphology. The sample names of the blend samples are identified as their composition distribution indices (CDI). CDI are calculated in the same way as Noro's works.<sup>19,20</sup> Here the molecular weight distribution of I component is chosen as CDI assuming the parent ISP triblocks used in this study are perfectly monodisperse. All the blend samples were prepared to be the volume fractions similar as  $\phi_I/\phi_S/\phi_P = 0.25/0.54/0.21$ . The volume fractions of the blend samples are listed in Table 3.3. It should be stressed that a neat ISP triblock terpolymer (ISP-III) with  $\phi_I/\phi_S/\phi_P = 0.24/0.55/0.21$  shows the tricontinuous double gyroid structure as shown in Figure 3.2 (c).<sup>26</sup>

**Table 3.1.** Molecular Characteristics of the Parent ISP Triblock Terpolymers

Sample Name	$M_n^a$ ( $\times 10^3$ )	$\phi_I^b$	$\phi_S^b$	$\phi_P^b$	$M_w/M_n^c$
 ISP-I	126	0.08	0.52	0.40	1.03
 ISP-II	121	0.13	0.55	0.32	1.05
 ISP-III	150	0.24	0.55	0.21	1.07
 ISP-IV	134	0.34	0.55	0.1	1.04
 ISP-V	124	0.39	0.56	0.05	1.06
 ISP-VI	122	0.06	0.62	0.32	1.02

<sup>a</sup> Determined by osmometry. <sup>b</sup> Determined by <sup>1</sup>H-NMR spectroscopy and the densities of I, S and P at room temperature ( $\rho_I$ : 0.926,  $\rho_S$ : 1.05,  $\rho_P$ : 1.14 g/cm<sup>3</sup>). <sup>c</sup> Estimated from a SEC chromatogram whose elution volumes were calibrated with polystyrene standards.

*\*The samples from ISP-I to ISP-VI used in this chapter correspond to ISP66, ISP57, ISP53, ISP58, ISP61 and ISP70, respectively, in Table 2.1\**

**Figure 3.1.** Schematic representation of the five ISP triblock terpolymers used in this study.

Blue, red, and green chains represent I, S, and P components, respectively.

**Table 3.2.** Blending Manners of the Five Parent Triblocks.

Sample Name/ Composition distribution	weight ratio				
	ISP-I	ISP-II	ISP-III	ISP-IV	ISP-V
1.27	1	1	1	1	1
1.31	2	1.5	1	1.5	2
1.36	8	4	1	4	8
1.51	1	0	0	0	1

Sample names share the same name with the values of composition distribution, which is defined as those of polyisoprene blocks of the blend.

**Table 3.3.** Volume Fractions of The Blending Samples, Whose Volume Fractions Are Almost Equivalent to ISP-III.

Sample Name	$\varphi_I$	$\varphi_S$	$\varphi_P$
1.27	0.25	0.54	0.21
1.31	0.25	0.54	0.21
1.36	0.25	0.54	0.21
1.51	0.25	0.54	0.21

### 3.2.2 Preparation for blend samples

Blend samples were prepared according to the rule listed in Table 3.2. As a first step, the ISP series were blended in tetrahydrofuran (THF)(5 wt%) without a stabilizer such as dibutylhydroxytoluene (BHT) and stirred for one day at room temperature to be blended homogeneously. THF is a non-selective solvent for all components. The solution was transferred into a Teflon beaker and the beaker was placed in a glass jar. The solution was evaporated slowly for three days and dried thoroughly in vacuo. Then, the resulting films were

thermally treated at 150°C for longer than four days under vacuum.

### 3.2.3 Measurements

For TEM observations, several small pieces of the annealed bulk films were embedded in an epoxy resin and cured for 9 hours at 60°C. The embedded samples were ultramicrotomed to a thickness of 50 ~ 90 nm at room temperature. The ultrathin sections were collected on a copper 300 mesh grid and then they were stained with OsO<sub>4</sub> for 2 hours at 70°C and I<sub>2</sub> for 2 hours at 50°C. Detail of the staining apparatus is shown in Chapter 2. OsO<sub>4</sub> gives a strong contrast for the I component, and I<sub>2</sub> selectively stains the P component. By twostep staining with both the reagents, the I component obtains the strongest contrast and the P component earns the mid contrast; that is, dark, white, and gray contrasts represent I, S, and P phases, respectively. TEM experiments were performed with JEM-1400 of JEOL Ltd. operated at an accelerating voltage of 120 kV and H-800 of HITACHI operated at accelerating voltage from 100 ~200 kV, changing the voltage according to the film thickness.

To investigate three-dimensional microdomain structures, a transmission electron microscopy tomography (TEMT) experiment was carried out using a JEM-1400 of JEOL Ltd., being operated at an acceleration voltage of 120 kV. The film preparation for TEMT experiments is somewhat different from that for conventional TEM observations, as is mentioned in Chapter 2. The annealed bulk films were immersed and stained with OsO<sub>4</sub> 5 wt% aqueous for 2 hours at 70°C before embedding. The ultrathin sections having about 200 nm thickness were prepared using an ultramicrotomed. 200 nm thickness is thick enough to confirm the three dimensional alignment of cylindrical domains. The thin sections on a Cu grid were stained with OsO<sub>4</sub> for an hour at 70°C again not to leave unstained region. The both sides of the grid was coated with carbon using a vacuum deposition equipment (SVC-700, SANYU Electron. Co., Ltd.). A series of a total of 101 TEM images were collected with tilt

## Chapter 3

angles ranging from  $-50^\circ$  to  $+50^\circ$  in  $1^\circ$  increment using a specimen rotating holder. The series of TEM images were aligned by the fiducial marker method using the Au nanoparticles (10 nm) as markers. The collected TEM images were reconstructed by using a reconstruction software, Composer, and a visualization and modeling software, Visualizer, both of JEOL System Technology Co., Ltd.

SAXS experiments were conducted using beamline 10C at Photon Factory (Tsukuba, Japan). Two dimensional SAXS patterns were recorded on an automated imaging plate detector (R-AXIS IV++, pixel size =100  $\mu\text{m}$ ). The instrument was calibrated using a silver behenate powder as a standard. The wavelength of the X-ray and the sample-to-detector distance were 0.1508 nm ( $\text{CuK}\alpha$ ) and ca. 2000 mm, respectively. Unless otherwise noted, SAXS experiments were performed for small sample pieces cut from the annealed bulk films, where X-ray was irradiated from the direction parallel to film surface.

Microbeam SAXS ( $\mu$ -SAXS) experiments were performed at high flux beamline BL40XU at SPring-8 (Hyogo, Japan). The wavelength of X-ray was 0.1 nm, and the size of the X-ray microbeam was ca.  $5\ \mu\text{m} \times 5\ \mu\text{m}$  (fwhm). The camera length was fixed about 3 m, and the precise camera length was calibrated with a collagen standard sample. For the  $\mu$ -SAXS measurements, the annealed bulk films were cut into thin section of about 20  $\mu\text{m}$  thickness by using an ultramicrotome. The thin films were collected on a Cu grid with 4 slits (2 mm width with each slit). The grids were placed at the sample stage and X-ray was irradiated from the direction perpendicular to film surface. The scattering patterns were recorded with a CCD detector.

### 3.3 Results and Discussion

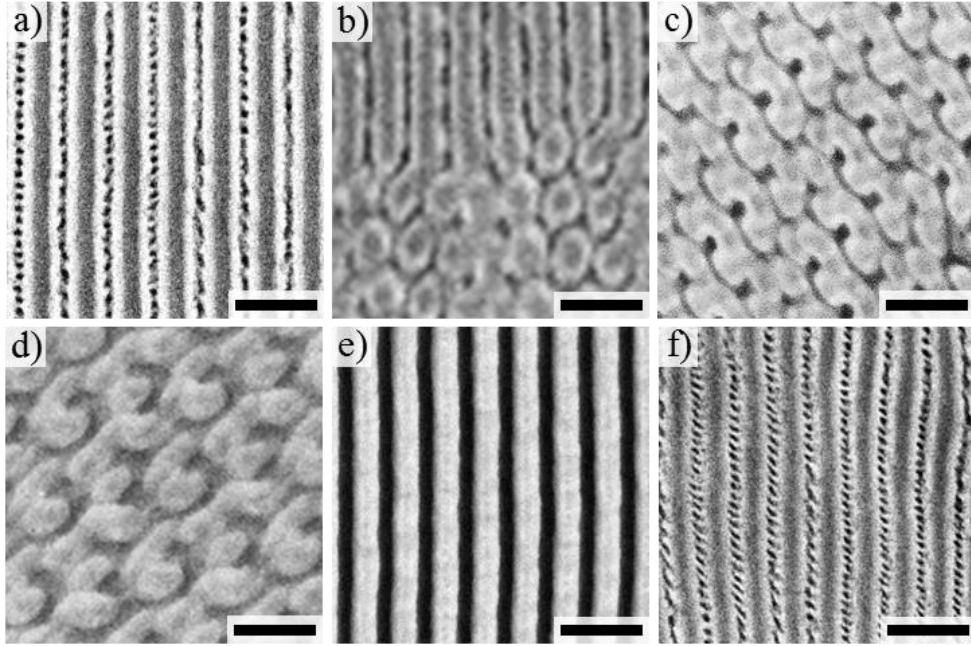
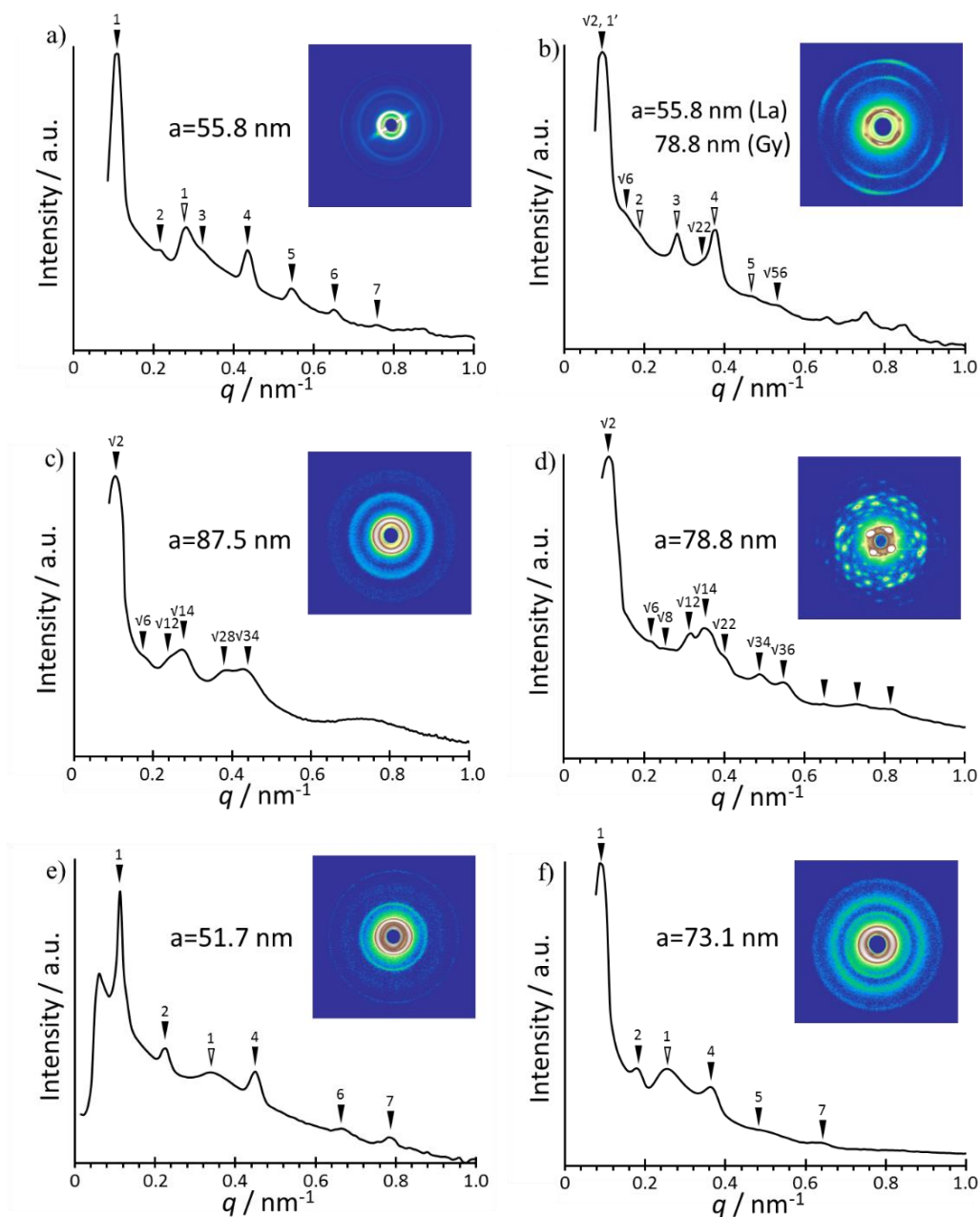


**Figure 3.2.** Comparison of microphase-separated structures for the six parent triblock terpolymers. Samples are a) ISP-I, b) ISP-II, c) ISP-III, d) ISP-IV, e) ISP-V and f) ISP-VI respectively. Scale bars all represent 100 nm.

Figure 3.2 compares the morphologies of the six parent ISP triblocks. In the TEM images, the black, white, and gray domains represent I, S, and P phases, respectively. The ISP-I ( $\phi_I/\phi_S/\phi_P = 0.08/0.52/0.40$ ) in Figure 3.2 (a) and ISP-VI ( $\phi_I/\phi_S/\phi_P = 0.06/0.62/0.32$ ) in Figure 3.2 (f) possess sphere-in-lamella structures, where the minor I component stays as isolated spheres at the center of lamellar domains of S component, and S and P phases exhibit alternative lamellae. These results are quite reasonable since the two parent ISP triblocks have highly asymmetric compositions of the end blocks: I and P, and the two components possess the highest interaction strength ( $\chi_{S-P} \gg \chi_{S-I} \cong \chi_{S-P}$ ). A sphere-in-lamella structure with P spheres located at the middle of S lamellae is also observed in ISP-V ( $\phi_I/\phi_S/\phi_P = 0.39/0.56/0.05$ ) shown in Figure 3.2(e), although it is somewhat difficult to see the isolated P

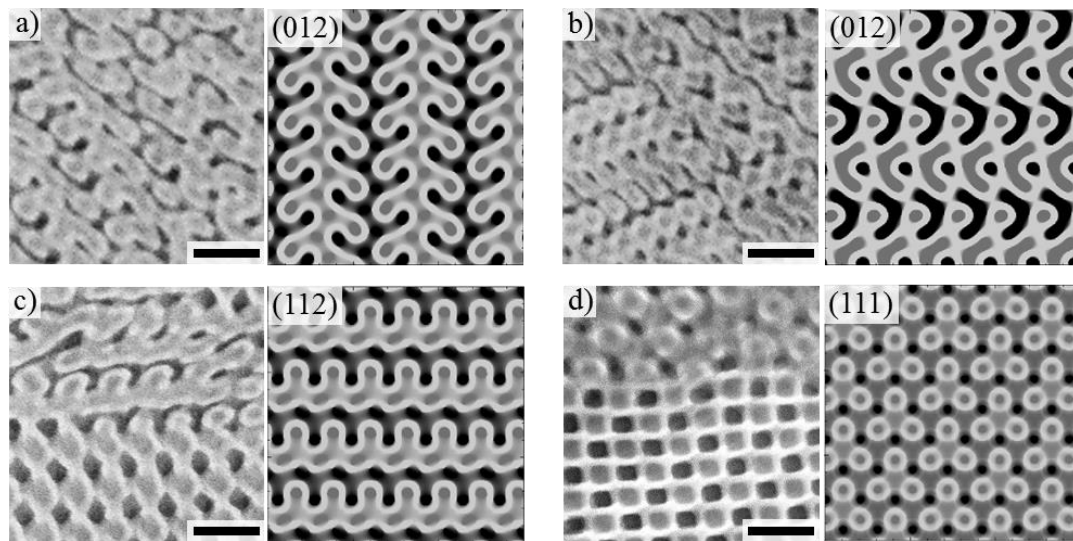
### Chapter 3

domains. The ISP-III ( $\phi_I/\phi_S/\phi_P = 0.24/0.55/0.21$ ) in Figure 3.2 (c) forms a tricontinuous double gyroid structure, which agrees well with the previous result for symmetric ISP triblock terpolymers.<sup>10,11,26</sup> However, the ISP-II and -IV, also exhibit tricontinuous double gyroid structures nevertheless the volume ratios of the end components, I/P for ISP-II and P/I for ISP-IV, are approximately three, but for ISP-II, a three-phase four-layer lamellar structure was also partially observed.



**Figure 3.3.** Azimuthally integrated SAXS patterns of the six parent triblock terpolymers. Samples are a) ISP-I, b) ISP-II, c) ISP-III, d) ISP-IV, e) ISP-V and f) ISP-VI respectively. The inset figures represent the corresponding 2D SAXS data. “a” expresses a unit cell size [nm] estimated from the primary peak of each sample. The inverted triangles point out the sequence of peaks. If the two types of structure exist, black and open inverted triangles are used.

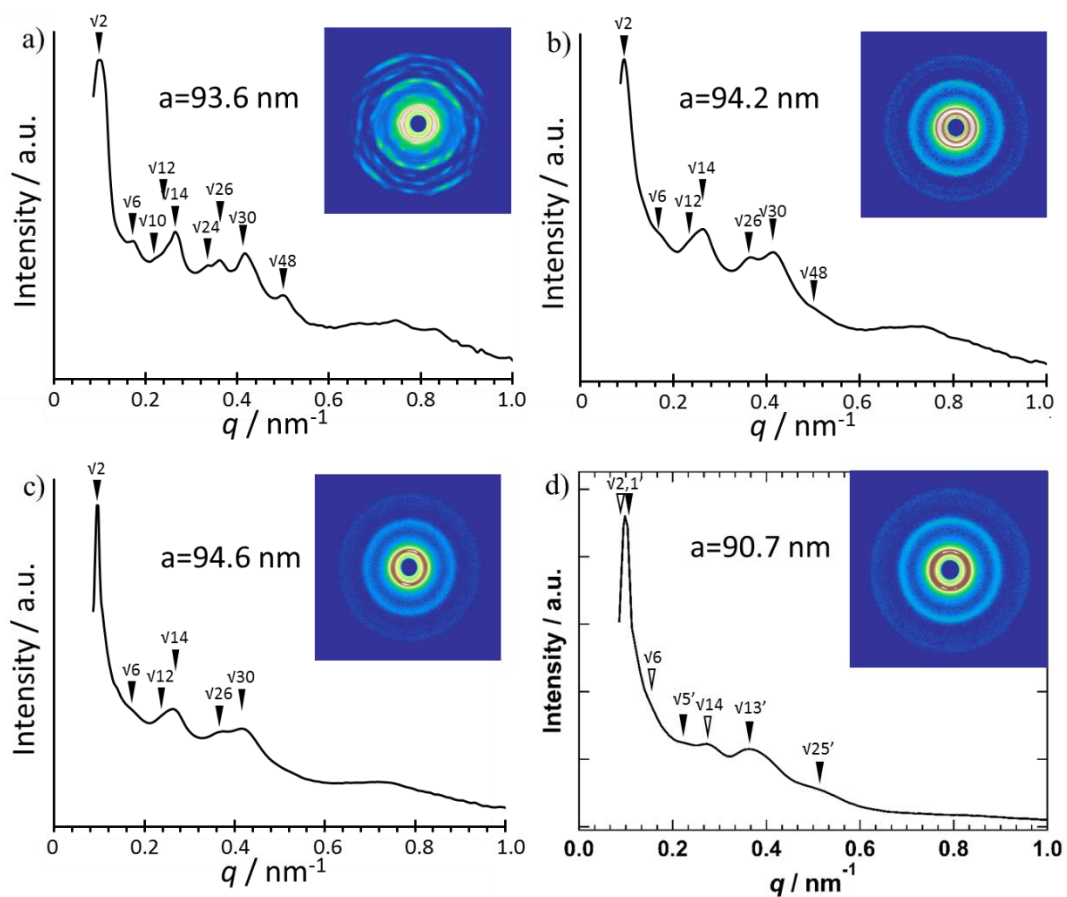
Figure 3.3 displays the SAXS patterns of the parent triblock terpolymers. The intensities on a two dimensional imaging plate were azimuthally integrated and circularly-averaged. For ISP-I, -V and -VI, ordered lamellar morphologies were assigned based on the presence and the location of higher order scattering peaks at integer multiples with respect to the primary peaks, however, the peaks (open inverted triangles) that do not follow the integer rule were observed at each scattering pattern. These peaks must be derived from the interferences of the small domains composed of the minor components (I component for ISP-I and -VI, P component for ISP-V). For ISP-III and -IV, the black inverted triangles indicate possible peak positions for a gyroid structure, whose peaks are observed at the relative magnitude of the scattering vectors of  $\sqrt{2}$ ,  $\sqrt{6}$ ,  $\sqrt{14}$ . On the other hand, the scattering pattern of ISP-II, in which lamellar and gyroid structures were confirmed by TEM, reveals two types of structure are obtained. The black inverted triangles contains a diffraction pattern with peaks  $q/q^* = \sqrt{2}, \sqrt{6}, \sqrt{22}$ , consistent with a gyroid structure. The open inverted triangles indicate probable peak positions of a lamellar structure. The two primary peaks are assumed to be overlapped. The SAXS result agrees well with that for the real space result in Figure 3.2 (b). Unit cell sizes of each sample determined by the primary peaks are in good accordance with the corresponding real space results in Figure 3.2.



**Figure 3.4.** TEM images of the blend samples with various composition distribution index (CDI), which are a) 1.27, b) 1.31, c) 1.36 and d) 1.51 respectively. Scale bars all represent 100 nm. Figures on the right side of each TEM image represent the computer-generated TEM simulation images for ordered tricontinuous double gyroid (OTDG) structure. The inset numbers exhibit the directions of projection performed for the calculations.

Figure 3.4 displays self-assembled structures of the blend samples and their corresponding TEM simulation results for tricontinuous double gyroid structure. Figure 3.4 (a) and (b) for the blend samples with CDIs of 1.27 and 1.31 exhibit gyroid structures. However, it is quite hard to identify the cocontinuous structures only from two-dimensional TEM images. Hence TEM simulation was performed for these samples. TEM simulation was carried out considering the direction of projection, volume fractions, film thickness and TEM contrasts and also assuming the cocontinuous structures possess tricontinuous state in which I and P component create alternative networks. The contrast in TEM simulation shows Black: I, Gray: P, White; S, which are the same with the TEM image. The detail of the TEM simulation process is mentioned in Chapter 6. The simulation TEM images of 1.27 and 1.31, which are obtained from (012) plane, sufficiently support that 1.27 and 1.31 possess the OTDG structure. In Figure 3.4 (c), two totally

different structures are obviously observed; one is an OTDG structure shown at the upper half of the image, the other is a very simple structure observed in the lower half of the image. The upper half image is typical for (112) projection for a gyroid structure. Note that the fraction of the simple structure, having I and P isolated domains alternated in a tetragonal arrangement, increases with increasing CDI as seen in Figure 3.4 (d), which is a binary blend of the ISP-I and -V. This structure with a tetragonal symmetry seems to be a periodical structure whose isolated domains form a rectangular shape instead of commonly known round one.



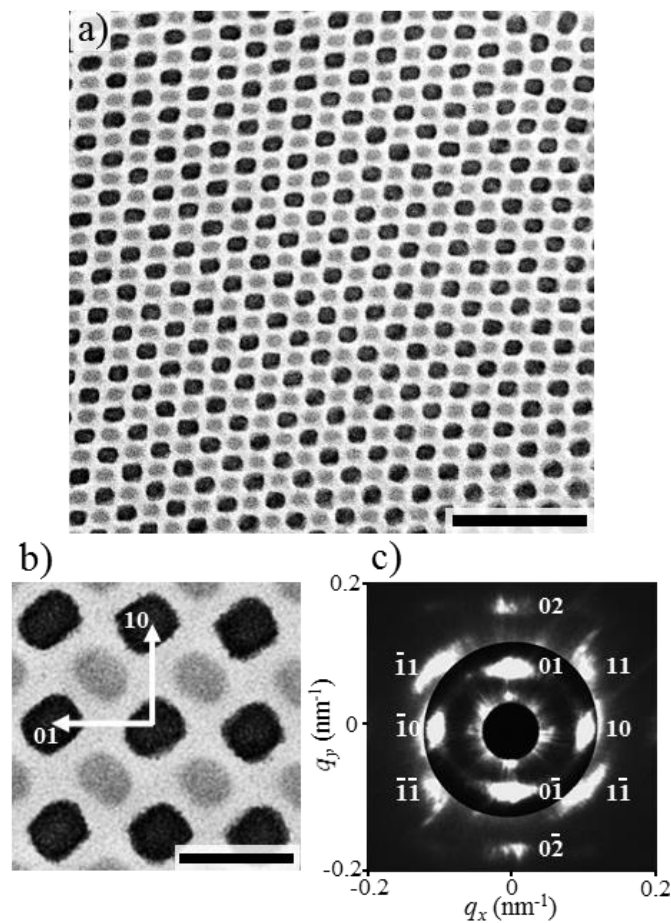
**Figure 3.5.** Azimuthally integrated SAXS patterns of the blend samples with various CDIs which are a) 1.27, b) 1.31, c) 1.36 and d) 1.51 respectively. The inset figures represent the corresponding 2D SAXS patterns.

Figure 3.5 shows the SAXS patterns of the blend samples with various CDIs. The peaks observed for 1.27, 1.31 and 1.36 have scattering wave vectors spacing-ratios of  $\sqrt{2}$ ,  $\sqrt{6}$ ,  $\sqrt{12}$ ,  $\sqrt{14}$ ...., consistent with an OTDG structure. However, the TEM image of 1.36 reveals the existence of two types of structure as shown in Figure 3.4 (c), suggesting the tetragonal domain orientation appears in a narrow region. For 1.51, the scattering pattern ensure the coexistence of two structures. The open inverted triangles indicate possible peak positions for a gyroid structure, whose peaks are observed at the relative magnitude of the scattering vectors of  $\sqrt{2}$ ,  $\sqrt{6}$ ,  $\sqrt{14}$ . The black inverted triangles indicate probable peak positions of a tetragonal domain orientation, whose peaks are observed at the relative magnitude of the scattering vectors of 1,  $\sqrt{5}$ ,  $\sqrt{13}$ ,  $\sqrt{25}$ . The primary peaks of the two structures are seems to be overlapped. The SAXS result is consistent with that for the real space image shown in Figure 3.4 (d).

It should be noted here that the unit lattice size (identified as “ $a$ ”) of OTDG increases as the CDI increases, except 1.51 which generates two types of structures. Interestingly, ISP-III with the narrowest CDI exhibits the smallest unit cell which is estimated to be 87.5 nm from the SAXS pattern shown in Figure 3.3 (c), although ISP-III has the largest total molecular weight of the parent polymers. It is entirely fair to state that the CDI significantly effects the morphological behavior. Noro *et al.*<sup>19,20</sup> and Lynd *et al.*<sup>17,18</sup> investigated the effects of the composition distribution and the molecular weight distribution on block copolymer self-assembly experimentally. They revealed that the increased breadth in the distribution indices emerges the increase in the domain spacing. The most likely explanation for this effect is that block copolymers blended with short and long chains could more efficiently fill space by using long chains to fill the center of the phase-separated domain and the decreased stretching entropy cost allows the domain to stretch further to minimize unfavorable segment-segment contacts at the interface, resulting in thick domain.

Turning now to the unusual structure with square domains obtained from 1.51. Based

on the TEM and SAXS results, the unique structure can be identified as a tetragonal-packed cylindrical morphology and concluded that the larger volume fraction of S component is necessary to stabilize the structure over the whole area based on general phase transition behavior. Hence, I prepared another binary blend with larger center block fraction; ISP-V ( $\phi_I/\phi_S/\phi_P = 0.39/0.56/0.05$ ) and ISP-VI ( $\phi_I/\phi_S/\phi_P = 0.06/0.62/0.32$ ). They were mixed with a weight ratio of ISP-V to ISP-VI of 1, as is the case with 1.51. The resulting volume fraction is  $\phi_I/\phi_S/\phi_P = 0.23/0.59/0.18$ ,  $\phi_S$  of which is larger than that of 1.51.



**Figure 3.6.** a) A typical TEM image over a wide range of the equimolar binary blend of ISP-V and ISP-VI. Scale bar represents 200 nm. b) A TEM image at high magnification (Scale bar: 50 nm). c) A  $\mu$ -SAXS diffraction pattern.

TEM and  $\mu$ -SAXS results of the binary mixture of ISP-V/-VI are summarized in Figure 3.6. From Figure 3.6 (a), it is clearly confirmed that tetragonal-packed cylindrical structure has been formed over a wide range. The TEM image at higher magnification shown in Figure 3.5 (b) reveals the rectangular cross-sections of I (black) and P (gray) domains align alternately on a tetragonal lattice. Figure 3.6 (c) shows a two-dimensional  $\mu$ -SAXS diffraction that clearly exhibits a 4-fold symmetry pattern. The domain distance between the nearest I-I or P-P domains is estimated to be 43 nm from the [10] (or [01]) diffraction. This value corresponds reasonably with the observed one, 46 nm in Figure 3.6 (b).

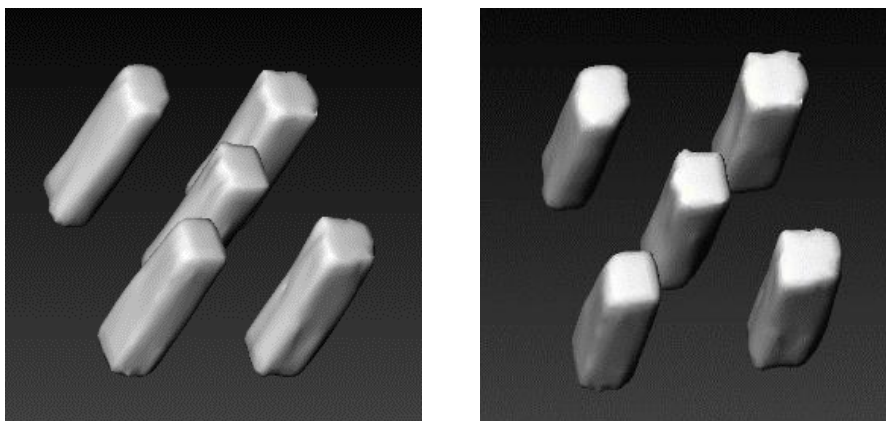


**Figure 3.7.** TEMT images reconstructed from 101 TEM images of the equimolar binary blend of ISP-V and ISP-VI stained with OsO<sub>4</sub>. The microdomains displayed in gray are composed of I component.

In order to evaluate the three-dimensional alignment of the specific domains with a rectangular shape, TEM tomography was performed. Reconstructed 3D TEM images of the equimolar binary mixture of ISP-V and ISP-VI are presented in Figure 3.7. The images reveal that I domains are penetrating through S matrix without any domain rotation, so it can be concluded that the present structure is a tetragonally-arranged “rod” structure. The I/S interface, probably P/S one as well, obviously show non-CMC, which is seldom found in

monodisperse block copolymers, but can be obtained in a triblock terpolymer system with relatively high molecular weight distribution<sup>24</sup> or complex blends with hydrogen bonding interaction between two chemical components as one block of copolymers.<sup>27,28</sup>

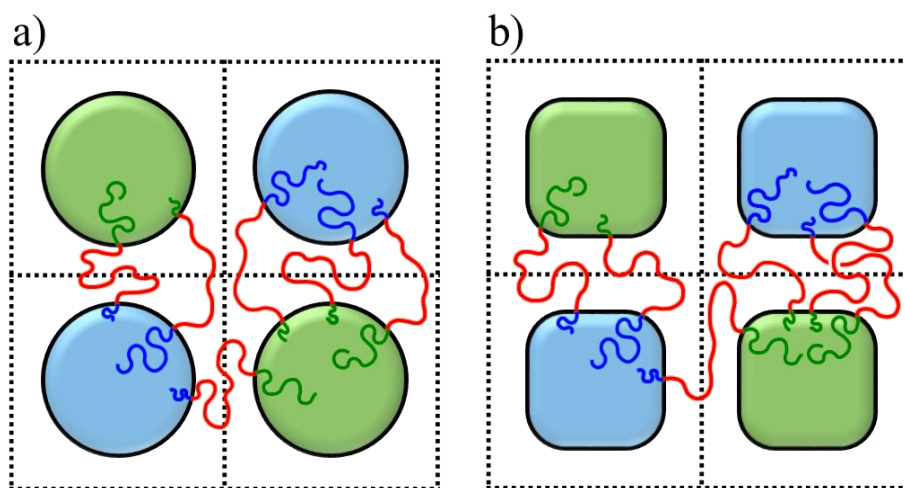


**Figure 3.8** a) and b) compare schematic illustrations of possible chain distribution in cylindrical and rod domains. When the binary chains with a large difference in block chain lengths are distributed uniformly in cylinders, the conformational entropy cost of three components could be large as shown in a). To relieve this frustration, two chains with different chain lengths might be localized, resulting in the rod domains as shown in b).

Figure 3.8 (a) and (b) schematically present possible chain arrangement of component polymers. Figure 3.8 (a) draws conventional round-shaped cylinders with a tetragonal manner, while Figure 3.8 (b) exhibits rod domains arranged tetragonally. Comparing these two illustrations, it can be noticed that the conformational entropy costs of two end blocks, that is, I and P chains distributed in independent domains, as well as middle S blocks in a matrix phase could be considerably large for the chain arrangement in Figure 3.8 (a). On the other hand, in Figure 3.8 (b), conformational entropy costs of I, P, and S chains can

be relieved due to the unusual rectangular shape by sacrificing the placement entropy of junction points from different molecules.

### 3.4 Conclusions

The effect of composition distribution of ABC linear terpolymers on the formation of periodic structures was investigated in this study. It was found that the tricontinuous gyroid structure gradually transforms into the cylindrical structure as increasing the composition distribution. For the largest distribution, where the blend system is actually the binary blend of ISP-I and ISP-V, rectangular-shaped domains with a tetragonal manner were partially observed. By tuning the volume fractions, co-arrayed tetragonal-packed rod domains were formed over a wide range. Bridging the present result with the previous one that is the study on molecular weight distribution<sup>23</sup>, it seems reasonable to conclude that the triblock terpolymer systems with fairly large distribution allow the domain interfaces with non-CMC to release the entropic cost by localizing each chain within domains. This is the specific feature of an ABC triblock terpolymer system that has never occurred in diblock copolymer systems.

### 3.5 References

- 1 Matsuo, M.; Sagae, S.; Asai, H. Fine Structures of Styrene-Butadiene Block Copolymer Films Cast from Toluene Solution. *Polymer* **1969**, 10, 78-87.
- 2 Inoue, T.; Soen, T.; Hashimoto, T.; Kawai, H. Thermodynamic Interpretation of Domain Structure in Solvent-Cast Films of A-B Type Block Copolymers of Styrene and Isoprene. *J. Polym. Sci. Part A-2* **1969**, 7, 1283-1302.
- 3 Matsushita, Y.; Choshi, H.; Fujimoto, T.; Nagasawa, M. Preparation and Morphological Properties of a Triblock Copolymer of the ABC Type. *Macromolecules* **1980**, 13, 1053-1058.
- 4 Richards, R. W.; Thomason J.L. A small angle neutron scattering investigation of block copolymers of styrene and isoprene in the solid state. *Polymer* **1981**, 22, 581-589.

## Chapter 3

- 5 Helfand, E.; Wasserman, Z. R. Block Copolymer Theory. 4. Narrow Interphase Approximation. *Macromolecules* **1976**, 9, 879-888.
- 6 Ohta, T.; Kawasaki, K. Equilibrium morphology of block copolymer melts. *Macromolecules* **1986**, 19, 2621-2632
- 7 Matsen, M. W.; Schick, M. Stable and unstable phases of a diblock copolymer melt. *Phys Rev Lett* **1994**, 72, 2660-2663.
- 8 Hadjuk, D. A.; Harper, P. E.; Gruner, S. M.; Honeker, C.C.; Kim, G.; Thomas, E.L The Gyroid A New Equilibrium Morphology in Weakly Segregated Diblock Copolymers. *Macromolecules*, **1994**, 27, 4063-4075.
- 9 Hasegawa, H.; Tanaka, H.; Yamasaki, K.; Hashimoto, T. Bicontinuous Microdomain Morphology of Block Copolymers. 1. Tetrapod-Network Structure of Polystyrene-Polyisoprene Diblock Polymers. *Macromolecules* **1987**, 20, 1651-1662.
- 10 Suzuki, J.; Seki, M.; Matsushita, Y. The tricontinuous double-gyroid structure from a three-component polymer system. *J. Chem.Phys.* **2000**, 112, 4862-4868.
- 11 Suzuki, J.; Nakane, K.; Takano, A.; Matsushita, Y. Self-assembly template during morphological transition of a linear ABC triblock copolymer from lamellar to Gyroid structure. *Polymer* **2004**, 45, 8989-8997.
- 12 Breiner, U.; Krappeb, U.; Abetz, V.; Stadler, R. Cylindrical morphologies in asymmetric ABC triblock. *Macromol. Chem. Phys.* **1997**, 198, 1051-1083.
- 13 Shefelbine, T. A.; Vigild, M. E.; Matsen, M. W.; Hajduk, D. A.; Hillmyer, M. A. Cussler, E. L.; Bates, F. S. Core-Shell Gyroid Morphology in a Poly(isoprene-block-styrene-block-dimethylsiloxane) Triblock Copolymer. *J. Am. Chem. Soc.* **1999**, 121, 8457-8465.
- 14 Masuda, J.; Takano, A.; Nagata, Y.; Noro, A.; Matsushita Y. Nanophase-Separated Synchronizing Structure with Parallel Double Periodicity from an Undecablock Terpolymer. *Phys. Rev. Lett.* **2006**, 97, 098301.
- 15 Sato, H.; Yoshinaga, M.; Mihara, T.; Nishi, T.; Jinnai, H. The interface dynamics of bicontinuous phase separating structure in a polymer blend. *J. Phys: Conf. Ser.* **2009**, 184, 012029.
- 16 Chen, F.; Kondo, Y.; Hashimoto, T. Control of Nanostructure in Mixtures of Block Copolymers Curvature Control via Cosurfactant Effects. *Macromolecules* **2007**, 40, 3714-3723.
- 17 Lynd, N. A.; Hillmyer, M. A. Influence of Polydispersity on the Self-Assembly of Diblock Copolymers. *Macromolecules* **2005**, 38, 8803-8810.
- 18 Lynd, N. A.; Meuler, A.; Hillmyer, M. A. Polydispersity and block copolymer self-assembly. *Prog. Polym. Sci.* **2008**, 33, 875-893.
- 19 Matsushita, Y.; Noro, A.; Iinuma, M.; Suzuki, J.; Ohtani, H.; Takano, A. Effect of Composition Distribution on Microphase-Separated Structure from Diblock Copolymers. *Macromolecules* **2003**, 36, 8074-8077.

## Chapter 3

- 20 Noro, A.; Inuma, M.; Suzuki, J.; Takano, A.; Matsushita, Y. Effect of Composition Distribution on Microphase-Separated Structure from BAB Triblock Copolymers. *Macromolecules* **2004**, *37*, 3804-3808.
- 21 Mogi, Y.; Nomura, M.; Kotsuji, H.; Ohnishi, K.; Matsushita, Y.; Noda, I. Superlattice Structures in Morphologies of the ABC Triblock Copolymers. *Macromolecules* **1994**, *27*, 6755-6760.
- 22 Hardy, C. G.; Tang, C. Advances in Square Arrays Through Self-Assembly and Directed Self-Assembly of Block Copolymers. *J. Polym. Sci., Part B: Polym. Phys.* **2013**, *51*, 2-15.
- 23 Matsen, M. W. Gyroid versus double-diamond in ABC triblock copolymer melts. *J. Chem. Phys.* **1998**, *108*, 785-796.
- 24 Matsushita, Y.; Suzuki, J.; Izumi, Y.; Matsuoka, K.; Takahashi, S.; Y. Aoyama,; Mihira, Y.; Takano, A. Formation of undulated lamellar structure from ABC block terpolymer blends with different chain lengths. *J. Chem. Phys.* **2010**, *133*, 194901.
- 25 Meuler, A. J.; Ellison, C. J.; Qin, J.; Evans, C. M.; Hillmyer, M. A.; Bates, F. S. Polydispersity effects in poly(isoprene-b-styrene-b-ethylene oxide) triblock terpolymers. *J. Chem. Phys.* **2009**, *130*, 234903.
- 26 Matsushita, Y.; Suzuki, J.; Seki, M. Surfaces of tricontinuous structure formed by an ABC triblock copolymer in bulk. *Physica B* **1998**, *248*, 238-242.
- 27 Tang, C.; Lennon, E.M.; Fredrickson, G.H.; Kramer, E.J.; Hawker, C.J. Evolution of Block Copolymer Lithography to Highly Ordered Square Arrays. *Science* **2008**, *322*, 429-432.
- 28 Asari, T.; Matsuo, S.; Takano, A.; Matsushita, A. Three-Phase Hierarchical Structures from AB CD Diblock Copolymer Blends. *Macromolecules* **2005**, *38*, 8811-8815.

## CHAPTER 4

# Creation of Cylindrical Morphologies with Extremely Large Oblong Unit Lattices from ABC Block Terpolymer Blends

\*Part of this work was published in “Yusuke Asai, Atsushi Takano, Yushu Matsushita *Macromolecules* **2015**, 48, 1538-1542.”

### 4.1 Introduction

Block copolymers are composed of two or more covalent-bound chemically distinct polymers. Because of chemical incompatibility between the constituent block components, phase separation occurs in block copolymers, resulting in periodical microphase-separated structures such as lamellae, gyroids, cylinders and spheres. There are several important factors in determining which ordered structure is formed; the volume fraction ( $\phi$ ) of each component and segregation strength ( $\chi N$ ) where  $\chi$  is Flory's segmental interaction parameter and  $N$  is the total degree of polymerization.<sup>1,2</sup> A number of studies of monodisperse AB diblock copolymers have been conducted both theoretically<sup>3-5</sup> and experimentally.<sup>6-8</sup> Lately, ABC triblock terpolymers have attracted considerable attention because of the ability that they form complex structures such as core-shell cylinders<sup>9,10</sup>, tetragonal-packed cylinders<sup>11,12</sup>, and others interesting morphologies.<sup>13-17</sup> The morphological variety originates in a large number of controlling parameters; volume fractions ( $\phi_A$ ,  $\phi_B$ ,  $\phi_C$ ) and three interaction parameters ( $\chi_{AB}$ ,  $\chi_{AC}$ ,  $\chi_{BC}$ ), and block sequences (ABC, BAC, ACB). ABC triblock terpolymers basically

possess the domain interfaces with constant mean-curvature (CMC) to minimize the free energy.

However, some specific ordered structures having non-CMC have been observed in block copolymer blends with supramolecular interaction such as hydrogen bonding<sup>18,19</sup> and with particular distributions such as molecular weight distribution<sup>20</sup> and composition distribution.<sup>21</sup> Tang and coworkers presented the ordered square arrays with a tetragonal manner from blends of two diblock copolymers with hydrogen bonding,<sup>19</sup> and we have developed co-arrayed tetragonal-packed rod domains by binary blends of poly(isoprene-*b*-styrene-*b*-2-vinylpyridine) (ISP) triblock terpolymers with distinctly different chain lengths of the two end-blocks.<sup>21</sup> In addition, some morphologies with complex domain orientations have been observed in multicomponent systems with the specific chain topology<sup>22-25</sup> and polymer/polymer blends.<sup>26,27</sup> Hayashida and coworkers<sup>22,23</sup> and Bates and coworkers<sup>24,25</sup> have found Frank-Kasper  $\sigma$  phase and quasicrystals from ABC star-shaped terpolymers and ABAC tetrablock terpolymers, respectively. Recently, Izumi and coworkers have reported a cylindrical structure with a new tiling pattern where P domain are surrounded by 5 I domains, using ISP/S homopolymer blend.<sup>26</sup> According to their study, it has been concluded that the ratio of volume fractions of two end-blocks,  $\phi_P/\phi_I$ , is recognized as an indicator of packing state of cylinders.<sup>26</sup>

In the present study, I demonstrate the formation of two characteristic cylindrical morphologies with new tiling patterns and non-CMC from binary blends of poly(isoprene-*b*-styrene-*b*-2-vinylpyridine) (ISP) triblock terpolymers with different chain lengths of the two end-blocks. The tiling patterns vary depending  $\phi_P/\phi_I$ , which can be controlled by blend ratios of two ISP triblock terpolymers.

## 4.2 Experiments and Measurements

### 4.2.1 Molecular design

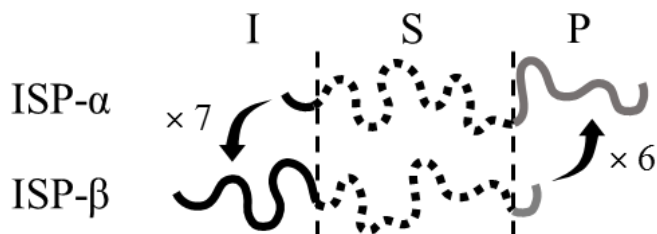


**Figure 4.1.** Schematic representation of the two ISP triblock terpolymers in this study. Black, dashed, and gray chains represent I, S, and P, respectively. The difference in molecular weight for I chains is about 7 and that for P chains is about 6.

Two kinds of ISP triblock terpolymer, ISP- $\alpha$  and ISP- $\beta$ , were synthesized via three-step anionic polymerizations as is mentioned in Chapter 2. SEC,  $^1\text{H-NMR}$ , MALLS and Osmometry were performed for the characterization. The schematic illustration of the two ISP triblocks are shown in Figure 4.1, in which black, dashed, and gray chains represent I, S, and P, respectively. Table 4.1 summarizes the molecular characteristics of the two parent triblocks. These ISP triblocks have almost the similar total molecular weights, but differ in the molecular weights of the I and P end-blocks. In fact, ISP- $\alpha$  and ISP- $\beta$  correspond to ISP-VI and ISP-V, respectively, used in Chapter 3, that is, the phase behavior of ISP-VI/ISP-V blend with varying the blend ratios was investigated in this chapter. In previous chapter, the equimolar blend of ISP-VI/ISP-V exhibited tetragonal-packed rod domains.

**Table 4.1.** Molecular Characteristics of Parent ISP Triblock Terpolymers Used in This Study.

Sample Name	$M_n^a$ ( $\times 10^3$ )	$\varphi_I^b$	$\varphi_S^b$	$\varphi_P^b$	$M_w/M_n^c$
 ISP- $\alpha$	122	0.06	0.62	0.32	1.02
 ISP- $\beta$	124	0.39	0.56	0.05	1.06

<sup>a</sup> Determined by osmometry. <sup>b</sup> Determined by <sup>1</sup>H-NMR spectroscopy and the densities of I, S and P at room temperature ( $\rho_I$ : 0.926,  $\rho_S$ : 1.05,  $\rho_P$ : 1.14 g/cm<sup>3</sup>). <sup>c</sup> Estimated from a SEC chromatogram whose elution volumes were calibrated with polystyrene standards.

**\*ISP- $\alpha$  and ISP- $\beta$  used in this chapter correspond to ISP70 and ISP61, respectively, in Table 2.1\***

Blend samples with various compositions were identified as Blend(A/B) as listed in Table 4.2, where A is the molar percentage of ISP- $\alpha$  and B is that of ISP- $\beta$ . The fundamental feature of these blend samples is that all the blend samples have a nearly constant  $\varphi_S$  and that  $\varphi_P/\varphi_I$  are gradually varied depending on the blend ratios. As identified above,  $\varphi_P/\varphi_I$  is an indicator of packing manner of cylindrical domains.<sup>26</sup> Furthermore, the ratio of the number of shorter P chains and longer P chains ( $N_{\text{short}}/N_{\text{long}}$ ) can be considered as an index of conformational entropy within P domains.

**Table 4.2.** Blend Manners of Two Parent Triblock Terpolymers and Volume Fractions of the Blend Samples.

Sample Name	Volume fraction	$\varphi_P/\varphi_I$	$N_{\text{short}}/N_{\text{Long}}(P)$
Blend(90/10)	0.09:0.62:0.29	3.02	0.11
Blend(80/20)	0.13:0.61:0.26	1.99	0.25
Blend(70/30)	0.16:0.60:0.23	1.41	0.43
Blend(60/40)	0.20:0.60:0.20	1.03	0.67
Blend(50/50)	0.23:0.59:0.18	0.77	1.00
Blend(40/60)	0.27:0.58:0.15	0.57	1.50
Blend(30/70)	0.30:0.58:0.12	0.42	2.33
Blend(20/80)	0.33:0.57:0.10	0.30	4.00
Blend(10/90)	0.36:0.57:0.07	0.21	9.00

#### 4.2.2 Preparation for blend samples

Blend samples were prepared according to the rule shown in Table 4.2. The samples were obtained by solvent casting from 5 wt% THF solution in Teflon beakers over 2 weeks at room temperature. Subsequently, the films were thoroughly dried under vacuum at room temperature and were treated with thermal annealing at 150 °C for 5 days. Detailed condition and procedure of the film preparation is mentioned in Chapter 2.

Note that the casting time (over 2 weeks) and annealing time (150 °C for 5 days) differ in those performed in Chapter 3. I have found the casting time and annealing time dependences on the resulting morphology especially of triblock terpolymer blends. It would require many pages to show and discuss the data, so let me mention summarily.

The casting time dependence (3days, 5days, 1 week and 2 weeks) was examined

## Chapter 4

under fixed conditions: 5 wt% THF solution, annealed at 150 °C for 5 days for Blend(48/52) by using SAXS and TEM. The samples performed at short casting time (3days, 5days, 1 week) generated different morphologies of each sample, and furthermore the thermal annealing changed the morphologies. It seems reasonable to conclude that the casting times: 3days, 5days and 1 week, are not long enough to achieve a state of thermodynamic equilibrium for the binary blend system. I found 2 weeks casting attained the thermal equilibrium morphology, that is, cylindrical morphology with a 5-coordinated domain orientation for Blend(48/52) as shown in Figure 4.7. Even after the thermal treatment, the morphology was maintained and became a highly-ordered array (larger grain size), but with slight shrinkage of domain distance. The shrink might be due to the cross-linkage of isoprene molecules. Actually, GPC confirmed that a small peak appeared toward lower elution after the thermal treatment.

I also examined the annealing time dependence (1day, 3days, 5 days, 1 week) under given conditions; 5 wt% THF solution, annealed at 150 °C, casting for 2 weeks for Blend(48/52) by using SAXS and TEM. For the SAXS patterns, higher periodic structures were obtained as increasing the annealing time, maintaining the morphology. The SAXS patterns for 5 days- and 1 week-annealed samples were overlapped considerably although the fraction of cross-linkage for 1 week-annealed samples was much higher. Hence, “casting over 2 weeks, thermal annealing at 150 °C for 5 days” is applied to a general procedure for preparing the blend samples.

### 4.2.3 Measurements

TEM experiments were performed with JEM-1400 of JEOL Ltd. operated at an accelerating voltage of 120 kV in the bright field mode. The annealed bulk films were cut into several small species and their small ones were embedded in an epoxy resin and cured for 9 hours at 60°C. Some species were treated with bulk staining in OsO<sub>4</sub> at 70°C for 2 hours before embedding to obtain strong contrast. The embedded samples were microtomed to a thickness of about 50 nm at room temperature. The ultrathin sections were collected on copper grids and then they were stained with OsO<sub>4</sub> for 2 hours at 70°C and/or I<sub>2</sub> for 2 hours at 50°C. Detail of the staining apparatus and condition is shown in Chapter 2. OsO<sub>4</sub> gives a strong contrast for the I component, and I<sub>2</sub> selectively stains the P component. By twostep staining with both the reagents, the I component obtains the strongest contrast and the P component earns the mid contrast; that is, dark, white, and gray contrasts represent I, S, and P phases, respectively.

In this chapter, I applied the dual-axis tomography to investigate three-dimensional microdomain structures. Transmission electron microscopy tomography (TEMT) experiment was carried out using a JEM-1400 of JEOL Ltd., being operated at an acceleration voltage of 120 kV. The annealed bulk films were immersed and stained with OsO<sub>4</sub> 5 wt% aqueous for 2 hours at 70°C before embedding. The ultrathin sections having about 200 nm thickness were prepared using an ultramicrotomed. The thin sections on a Cu grid were stained with OsO<sub>4</sub> for an hour at 70°C again. The both sides of the grid was coated with carbon using a vacuum deposition equipment (SVC-700, SANYU Electron. Co., Ltd.). Two sets of tilt TEM images were collected with tilt angles ranging from -50° to +50° in 1° increment using a specimen rotating holder. The series of TEM images were aligned by the fiducial marker method using the Au nanoparticles (10 nm) as a marker. The three dimensional reconstruction image was given by using a reconstruction software, Composer, and a visualization and modeling software, Visualizer, both of JEOL System Technology Co., Ltd.

## Chapter 4

SAXS experiments were conducted using beamline 6A and 10C at Photon Factory (Tsukuba, Japan). Two dimensional SAXS patterns were recorded on an automated imaging plate detector (R-Axis IV++, pixel size = 100  $\mu\text{m}$ ) and Pilatus 1M detector (pixel size = 172  $\mu\text{m}$ ). The instrument was calibrated using a silver behenate powder as a standard. The wavelength of the X-ray and the sample-to-detector distance at Photon Factory were 0.1508 nm ( $\text{CuK}\alpha$ ) and ca. 2000 mm, respectively. All SAXS experiments were performed for small sample pieces cut from the annealed bulk films, where X-ray was irradiated from the direction parallel to film surface.

Microbeam SAXS ( $\mu$ -SAXS) experiments were performed at high flux beamline BL40XU at SPring-8 (Hyogo, Japan). The wavelength of X-ray was 0.1 nm, and the size of the X-ray microbeam was ca. 5  $\mu\text{m}$   $\times$  5  $\mu\text{m}$  (fwhm). The camera length was fixed about 3 m, and the precise camera length was calibrated with a collagen standard sample. For  $\mu$ -SAXS measurements, the annealed bulk films were cut into thin section of about 5~10  $\mu\text{m}$  thickness by using an ultramicrotome. The thin films were collected on a Cu grid with 4 slits (2mm width with each slit). The grids were placed at the sample stage and X-ray was irradiated from the direction perpendicular to film surface. The scattering patterns were recorded with a CCD detector.

### 4.3 Results and Discussion

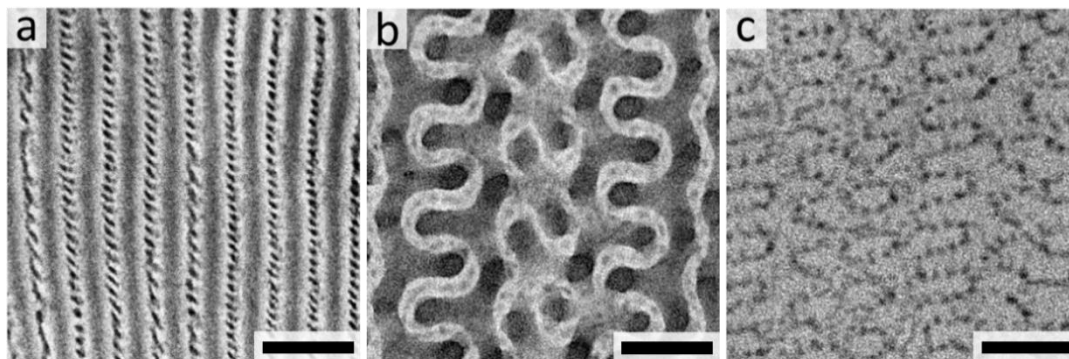


**Figure 4.2.** TEM images of the two parent triblock terpolymers. a) ISP- $\alpha$  and b) ISP- $\beta$  were stained with OsO<sub>4</sub>/I<sub>2</sub>. c) ISP- $\beta$  was stained with I<sub>2</sub> only. Scale bars all represent 100 nm.

Figure 4.2 compares the morphologies of the two parent terpolymers. For the TEM images of (a) and (b) stained with OsO<sub>4</sub> and I<sub>2</sub>, the black, white, and gray domains represent I, S and P phases respectively. In Figure 4.2 (c) of I<sub>2</sub>-stained ISP- $\beta$ , only P component can be observed. The ISP- $\alpha$  is a cylinder-in-lamellae structure, in which the minor component I remains in isolated cylinders at the center of S lamellae, as is shown in Figure 3.2. However, the ISP- $\beta$  exhibited a different structure from that of ISP-V shown in Chapter 3 by changing the film preparation process. In fact, ISP- $\beta$  and ISP-V are completely the same. As mentioned in the film preparation section, the bulk film of ISP- $\beta$  was prepared via 2-weeks solvent casting and thermal annealing at 150°C for 5 days, while ISP-V in Chapter 3 was conducted with 3-days solvent casting and thermal annealing at 150°C for 4 days. The morphology of ISP- $\beta$  shown in Figure 4.2 (b) was obtained with satisfactory reproducibility although that of ISP-V was not replicable under the given condition mentioned in Chapter 3. Naturally, these results suggest that Figure 4.2 (b) represent the thermal equilibrium structure of ISP- $\beta$ . Figure 4.2 (b) corresponds well to the [112] projection of a double gyroid structure. Although the double gyroid structure is composed of three components from ISP triblock terpolymers, the ordered

“bicontinuous” double gyroid is developed, in which I component forms two gyroid networks embedded in an S matrix. Combining Figure 4.2 (b) with Figure 4.2 (c) confirms P spherical domains lie on the S matrix. Considering the geometry of a double gyroid structure, the P spheres could be aligned on the gyroid triply periodic minimal surface.<sup>28</sup> To my knowledge, the sphere-in-gyroid structure has not yet been found experimentally, however, the structure might be reasonable considering the volume fractions and the geometrical constraint. Concerning ISP triblock terpolymers, there is no I/P interface because of the “nonfrustrated” system ( $\chi_{I-P} \gg \chi_{S-P} \cong \chi_{S-I}$ ). For ISP- $\beta$ , the geometrical (enthalpy) constraint causes the minor P component to be included in the S component, that is, the ISP- $\beta$  can be regarded as an IS diblock copolymer with  $\phi_I:\phi_{S(+P)}=0.39:0.61$ . Hasegawa et al. obtained an ordered bicontinuous double gyroid structure from IS diblock copolymers with  $\phi_S=0.62\sim 0.66$ ,<sup>29</sup> which sufficiently supports my experiments. Let me here focus on the S/P components in ISP- $\beta$ . The volume fraction of the two components in ISP- $\beta$  is  $\phi_S:\phi_P=0.92:0.08$ . According to Matsushita’s work<sup>30</sup>, an SP diblock copolymer with the volume fraction ( $\phi_S:\phi_P=0.92:0.08$ ) forms a spherical structure. These results corroborate that ISP- $\beta$  generates a sphere-in-gyroid structure.

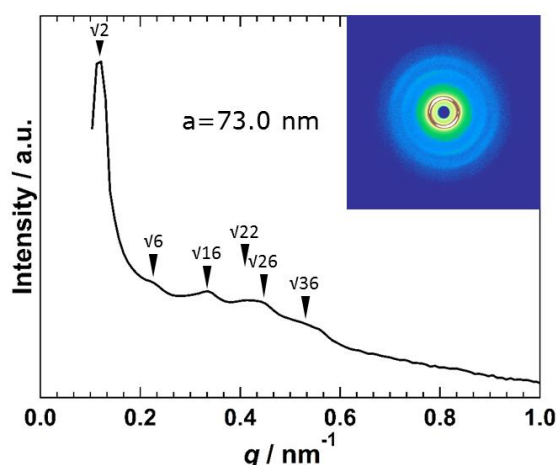


**Figure 4.3.** Azimuthally integrated SAXS patterns of ISP- $\beta$ . The inset represent the corresponding 2D SAXS pattern. “ $a$ ” expresses unit cell size [nm]. The inverted triangles point

out the sequence of peaks.

Figure 4.3 displays the SAXS pattern of ISP- $\beta$ . The pattern exhibit peaks at relative  $q$  values  $\sqrt{2}:\sqrt{6}:\sqrt{16}:\sqrt{22}:\sqrt{26}:\sqrt{36}$ , which confirms the formation of a double gyroid phase. Although P component has the highest electron density of the three component, the volume fraction is too small to detect the interference, suggesting that the domain distance between P spheres aligning over the gyroid surface cannot be identified. I shall spare the SAXS pattern of ISP- $\alpha$  because the pattern corresponds well with that of ISP-VI even though the bulk films were prepare via different ways.

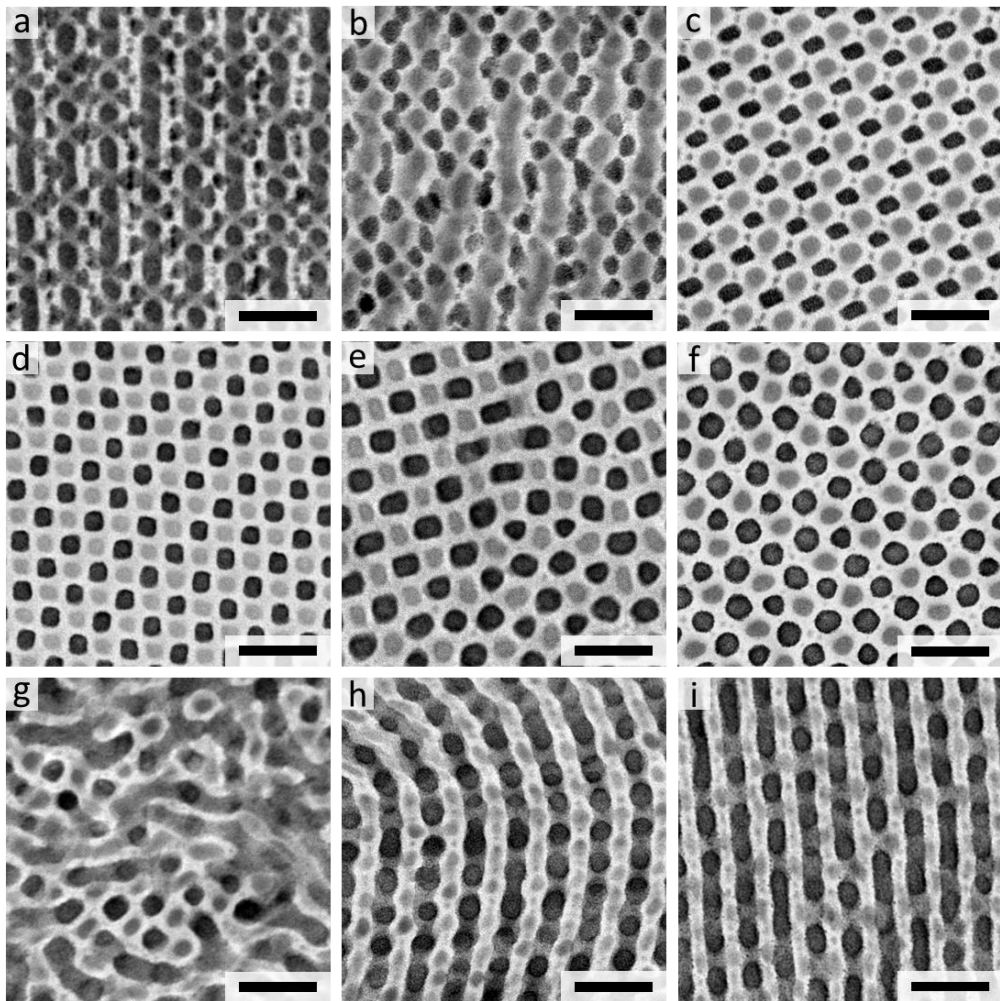


**Figure 4.4.** TEM images of the blend samples. (a) Blend(90/10), (b) Blend(80/20), (c)

## Chapter 4

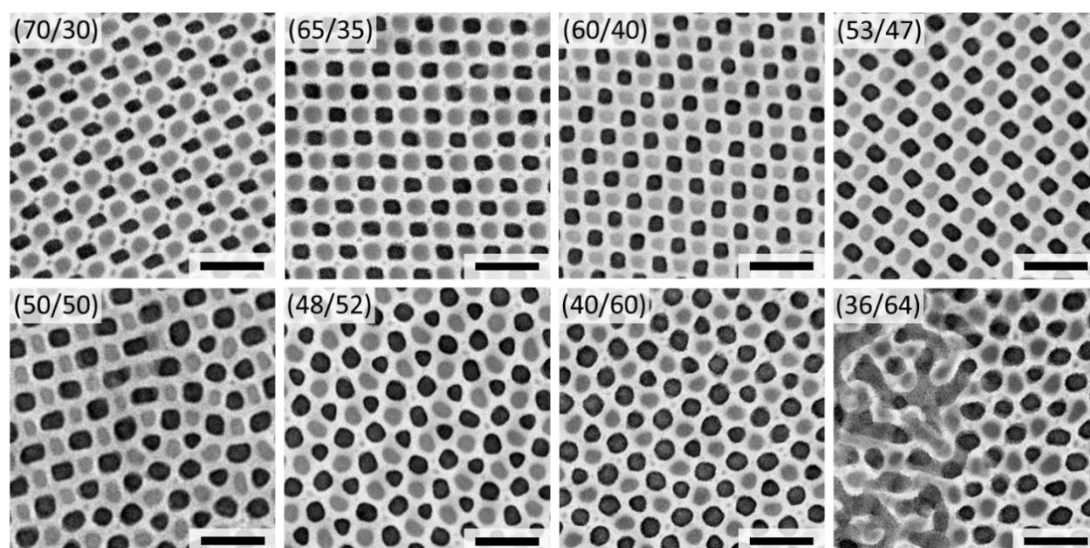
Blend(70/30), (d) Blend(60/40), (e) Blend(50/50), (f) Blend(40/60), (g) Blend(30/70), (h) Blend(20/80) and (i) Blend(10/90). All samples were stained with  $\text{OsO}_4/\text{I}_2$ . Scale bars all represent 100 nm.

Figure 4.4 compares the TEM micrographs of self-assembled structures for the blend samples. All these morphologies could not be obtained in neat ISP triblock terpolymers with the same compositions of each sample. For example, an ISP triblock terpolymer with  $\phi_{\text{I}}:\phi_{\text{S}}:\phi_{\text{P}}=0.20:0.60:0.20$  that is the same volume fractions with that of Blend(60/40), shows a double gyroid structure.<sup>9</sup> Interestingly, all the blend samples do not exhibit macrophase separation in spite of the large chain length differences of two end blocks. It is apparent that Blend(90/10), Blend(80/20) and Blend(30/70) do not exhibit periodic structures although the each component generates isolated domains. Perforated lamella-like structures were obtained in Blend(20/80) and Blend(10/90). This chapter is focusing on cylindrical morphology, so the fuller study of the specific structures from Blend(90/10), Blend(80/20), and Blend(30/70)~(10/90) lie outside the scope of this work. Cylindrical morphologies were obtained from Blend(70/30) to Blend(40/60), TEM images of which show the cross section of the cylindrical domains. Interestingly, the cylindrical structures show different domain orientations for each sample. Here, let me examine further the cylindrical structures by finely tuning the volume fractions. The additional blend samples are summarized in Table 4.3 and the sample were prepared in the same way as mentioned in Section 4.2.2.

**Table 4.3.** Molecular Characteristics of Blend Samples Exhibiting Cylindrical Structures.

Sample Name	Volume fraction	$\phi_P/\phi_I$	$N_{\text{short}}/N_{\text{Long}}$
Blend(70/30)	0.16:0.60:0.23	1.41	0.43
Blend(65/35)	0.18:0.60:0.22	1.20	0.54
Blend(60/40)	0.20:0.60:0.20	1.03	0.67
Blend(53/47)	0.23:0.59:0.18	0.84	0.89
Blend(50/50)	0.23:0.59:0.18	0.77	1.00
Blend(48/52)	0.24:0.59:0.17	0.72	1.08
Blend(40/60)	0.27:0.58:0.15	0.57	1.50
Blend(36/64)	0.28:0.58:0.14	0.51	1.78

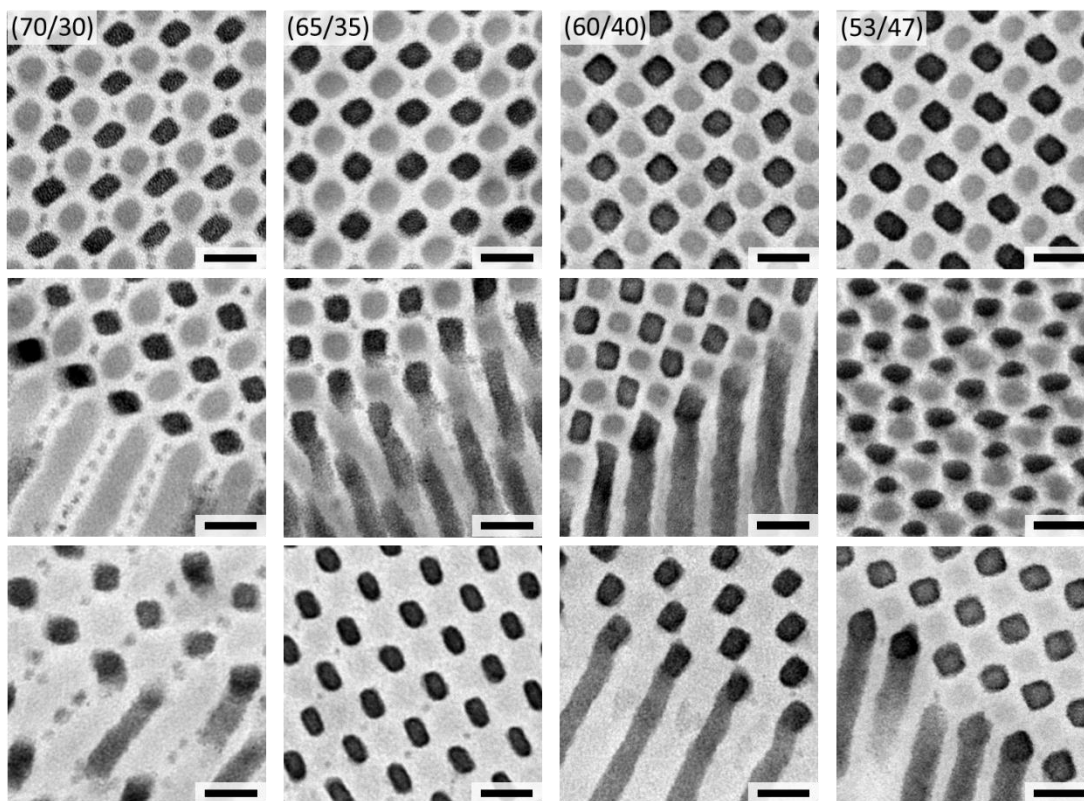
The additional samples are indicated in red.



**Figure 4.5.** Comparison of microphase-separated structures for the blend samples, all of which exhibit cylindrical morphologies. Insets express the blend ratios. All TEM images represent the cross section of cylindrical structures. Scale bars all represent 100 nm.

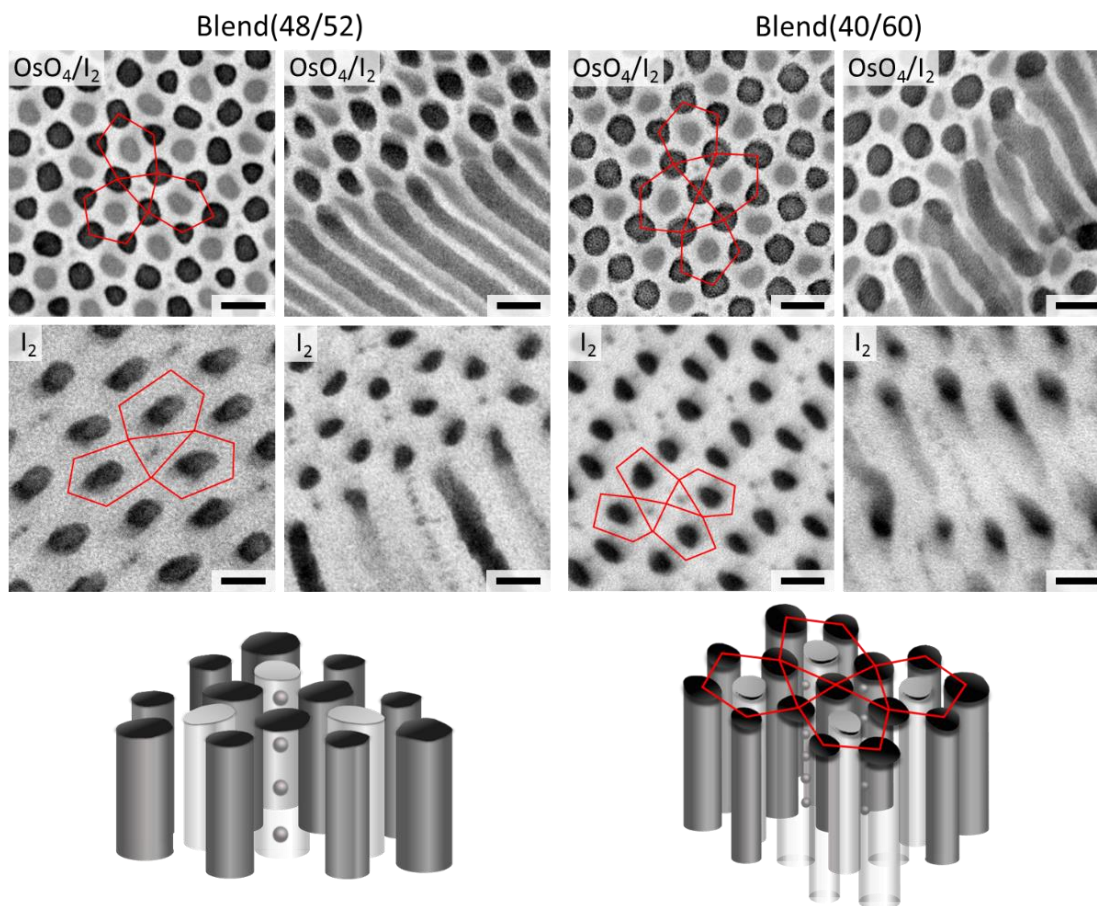
## Chapter 4

Figure 4.5 compares the TEM images of the blend samples, exhibiting cylindrical structures. All the images show the cross section of the cylindrical structures. It is evident that the domain packings vary depending on the blend ratios ( $\phi_P/\phi_I$ ). Above 4 images clearly reveal tetragonal-packed domain orientations, while below 4 images represent different domain orientations. Actually, at Blend(50/50) which is the same blend sample of ISP-V/ISP-VI in Chapter 3, two types of cylindrical structures are observed simultaneously, suggesting this sample is in a transit region between Blend(60/40) and Blend(48/52). Furthermore, cocontinuous structure is partially developed in Blend(36/64). Both Blend(48/52) and Blend(40/60) show new cylindrical structures. Later I shall try to give a more precise account of the new structures. For the present, it may be useful to look more closely at some of the important features of tetragonal-packed cylinders formed from Blend(70/30) to Blend(53/47).



**Figure 4.6.** Comparison of microphase-separated structures for the blend samples, all of which exhibit tetragonal-packed cylindrical structures. Insets express the blend ratios. The top two images of each sample represent OsO<sub>4</sub>/I<sub>2</sub>-stained images, Bottom images are the ones of the OsO<sub>4</sub>-stained specimen. Scale bars all represent 50 nm.

Figure 4.6 shows the summary of TEM images of the blend samples with a tetragonal manner. The top two images are the ones of the OsO<sub>4</sub>/I<sub>2</sub>-stained specimen and the bottom ones are presenting I domains stained with OsO<sub>4</sub>. The top images of each blend sample reveal that the shape of the cross section of I cylinders is close to square and furthermore small domains are observed between I cylinders and P cylinders for Blend(70/30) and Blend(65/35). (“Rectangular-shaped cylinder” is, properly speaking, “rod”, however in this thesis, the square-cylinder is called “cylinder” as is conventionally done.) The bottom TEM images for Blend(70/30) and Blend(65/35) confirmed that I phase generates two types of domains; sphere and cylinder. The middle TEM images show I spheres aligning along I cylinders with tetragonal symmetry. Note that the number of small I spheres increases gradually with the increase of fraction of ISP- $\alpha$ . Comparing TEM images of Blend(70/30) and that of ISP- $\alpha$ , we can notice that the size of the I spheres in Blend(70/30) is similar to that of I spheres in ISP- $\alpha$ , suggesting that the I spheres in Blend(70/30) and (65/35) are formed from the short I chain of ISP- $\alpha$ . Interestingly, the I spheres are distributed anisotropically and localized in a certain direction. The rectangular cylinders must affect the anomalous domain orientation, but at present I am incompetent to discuss that. There is one further feature that we must not ignore. For Blend(53/47), the specific domain orientation shown in the middle TEM image is observed in a small area and the domain orientation corresponds to that observed in Blend(48/52).



**Figure 4.7.** TEM images of Blend(48/52) and Blend(40/60) with various staining conditions. The staining reagents used are expressed in insets of each figure. Scale bars all represent 50 nm. Schematic illustrations drawn based on the TEM results.

Figure 4.7 compares Blend(48/52) with Blend(40/60). The cylindrical morphologies of both the blend samples show characteristic domain shapes and domain packings. The cross sections of the cylindrical domains are not simple circles, but rather anisotropic circles. That is, these blend samples also create an interface with non-CMC. Furthermore, it is apparent that I phase has variously sized domains and the domains arrange periodically. On the other hand, it can be confirmed that the small P domains appear at the center surrounding from three large I domains. In order to verify the arrangement of P domains, I<sub>2</sub>-stained sample films were prepared to give strong contrast to only P phase. Surprisingly, two kinds of P domains were

found; one is a cylindrical domain, and the other is a spherical one aligning periodically along the cylindrical I domains. Briefly, I have found complex morphologies based on the cylindrical structure that has domains with different sizes and shapes both in two end-block components. The structure from Blend(40/60) has some features similar to that of Blend(48/52): (1) cylinder-based morphology, (2) the cross sections of cylinders are not simple circle, (3) different sized I domains, (4) P components have two kinds of domain; cylinder and sphere.

However, the domain periodicities from the two blend samples are significantly different. The periodicities have been determined using a net (red solid line) that connects the nearest I domains together, as shown in Figure 4.7. Note that nets from Blend(48/52) and Blend(40/60) indicate that the tiling patterns are composed of triangles and pentagons and that those polygons regularly line up. The tiling from Blend(48/52) is almost the same as Izumi's report.<sup>26</sup> According to this tiling pattern, it can be confirmed that small P domains exist at the center of triangles. However, there is a significant difference between the tiling patterns of Blend(48/52) and Blend(40/60). The unit of polygons of Blend(48/52) includes a triangle and three pentagons, while that of Blend(40/60) consists of two triangles and four pentagons.

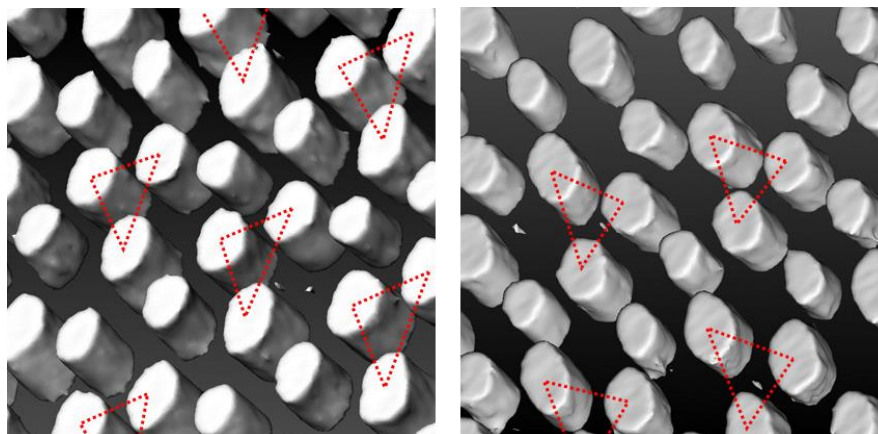


**Figure 4.8.** TEM tomography images of Blend(48/52). The highlighted phase represents I phase. Red lines are denoted for easier viewing.

Tomography images of Blend(48/52) are shown in Figure 4.8. These images were obtained by dual-axis tomography. Figure 4.7 reveals that small P domains align periodically along I cylinders and that the small domains are surrounded by I large cylinders. Hence, there is a high possibility that the surface of I large cylinders are undulated to possess the volume filled with the P spheres. Here look at the center of red triangles. It cannot be observed that the cylindrical domains possess the undulated surface.

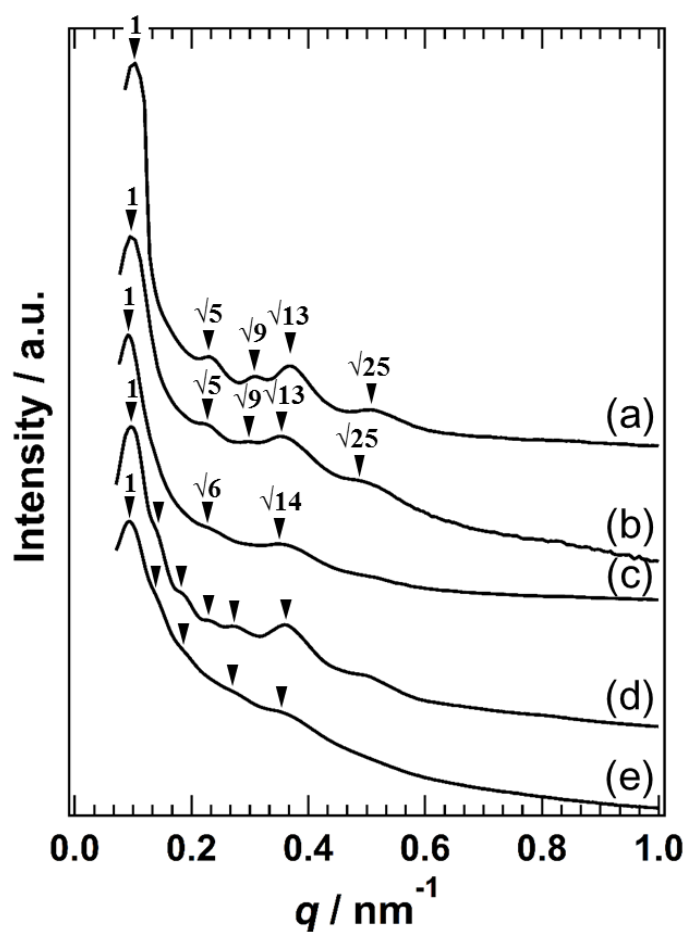


**Figure 4.8** Azimuthally SAXS patterns of blend samples. (a) Blend(60/40), (b) Blend(53/47), (c) Blend(50/50), (d) Blend(48/52), (e) Blend(40/60). Peaks are denoted by inverted triangles.

The domain periodicity of cylindrical structures were studied by SAXS. Selected

results drawn from blend samples (Blend(60/40)~Blend(40/60)) are shown in Figure 4.8. The scattering patterns obtained from Blend(60/40) and Blend(53/47), both of which exhibit tetragonal-packed cylinders, indicate representative relative  $q$  values of tetragonal cylinders; 1,  $\sqrt{5}$ ,  $\sqrt{9}$ ,  $\sqrt{13}$  and  $\sqrt{25}$ . The domain distances evaluated from the primary peak are in good accordance with the real space images. For Blend(50/50), in which two types of structures were observed in the TEM image, the SAXS pattern cannot identify the structure because of the small grain. On the other hand, the scattering patterns of Blend(48/52) and Blend(40/60) show many distinct peaks, but their peaks cannot be identified as traditional morphology. Hence,  $\mu$ -SAXS was performed to study the specific morphologies.

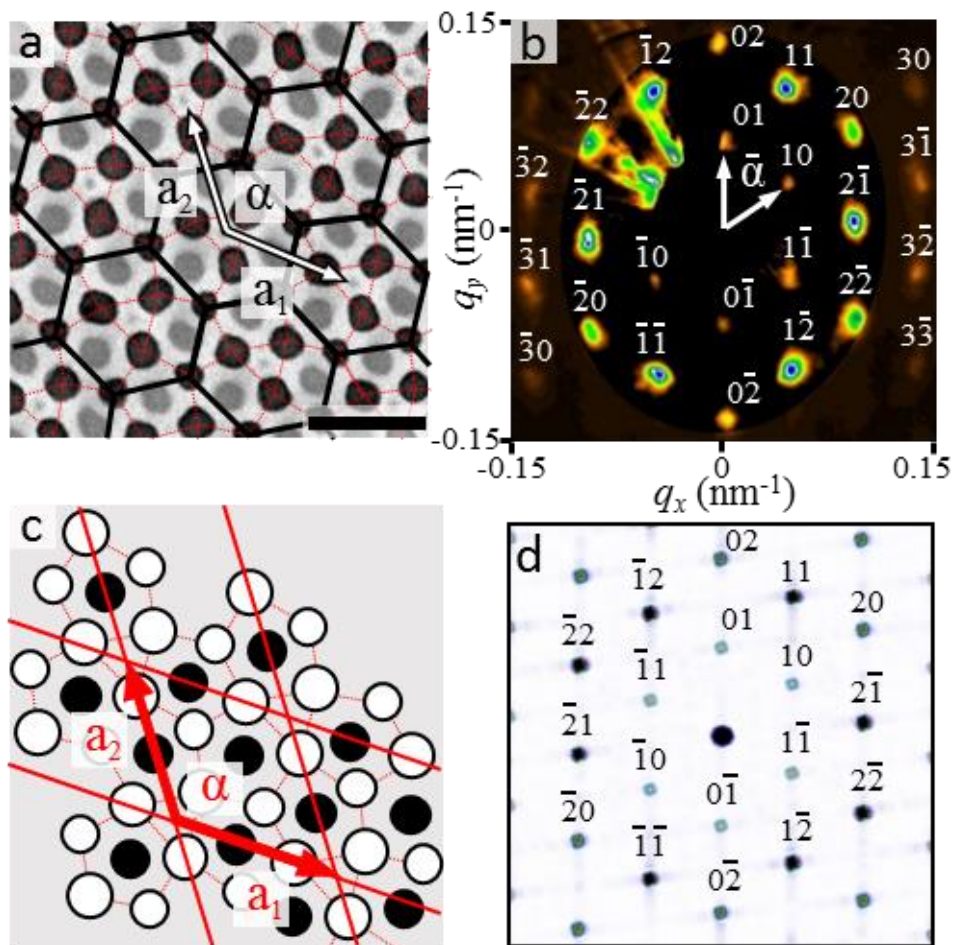


**Figure 4.9.** (a) Unit lattice data of Blend(48/52), denoted with black solid line, is

superimposed on the TEM image. The lattice size ( $a_1 \times a_2$ ) is estimated from  $\mu$ -SAXS. Scale bar represents 100 nm. (b)  $\mu$ -SAXS pattern. (c) Schematic illustration of domain orientation based on (a). White and black circles express I and P domains, respectively, considering their electron densities. (d) A FT pattern computed with the domain packing in (c). The size of the dots represents the intensities.

Unit lattice data expressed on the TEM image and the  $\mu$ -SAXS pattern of Blend(48/52) are presented in Figures 4.9 (a) and (b), respectively. In Figure 4.9 (a), white arrows express the real lattice vectors,  $a_1$  and  $a_2$ . Figure 4.9 (b) clearly indicates a hexagonal manner, in which first-order scattering vectors are denoted with white arrows. Spot-like 2D pattern is detected in the  $\mu$ -SAXS pattern, suggesting that the beam diameter (ca.  $5\mu\text{m}$ ) of the irradiated X-ray is small enough to probe the grains where the specific cylindrical structure orders with regularity. The lattice constants,  $a_1$  and  $a_2$ , were 120 and 133 nm calculated from the  $q$  values of their corresponding scattering vectors  $q_{10}$  and  $q_{01}$ , respectively. The angle  $\bar{\alpha}$  between  $q_{10}$  and  $q_{01}$  is  $55^\circ$ , which is reasonably consistent with the real lattice data, i.e.,  $\alpha = 127^\circ$ . These results concluded that the cylindrical structure of Blend(48/52) with a tiling pattern consisting of triangles and pentagons, exhibits crystallographically a hexagonal symmetry. For clarity, the hexagonal unit lattices of Blend(48/52) are displayed in Figure 4.9 (a), where the black solid polygons express the real-space lattices, which agree well with the reciprocal-space result obtained by the  $\mu$ -SAXS experiment.

Figure 4.9 (c) shows a more simplified schematic representation based on the real-space image of Blend(48/52), associated with electron density of each component (I: 0.512; S: 0.565; P: 0.608 electron/cm<sup>3</sup>). A Fourier Transform (FT) was performed for the illustration in Figure 4.9 (c), and Figure 4.9 (d) shows the resulting 2D pattern. The FT result reveals that the second ordered diffractions ( $02$ ,  $20$ ,  $2\bar{2}$ , etc.) are detected stronger than the first ordered

peaks (01, 10,  $1\bar{1}$ , etc.), and its nature is consistent with the experimental pattern.

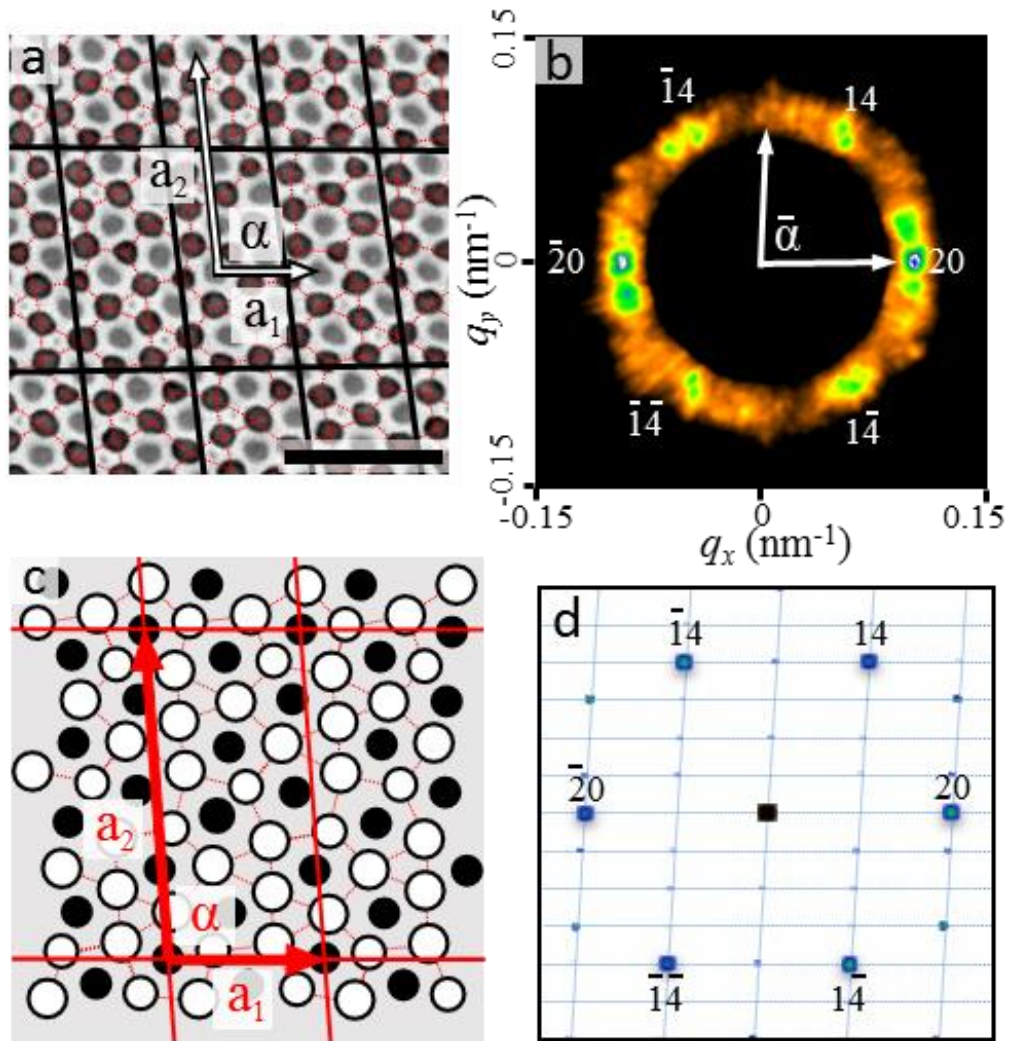


**Figure 4.10.** (a) Unit lattice data of Blend(40/60), denoted with black solid line, is superimposed on the TEM image. The lattice size ( $a_1 \times a_2$ ) is estimated from  $\mu$ -SAXS. Scale bar represents 100 nm. (b)  $\mu$ -SAXS pattern. (c) Schematic illustration of domain orientation based on (a). White and black circles express I and P domains, respectively, considering their electron densities. (d) A FT pattern computed with the domain packing in (c). The size of the dots represents the intensities.

Unit lattice data on the TEM image and the  $\mu$ -SAXS pattern of Blend(40/60) are presented in Figures 4.10 (a) and (b), respectively. Here one notices the diffraction spots in

Figure 4.10 (b) are similar to that of a hexagonal symmetry, although a hexagonal-packed morphology cannot be found. Provided that the representative diffractions indicate (14), (20), etc., as shown in Figure 4.10 (b), the pattern gives an oblong-type unit lattice whose lattice constants are 135nm, 295 nm, and  $88^\circ$  for  $a_1$ ,  $a_2$ , and  $\bar{\alpha}$ , respectively. These values agree reasonably well with the real space data, i.e., 131 nm, 279 nm, and  $95^\circ(\alpha)$ , respectively. The schematic illustration of domain packing considering electron densities is described in Figure 4.10 (c) and the resulting FT pattern is shown in Figure 4. 10 (d). The blue auxiliary lines linking the diffractions shown in Figure 4.10 (d) give an oblong-shaped unit lattice. We can find that the agreement between Figure 4.10 (b) and Figure 4. 10 (d) is satisfactorily good.

We evaluated the periodicity of the complex morphologies formed from Blend(48/52) and (40/60) by using X-ray analysis. Interestingly, the estimated unit lattice size tends to increase dramatically as  $\phi_p/\phi_I$  decreases.

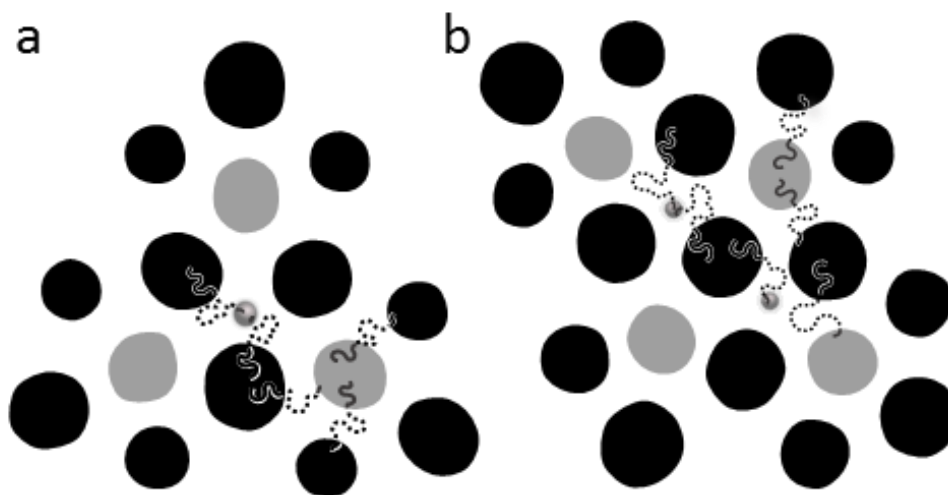


**Figure 4.11.** Schematic representations of possible chain orientation within the domain structures of (a) Blend(48/52) and (b) Blend(40/60). Black, dashed, and gray chains represent I, S, and P, respectively.

Following the rectangular cylinders, two additional characteristic morphologies were found in the ISP triblock terpolymer blends. There are two common features in the morphologies: (1) microdomains with nonconstant forms and sizes, (2) tiling patterns consisting of imaginary triangles and pentagons.

Let me first discuss the feature (1). The possible chain orientation in domain structure is schematically drawn in Figure 4.11, where the domain arrangements were transcribed from the real-space images. It is explained earlier that a structure with non-CMC is obtained by heterogeneous chain distribution within the domain. In the case of this work, block chains with different lengths are forced to share the same domain, and hence localize at the proper position of the domain boundary due to release the conformational entropy cost, resulting in the creation of non-CMC cylindrical structures. Furthermore, microdomains with different forms and sizes have also been developed in the unit lattices, as shown in Figure 4.9 and 4.10. In particular, P component creates two kinds of domains; sphere and cylinder. The shorter P chains of ISP- $\beta$  prefer to form spherical domains, as is the case with the original self-assembled structure of the ISP- $\beta$ . Furthermore, the size of the P sphere domains for Blend(48/52) and Blend(40/60) is about 4 nm, which is close to that of P spheres from the neat ISP- $\beta$  based on Figure 4.2 (c). However, it is unnatural that the longer P chains on ISP- $\alpha$  distribute in the P spherical domains, since the molecular weight of P block in ISP- $\alpha$  is 41 000 g/mol. Moreover, if assuming shorter P chains are all distributed in the spheres, the relative volume ratio of the two P domains does not match the volume fractions of P chains in Blend(48/52) and Blend(40/60). It is entirely fair to say that the spherical P domains observed in Blend(48/52) and Blend(40/60) were composed of only P chains of ISP- $\beta$  because the number of the shorter P chains is larger than that of the longer P chains. Alternatively,  $N_{\text{short}}/N_{\text{long}}$  is 0.67 in Blend(60/40), indicating that shorter chains can be miscible with an excess longer chains, resulting in a homogeneous domain. If  $N_{\text{short}}/N_{\text{long}}$  is excess over unity, i.e., 1.08 for

## Chapter 4

Blend(48/52) and 1.50 for Blend(40/60), conformational entropy cost within I and P domains is increased along with heightened  $N_{\text{short}}/N_{\text{long}}$ , but cannot be relieved merely by the chain localization within domains. Eventually, shorter P chains could be expelled from cylindrical P domains and generate the individual domains. As a result, the spherical structure is possibly stabilized by chain localization of shorter chains in a unit lattice. Based on the assumption of the possible chain distribution as depicted in Figure 4.11, it seems reasonable that I domains surrounding the spherical P domains become bigger. Moreover, the perspective of increased  $N_{\text{short}}/N_{\text{long}}$  corroborates that Blend(40/60) with lower  $N_{\text{short}}/N_{\text{long}}$  form the morphology with more spherical P domains.

Now, I shall discuss the feature (2). It has been confirmed that the packing state of cylindrical structure in ABC triblock terpolymers considerably depends on  $\phi_C/\phi_A$ . For neat ABC triblock terpolymers, a 5-coordination structure has never been found even if the  $\phi_C/\phi_A$  systematically changes. This is due to the thermodynamical and geometrical constraints. However, in this study, two complex structures having a 5-coordinated packing were found with decreasing  $\phi_P/\phi_I$ . These characteristic packing states are probably derived from the synergetic effect between the chain localization and the asymmetric interface curvature.

It should be noted that systematical increase of the unit lattice size has been confirmed by only varying the blending ratios without changing the parent polymers. The unit lattices have changed from square to hexagon, and furthermore from hexagon to oblong depending the blend ratios, and the oblong unit lattice is extremely large. This phenomenon is very similar to the one well-known in metal alloy system, where pseudo decagonal approximants have been observed<sup>31,32</sup> Hence, the oblong shape unit lattice could be considered as the pseudodecagonal phase. One can safely say that decagonal quasicrystal could be found in the vicinity of this study.

## 4.4 Conclusion

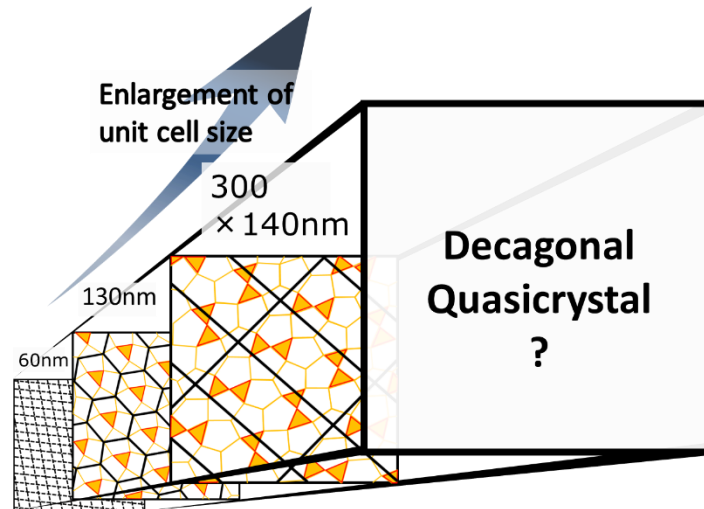


**Figure 4.12.** Summary of the present work. The enlargement of unit cell sizes by varying the blend ratios will develop a decagonal quasicrystal.

Two characteristic cylindrical morphologies were found in the binary blends of ISP triblock terpolymers. These two morphologies have two specific features: (1) domains with different forms and sizes, (2) tiling patterns composed of triangles and pentagons. The former feature probably stems from the weak localization of the junction point of the two parent ISP triblocks within domains and that excess amount of the shorter block chains form the individual domains to relieve the conformational entropy cost within the unit lattices. The latter one is derive from the synergistic effect of asymmetric interfacial curvature of I and P phases and the composition distribution. The cylindrical morphology with oblong unit lattices can be considered as a pseudodecagonal phase; hence, the present work provides a new approach with respect to the creation of new morphologies, which could be used to form decagonal quasicrystal structures.

## 4.5 References

1. Leibler, L. Theory of Microphase Separation in Block Copolymers. *Macromolecules* **1980**, 13, 1602-1617.
2. Matsen, M. W. Effect of Architecture on the Phase Behavior of AB-Type Block Copolymer Melts. *Macromolecules* **2012**, 45, 2161-2165.
3. Helfand, E.; Wasserman, Z. R. Block Copolymer Theory. 4. Narrow Interphase Approximation. *Macromolecules* **1976**, 9, 879-888.
4. Ohta, T.; Kawasaki, K. Equilibrium morphology of block copolymer melts. *Macromolecules* **1986**, 19, 2621-2632.
5. Matsen, M. W.; Schick, M. Stable and unstable phases of a diblock copolymer melt. *Phys Rev Lett* **1994**, 72, 2660-2663.
6. Matsuo, M.; Sagae, S.; Asai, H. Fine structures of styrene-butadiene block copolymer films cast from toluene solution. *Polymer* **1969**, 10, 79-87.
7. Inoue, T.; Soen, T.; Hashimoto, T.; Kawai, H. Thermodynamic interpretation of domain structure in solvent-cast films of A-B type. *J. Polym. Sci. Part A-2* **1969**, 7, 1283-1302.
8. Matsushita, Y.; Choshi, H.; Fujimoto, T.; Nagasawa, M. Preparation and Morphological Properties of a Triblock Copolymer of the ABC Type. *Macromolecules* **1980**, 13, 1053-1058.
9. Mogi, Y.; Kotsuji, H.; Kaneko, Y.; Mori, K.; Matsushita, Y.; Noda, I. Preparation and Morphology of Triblock Copolymers of the ABC Type. *Macromolecules* **1992**, 25, 5808-5411.
10. Choi, H.K.; Gwyther, J.; Manners, I.; Ross, C.A. Square Arrays of Holes and Dots Patterned from a Linear ABC Triblock Terpolymer. *ACS NANO* **2012**, 6, 8342-8348.
11. Breiner, U.; Krappe, U.; Abetz, V.; Stadler, R. Cylindrical morphologies in asymmetric ABC triblock copolymers. *Macromol. Chem. Phys.* **1997**, 198, 1051-1083.
12. Gido, S.P.; Schwark, D.W.; Thomas, E.L.; Goncalves, M.C. Observation of a Non-Constant Mean Curvature Interface in an ABC Triblock Copolymer. *Macromolecules* **1993**, 26, 2636-2640.
13. Auschra, C.; Stadler, R. New Ordered Morphologies in ABC Triblock Copolymers. *Macromolecules* **1993**, 26, 2171-2174.
14. Stadler, R.; Auschra, C.; Beckmann, J.; Krappe, U.; Voigt-Martin, I.; Leibler, L. Morphology and Thermodynamics of Symmetric Poly(A-block-B-block-C) Triblock Copolymers. *Macromolecules* **1995**, 28, 3080-3097.
15. Erhardt, R.; Boker, A.; Zettl, H.; Kaya, H.; Pyckhout-Hintzen, W.; Krausch, G.; Abetz, V.; Muller, A. H. E. Janus Micelles. *Macromolecules* **2001**, 34, 1069-1075.
16. Ott, H.; Abetz, V.; Altstadt, V. Morphological Studies of Poly(styrene)-block-poly(ethylene-co-butylene)-

## Chapter 4

- block-poly(methyl methacrylate) in the Composition Region of the “Knitting Pattern” Morphology. *Macromolecules* **2001**, 34, 2121-2128.
17. Higuchi, T.; Sugimori, H.; Jiang, X.; Hong, S.; Matsunaga, K.; Kaneko, T.; Abetz, V.; Takahara, A.; Jinnai, H. Morphological Control of Helical Structures of an ABC-Type Triblock Terpolymer by Distribution Control of a Blending Homopolymer in a Block Copolymer Microdomain. *Macromolecules* **2013**, 46, 6991-6997.
  18. Tang, C.; Lennon, E. M.; Fredrickson, G. H.; Kramer, E. J.; Hawker, C.J. Evolution of Block Copolymer Lithography to Highly Ordered Square Arrays. *Science* **2008**, 322, 429-432.
  19. Asari, T.; Matsuo, S.; Takano, A.; Matsushita, A. Three-Phase Hierarchical Structures from AB/CD Diblock Copolymer Blends with Complementary Hydrogen Bonding Interaction. *Macromolecules* **2005**, 38, 8811-8815.
  20. Matsushita, Y.; Suzuki, J.; Izumi, Y.; Matsuoka, K.; Takahashi, S.; Y. Aoyama,; Mihira, Y.; Takano, A. A New Periodic Pattern with Five-Neighbored Domain Packing from ABC Triblock Terpolymer B Homopolymer Blend. *J. Chem. Phys.* **2010**, 133, 194901.
  21. Asai, Y.; Yamada, K.; Yamada, M.; Takano, A.; Matsushita, Y. Formation of Tetragonally-Packed Rectangular Cylinders from ABC Block Terpolymers Blends. *ACS Macro Letters* **2014**, 3, 166-169.
  22. Hayashida, K.; Takano, A.; Arai, S.; Shinohara, Y.; Amemiya, Y.; Matsushita, Y. Archimedean Tiling Patterns of ABC Star-Shaped Terpolymers Studied by Microbeam Small-Angle X-ray Scattering. *Macromolecules* **2006**, 39, 9402-9408.
  23. Hayashida, K.; Dotera, T.; Takano, A.; Matsushita, Y. Polymeric Quasicrystal Mesoscopic Quasicrystalline Tiling in ABC Star Polymers. *Phys. Rev. Lett* **2007**, 98, 195502.
  24. Lee, S.; Bluemle, M. J.; Bates, F. K. Discovery of a Frank-Kasper  $\sigma$  Phase in Sphere-Forming Block Copolymer Melts. *Science* **2010**, 330, 349-353.
  25. Zhang, J.; Bates, F.S. Dodecagonal Quasicrystalline Morphology in a Poly(styrene-*b*-isoprene-*b*-styrene-*b*-ethylene oxide) Tetrablock Terpolymer. *J. Am. Chem. Soc.* **2012**, 134, 7636-7639.
  26. Izumi, Y.; Yamada, M.; Takano, A.; Matsushita, Y. A New Periodic Pattern with Five-Neighbored Domain Packing from ABC triblock Terpolymer/B Homopolymer Blend. *J. Polym. Sci., Part B: Polym. Phys.* **2015**, 53, 907-911.
  27. Abetz, V.; Goldacker, T. Formation of superlattices via blending of block copolymers. *Macromol. Rapid. Commun.* **2000**, 21, 16-34.
  28. Dotera, T.; Kimoto, M.; Matsuzawa, J. Hard spheres on the gyroid surface. *Interface Focus* **2012**, 2, 575-581.
  29. Hasegawa, H.; Tanaka, H.; Yamasaki, K.; Hashimoto, T. Bicontinuous Microdomain Morphology of Block Copolymers. 1. Tetrapod-Network Structure of Polystyrene-Polyisoprene Diblock Polymers. *Macromolecules* **1987**, 20, 1651-1662.

## Chapter 4

30. Matsushita, Y. Studies on Equilibrium Structures of Complex Polymers in Condensed Systems. *J. Polym. Sci., Part B: Polym. Phys.* **2000**, 38, 1645-1655.
31. Edagawa, K. Phonon–phason coupling in decagonal quasicrystals. *Philosophical Magazine* **2007**, 87, 2789-2798.
32. Hovmoller, S.; Zou, L. H.; Zou, X.; Grushko, B. Structures of pseudo-decagonal approximants in Al-Co-Ni. *Phil. Trans. R. Soc. A* **2012**, 370, 2949-2959.

## CHAPTER 5

# Asymmetric Double Tetragonal Domain Packing from ABC Triblock Terpolymer Blends with Chain Length Difference

\*Part of this work was published in “Yusuke Asai, Atsushi Takano, Yushu Matsushita *Macromolecules* **2016**, 49, 6940-6946.”

### 5.1 Introduction

Block copolymers consisting of two or more chemically distinct constituents spontaneously self-assemble into periodical microstructures in condensed state.<sup>1-3</sup> The ability of self-assembled structures to exhibit tunability of domain distance and thickness and a huge variety of morphologies has received much attention experimentally and theoretically.<sup>4-7</sup>

For the simplest block copolymer, AB diblock copolymer, four classical structures - alternative lamellae, bicontinuous double gyroid, hexagonally packed cylinders, and body-centered cubic spheres - are typically obtained.<sup>8-11</sup> The phase behavior of AB diblock copolymers is controlled by the relevant parameters; the degree of polymerization ( $N$ ), the Flory-Huggins interaction parameter ( $\chi_{AB}$ ), and the volume fraction of the A component ( $\phi_A$ ).

The addition of a third component to be ABC triblock terpolymers can provide a richer phase behavior because of increase in the number of parameters; interaction parameters ( $\chi_{AB}$ ,  $\chi_{AC}$ ,  $\chi_{BC}$ ), volume fractions ( $\phi_A$ ,  $\phi_B$ ,  $\phi_C$ ), and component sequences (ABC, ACB, BAC).<sup>2,3,12-22</sup> The bridging conformation of the middle B chains between the two end blocks also contributes to the variety and complexity of morphologies. For example, ABC triblock

## Chapter 5

terpolymers with interaction parameters  $\chi_{AB} \cong \chi_{BC} < \chi_{AC}$  produce three-phase four-layer lamellae, tricontinuous double gyroid, coarrayed tetragonal-packed cylinders, and spheres with a CsCl-type lattice depending on  $\phi_B$  when the end-block compositions are equal,  $\phi_A = \phi_C$ .<sup>3,12,13</sup> When A/C interactions are less expensive than A/B or B/C interactions ( $\chi_{AC} > \chi_{AB}$  or  $\chi_{BC}$ ), the triblocks prefer to produce structures with A/C interfaces, resulting in complex morphologies since those molecules must be in a frustrated circumstance. Breiner and Liu have reported that the frustrated systems create more complex morphologies than the nonfrustrated ones.<sup>17,22</sup>

Despite a lot of experimental and theoretical studies, a comprehensive understanding of the phase behavior of ABC triblock terpolymers is still lacking since the triangle phase diagram must be considered. Especially in experiments, a huge number of ABC triblock terpolymers are required to cover the entire phase diagrams. One of the efficient methods to accomplish above the difficulty is mixing of polymers, which can change the compositions of block copolymers without synthesizing new copolymers with different compositions. There are essentially two ways: one is blending ABC triblock terpolymers with the constituent homopolymer(s), and the other is blending ABC triblock terpolymers with block copolymers or terpolymers with two or three constituent blocks.

Blending the constituent homopolymers with ABC triblock terpolymers denotes a well-established technique to control morphology.<sup>23-26</sup> Note that triblock terpolymer/homopolymer blend systems are not strictly equivalent to neat triblock terpolymers with same compositions and have proven to stabilize new ordered morphologies such as *Fddd* orthorhombic network structure<sup>23</sup> and a cylindrical structure with a 5-neighbors domain packing.<sup>26</sup> Dotera theoretically reported that ABC/A/C blends produce tricontinuous double diamond and also double primitive structures.<sup>27</sup>

Blends of ABC triblock terpolymers and block copolymers have also become an

attractive research area.<sup>28–35</sup> In contrast to block terpolymer/homopolymer blend systems, where the spatial distribution of the homopolymers within chemically corresponding domains significantly affects the stable phase, the chemical junctions of the blended block copolymers have to share a common microdomain interface, resulting in the creation of characteristic structures such as noncentrosymmetric superlattice and core–shell superlattices.<sup>28–31</sup> In addition, a large number of controlling parameters (blend ratios, molecular weights, and volume fractions) in the blend system produce much richer phase diagrams than those of neat triblock terpolymers.

In our previous papers, fantastic morphologies have been found in poly(*isoprene-block-styrene-block-(2-vinylpyridine)*) (ISP) triblock terpolymer blends. They are periodic undulated lamellae,<sup>33</sup> rectangular-shaped rods,<sup>34</sup> and cylindrical morphologies with non-uniform domain forms and sizes.<sup>35</sup> Especially, for the binary blend of ISP triblock terpolymers with different chain lengths of two end-blocks, the unit lattices of the cylindrical morphology show oblong shape extremely large than the size of individual domain, which was regarded as a pseudo decagonal approximant.<sup>35</sup>

Our purpose of this work is to investigate the morphological behavior of the binary blends of ISP triblock terpolymers with asymmetric different chain lengths of two end-blocks unlike our previous works employing symmetric different chain lengths.<sup>35</sup> Concretely, the difference in molecular weights for I chains is 4 and that for P chains is 8, while the total molecular weight of the two ISP triblock terpolymers and the molecular weights of central S component are constant. The morphologies of the binary blends were carefully investigated by using transmission electron microscopy (TEM) and small angle X-ray scattering (SAXS) measurements.

## 5.2 Experiments and Measurements

### 5.2.1 Molecular design

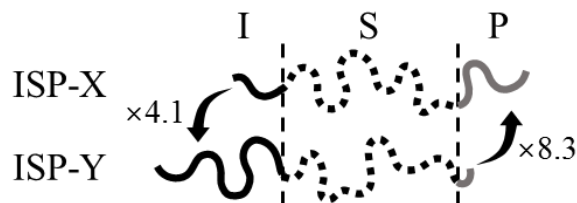


**Figure 5.1.** Simple sketch of the two parent ISP triblock terpolymers in this study. Black, dashed, and gray chains represent I, S, and P components, respectively.

Two kinds of poly(isoprene-*b*-styrene-*b*-2-vinylpyridine) (ISP) triblock terpolymers, ISP-X and ISP-Y, were synthesized via living anionic polymerization. The details of synthetic procedure are mentioned in Chapter 2. The schematic illustration of the two ISP triblocks are denoted in Figure 5.1, in which black, dashed, and gray chains represent I, S, and P, respectively. Table 5.1 summarizes the molecular characteristics of the two ISP triblock terpolymers prepared. ISP-X and ISP-Y correspond to ISP-80 and ISP-68, respectively, as shown in Chapter 2.

**Table 4.1.** Characteristics of Parent ISP Triblock Terpolymers Used in This Work.

Sample Name	$M_n^a$ ( $\times 10^3$ )	$\phi_I^b$	$\phi_S^b$	$\phi_P^b$	$M_w/M_n^c$
ISP-X	223	0.12	0.67	0.21	1.02
ISP-Y	264	0.42	0.56	0.02	1.03

<sup>a</sup> Determined by osmometry. <sup>b</sup> Determined by <sup>1</sup>H-NMR spectroscopy and the densities of I, S and P at room temperature ( $\rho_I$ : 0.926,  $\rho_S$ : 1.05,  $\rho_P$ : 1.14 g/cm<sup>3</sup>). <sup>c</sup> Estimated from a SEC chromatogram whose elution volumes were calibrated with polystyrene standards.

\*ISP-X and ISP-Y used in this chapter correspond to ISP80 and ISP68, respectively, in

**Table 2.1\***

The composition data of the binary blends of ISP-X and ISP-Y denoted as Blend(X/Y) are listed in Table 5.2, where X is the molar ratio of ISP-X and Y is that of ISP-Y. The composition ratio of two end components,  $\phi_P/\phi_I$ , is gradually varied as changing the blend ratios. The  $\phi_P/\phi_I$  is recognized as a good indicator to signify the degree of asymmetry.<sup>26</sup>

**Table 5.2.** Molecular Characteristics of Blend Samples in This Study.

Sample Name	Volume fraction	$\phi_P/\phi_I$
Blend(9/1)	0.16:0.66:0.18	1.13
Blend(8/2)	0.20:0.64:0.16	0.82
Blend(7/3)	0.23:0.63:0.14	0.62
Blend(6/4)	0.26:0.62:0.12	0.47
Blend(5/5)	0.29:0.61:0.10	0.36
Blend(4/6)	0.32:0.60:0.08	0.27
Blend(3/7)	0.34:0.59:0.07	0.23
Blend(2/8)	0.37:0.58:0.05	0.14
Blend(1/9)	0.40:0.57:0.03	0.09

### 5.2.2 Preparation for blend samples

All sample films for the morphological observation were prepared by solvent casting from 3 wt % solution in THF. The solvent was slowly vaporized over 2 weeks in a PTFE beaker at room temperature in a temperature-controlled oven. Subsequently, the films were dried under vacuum at room temperature for 1 day, followed by thermal annealing at 150 °C for 5 days. Detailed condition and procedure of the film preparation is explained in Chapter 2.

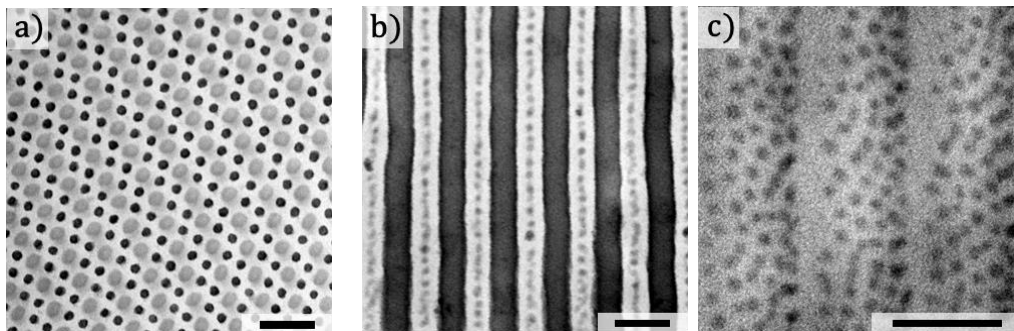
### 5.2.3 Measurements

TEM and SAXS analysis were performed to examine the morphologies of the blend samples. For TEM observation, the ultrathin sections prepared by a microtome were stained with osmium tetroxide ( $\text{OsO}_4$ ) vapor for 3 h at 70 °C and iodine ( $\text{I}_2$ ) vapor for 2 h at 50 °C.  $\text{OsO}_4$  gives a strong contrast for the I component, and  $\text{I}_2$  selectively stains the P component. Treating with both the staining reagents gives the strongest contrast for the I component and the mid contrast for the P component; that is, dark, white, and gray contrasts represent I, S, and P phases, respectively. TEM experiments were performed with a JEM-1400 (JEOL Ltd.) operated at an accelerating voltage of 120 kV.

SAXS experiments were conducted using BL 8S3 of Aichi Synchrotron Radiation Center (Aichi, Japan) and beamline 6A at Photon Factory (Tsukuba, Japan). The wavelength of the X-ray and the camera length at BL 8S3 were 0.15 nm and 3965 mm, respectively. The instrument was calibrated using lead stearate as a standard, and 2D SAXS patterns were collected on an automated imaging plate detector (R-AXIS IV++, pixel size = 100  $\mu\text{m}$ ). The wavelength of the X-ray and the camera length at beamline 6A were 0.15 nm and 2519 mm, respectively. A silver behenate powder was used for the calibration of the instrument, and 2D SAXS patterns were recorded on a Pilatus 1 M detector (pixel size = 172  $\mu\text{m}$ ). All SAXS

experiments were performed on small pieces cut from the annealed sample films.

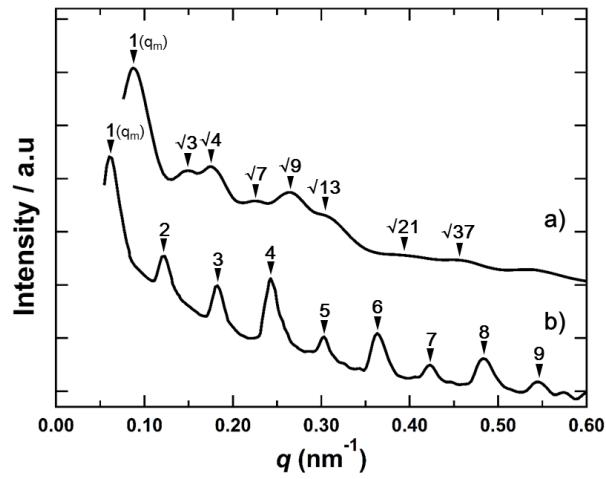
### 5.3 Results and Discussion



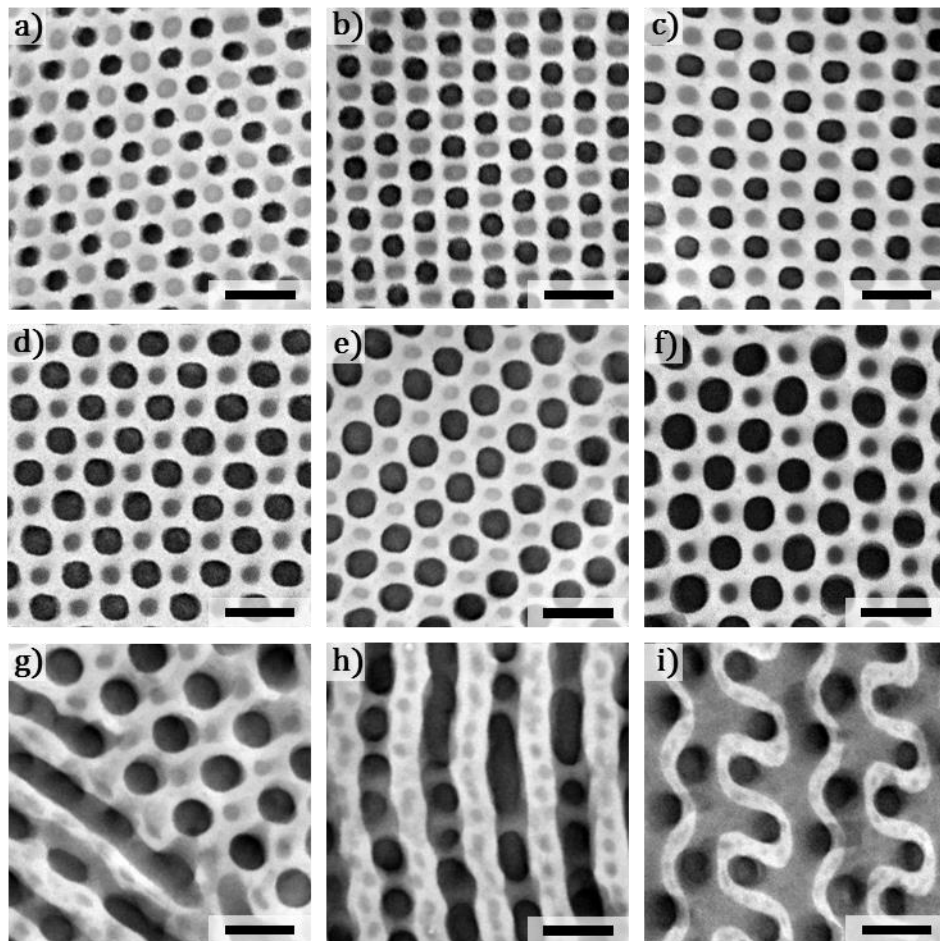
**Figure 5.2.** TEM images of (a) ISP-X and (b) ISP-Y. (c) Image of ISP-Y stained only with  $I_2$ , which was shot perpendicular to lamellar surface with a slight tilt angle. All Scale bars represent 100 nm.

Figure 5.2 presents TEM images of the two parent ISP triblock terpolymers. The ISP-X in Figure 5.2 (a) creates a hierarchical structure with double hexagonal symmetry, in which large P cylinders with a hexagonal symmetry are surrounded by six thin I cylinders.<sup>26</sup> The ISP-Y exhibits a sphere-in-lamellae structure as shown in Figure 5.2 (b), where I and S phase create alternative lamellae. The relative diffraction peak positions,  $q/q_m$  ( $q_m$  corresponds to the  $q$  value for the primary peak) shown in Figure 5.3 reveal that ISP-X exhibits hexagonal symmetry and ISP-Y displays a lamellar structure. The P cylinder-to-cylinder and interlamella distances estimated from the  $q_m$  values are 83 and 104 nm, respectively, both of which correspond well with the TEM results. Although P component has the largest electron density (I, 0.512 electron/cm<sup>3</sup>; S, 0.565 electron/cm<sup>3</sup>; P, 0.608 electron/cm<sup>3</sup>), the interference peaks of the P spheres of ISP-Y were not observed in the SAXS data shown in Figure 5.3 (b). This is probably due to the small composition of the P component. Figure 5.2 (c) demonstrates that the minor P component forms spherical domains packed hexagonally within a single layer at

the center of S lamellae and the diameter of the P spheres is estimated to be about 11 nm from the TEM image.<sup>19</sup>



**Figure 5.3.** SAXS patterns of the two parent ISP triblock terpolymers; (a) ISP-X and (b) ISP-Y. The black inverted triangles indicate the relative peak positions.



**Figure 5.4.** TEM images of the blend samples: (a) Blend(9/1), (b) Blend(8/2), (c) Blend(7/3), (d) Blend(6/4), (e) Blend(5/5), (f) Blend(4/6), (g) Blend(3/7), (h) Blend(2/8), and (i) Blend(1/9). Images from (a) to (f) display the cross sections of cylindrical morphologies. All scale bars represent 100 nm.

TEM images of all the blend samples listed in Table 5.2 are shown in Figure 5.4. Surprisingly, tetragonally packed cylinders, in which the cylinders pack tetragonally with alternating I and P domains, were observed from Blend(9/1) to Blend(4/6) covering a wide range of  $\phi_P/\phi_I$ . Generally, tetragonal-packed cylinders are favored for ABC triblock terpolymers with symmetric compositions concerning A and C; i.e.,  $\phi_C/\phi_A$  is close to unity. A and C domains are forced to stay at alternating locations within B matrix phase.<sup>36</sup> Evidently, from the standpoint of filling space, hexagonal packing is more favorable than tetragonal one as is shown in Figure 5.2 (a) for an ISP triblock terpolymer with asymmetric end-block components.<sup>37</sup> That is, ABC triblock terpolymers with asymmetric end-block components prefer to obtain hexagonally packed cylinders. Later, we will give a more precise account of the characteristic cylinders packed tetragonally with alternating different-sized I and P domains.

At Blend(3/7), tetragonal cylinders and perforated lamella-like morphology were found simultaneously, indicating this blend is in a transit region. The Blend(2/8) shows a perforated lamella-like morphology over the whole area, where a perforated layer of I and a complex layer of S/P align alternately, in addition, P spheres are distributed at the center of S phase. A TEM image of the Blend(1/9) has revealed a double gyroid structure, in which I component conforms the alternative gyroid networks embedded in a complex matrix phase of S and P components. For the matrix phase, P component creates spherical domains because its volume fraction is quite low, 0.03, and consequently the P spheres are periodically distributed

over the triply periodic gyroid minimal surface.<sup>35,38,39</sup> Since the specific tetragonal cylinders will be considered more fully later, I shall outline here only briefly Blend(2/8) and Blend(1/9).

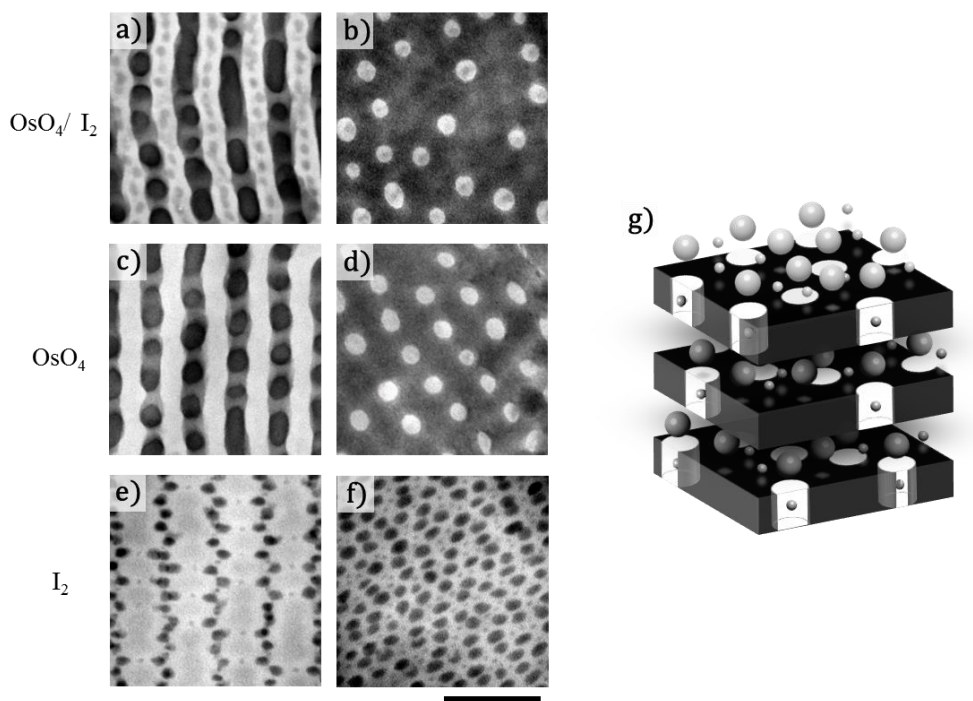


**Figure 5.5.** TEM images of Blend(2/8); staining agent for (a) and (b) is  $\text{OsO}_4/\text{I}_2$ , that for (c) and (d) is  $\text{OsO}_4$ , while that for (e) and (f) is  $\text{I}_2$ . The images (a), (c) and (e) are taken parallel to the lamellar phase, whereas the images (b), (d) and (f) are shot perpendicular to the perforated lamellae. The scale bar represents 200 nm. (g) is a schematic representation of the current morphology, in which black and gray domain represent I and P phase, respectively.

Figure 5.5 compares the TEM images of Blend(2/8) stained with different staining reagents and taken from different directions. Forming perforated lamellae of I component was manifested by Figure 5.5 (c) and (d). Figure 5.5 (a) confirms the alignment of P spheres within S phase. Figure 5.5 (e) and (f) reveal that P phase consists of small and large spherical domains, both of which are distributed under regulation, particularly some small P sphere are located at the mid of I lamellae. By comparing Figure 5.5 (b) with 5.5 (d), we can also notice the presence of some P spheres in the holes of I phase. That is, P spheres are always distributed in S matrix,

in which small and large P spheres are located in between I perforated phases, while some small P spheres are placed in the holes of I perforated phases. Figure 5.5 (g) represent the schematic illustration of the perforated morphology.

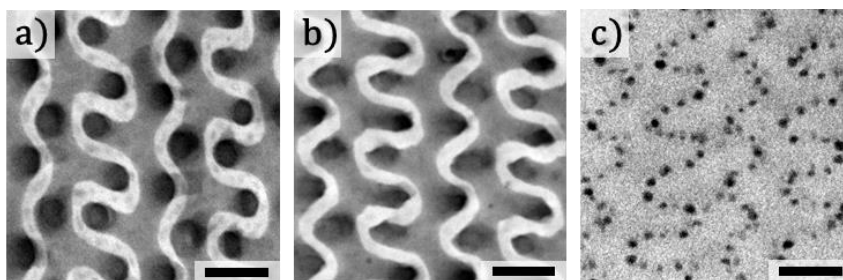


**Figure 5.6.** TEM images of Blend(1/9); stained with OsO<sub>4</sub>/ I<sub>2</sub> (a), OsO<sub>4</sub> (b) and I<sub>2</sub> (c). The images represent the projections of a double gyroid structure through the [112] plane. All scale bars represent 100 nm.

Figure 5.6 shows the TEM images of Blend(1/9) stained with different reagents. Figure 5.6 (a) corresponds well to the [112] projection of a double gyroid structure. Although the double gyroid structure is composed of three components from ISP triblock terpolymers, the ordered bicontinuous double gyroid is developed, in which I component forms two gyroid networks in an S matrix. By comparing Figure 5.6 (b) with Figure 5.6 (c), P spherical domains can be confirmed to lie on the S matrix. Considering the geometry of a double gyroid structure, the P spheres could be aligned on the gyroid triply periodic minimal surface or close.<sup>35,38,39</sup> Sphere-in-gyroid structure was found in ISP-61 as shown in Chapter 4, in which equal-sized spherical domains are distributed over the gyroid surface. Interestingly, in Blend(1/9), spheres aligned over the gyroid surface are unequal in size, suggesting long and short P chains are not homogeneously dispersed in the morphology.

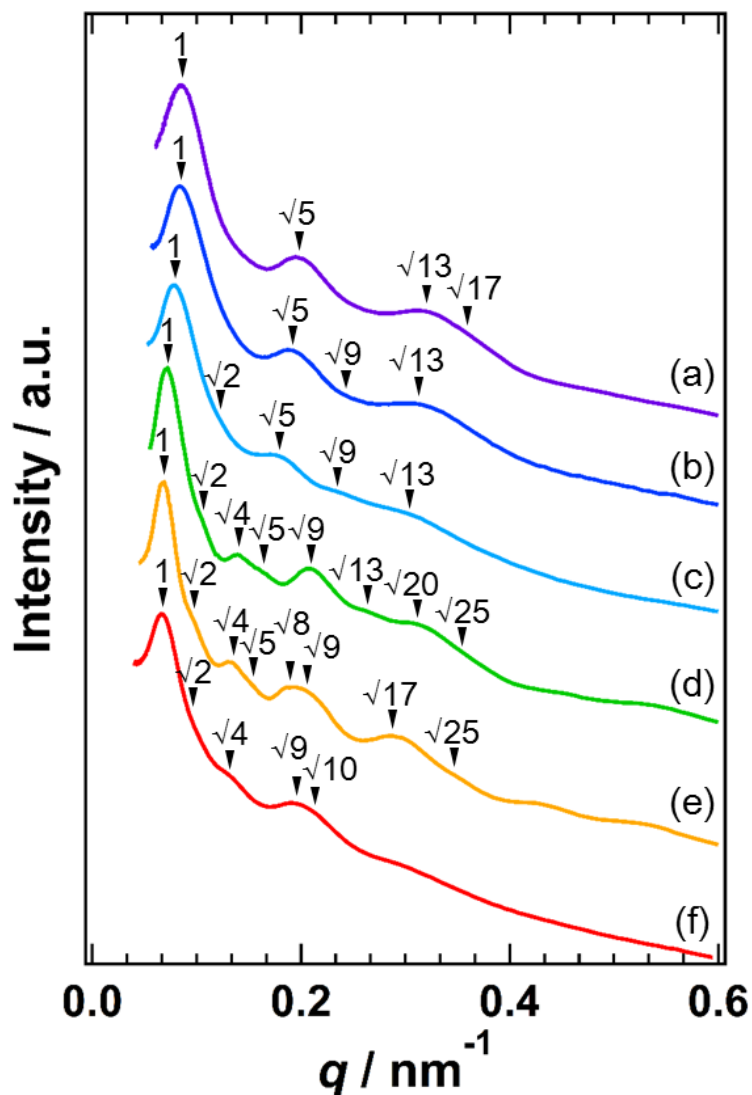


**Figure 5.7.** SAXS profiles of the blend samples in which tetragonal cylinders were observed from TEM. The sequence of peaks pointed out by inverted triangles is consistent with a tetragonal cylindrical arrangement. (a) Blend(9/1), (b) Blend(8/2), (c) Blend(7/3), (d) Blend(6/4), (e) Blend(5/5), and (f) Blend(4/6)

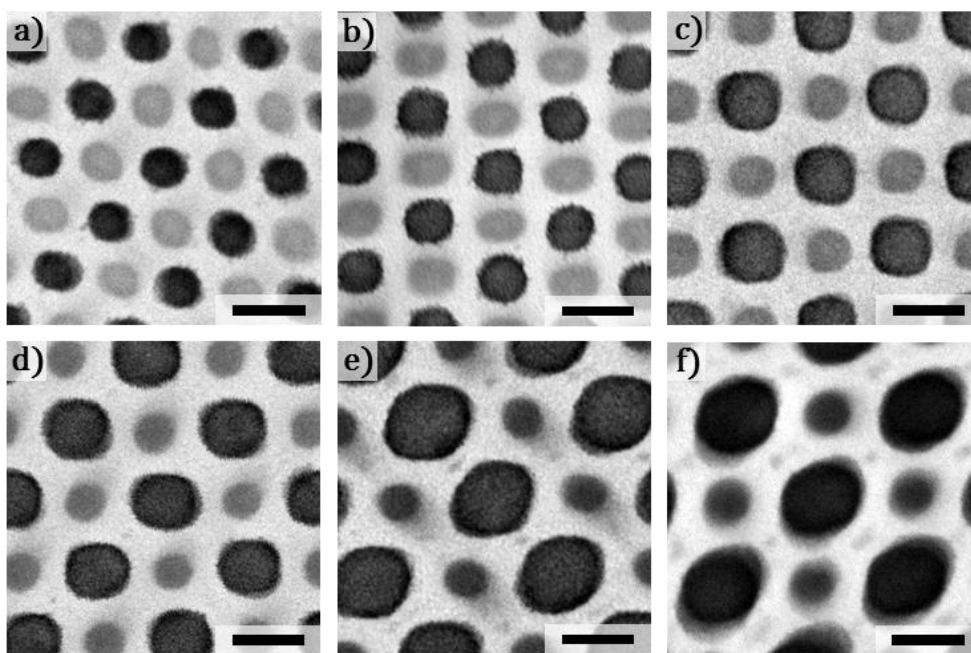
Now let me return to the cylindrical structures obtained from Blend(9/1) to Blend (4/6). It should be stressed on the fact that TEM images identify local structures of bulk morphologies, whereas SAXS measurement provides structural information covering a wide area. Figure 5.7 shows the azimuthally integrated SAXS profiles for the blend samples

exhibiting tetragonal-packed cylinders in their TEM images. All the SAXS patterns reveal the tetragonal manner from a series of diffraction peaks positioned in the order of the  $q/q_m$  ratio, i.e., 1,  $\sqrt{2}$ ,  $\sqrt{4}$ ,  $\sqrt{5}$ ,  $\sqrt{8}$ ,  $\sqrt{9}$ , and so on. The domain distances between neighboring I cylinders or P cylinders estimated from the first order peaks are summarized in Table 5.3. It is evident that the domain distance increases monotonically with increasing the blend ratio of ISP-Y.

**Table 5.3.** Summary of the Domain Distance (D) and the Diameter of Cylindrical Domains

Calculated from Eq 7						
	Blend (9/1)	Blend (8/2)	Blend (7/3)	Blend (6/4)	Blend (5/5)	Blend (4/6)
D [nm]	72	75	81	87	91	95
I cylinder [nm]	32	38	41	50	55	61
P cylinder [nm]	34	34	34	34	33	31
No. of chains in a unit cell <sup>a</sup>	N	1.07N	1.22N	1.39N	1.49N	1.60N

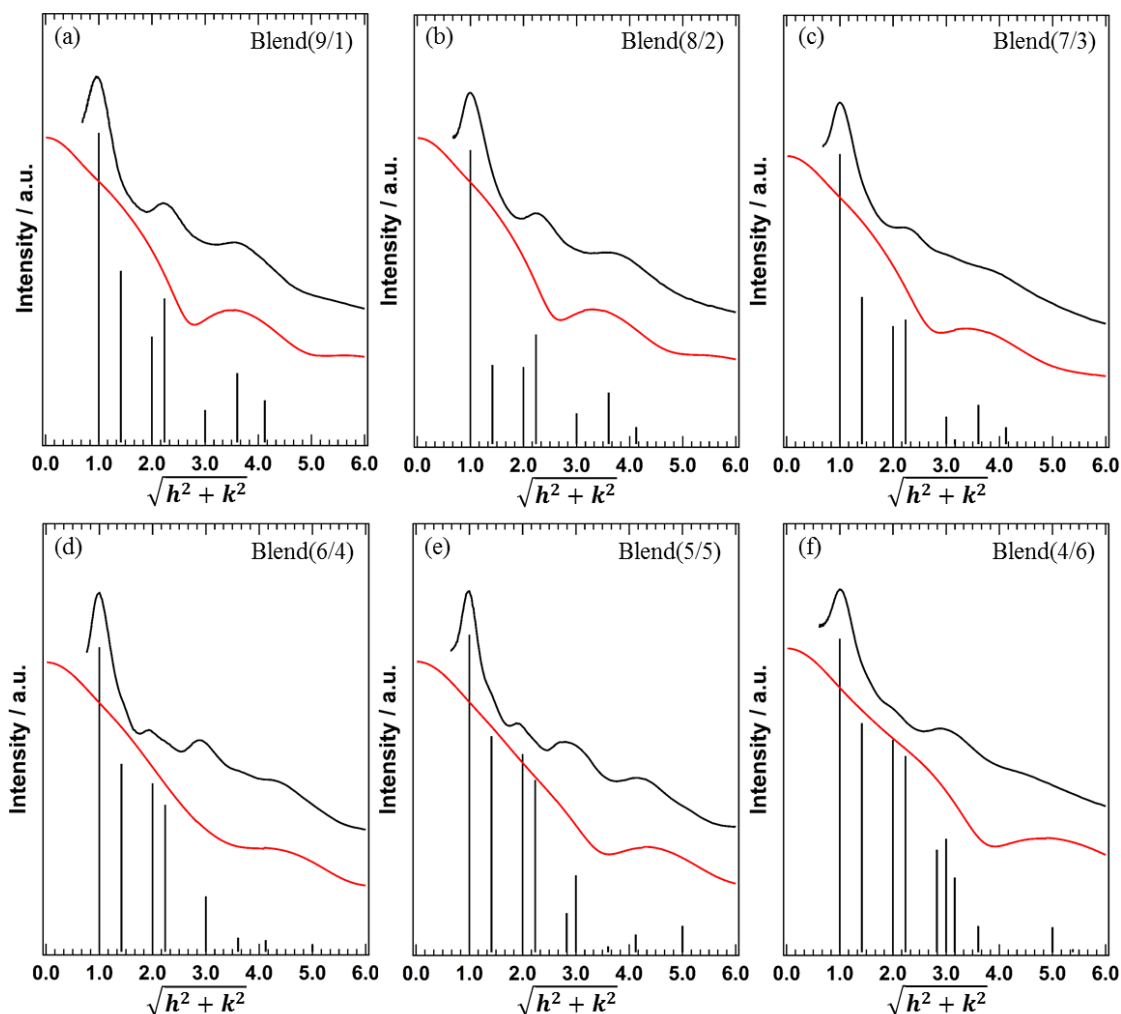
<sup>a</sup> Number of chains within a unit cell are estimated considering the molecular weight of the parent triblocks and the blend ratios, assuming that the number involved in Blend(9/1) is N



**Figure 5.8.** TEM images of the blend samples at high magnification: (a) Blend(9/1), (b) Blend(8/2), (c) Blend(7/3), (d) Blend(6/4), (e) Blend(5/5), and (f) Blend(4/6). All scale bars represent 50 nm.

The TEM images of the blend samples at high magnification are shown in Figure 5.8. These images clearly ensure tetragonal-packed cylinders and the increase in domain distance. It should be noted that we can easily find that the shape of the cross section of I cylinders is not just circle but rather close to square especially in Blend(7/3) and Blend(6/4); that is, the I domain is a rod rather than a cylinder in these blends. In our previous work, rods with 4-fold symmetry, which we called “rectangular shaped cylinder”,<sup>34</sup> were also found from binary blends of ISP triblock terpolymers with symmetric different chain length of the two end blocks. I concluded that the domains with nonconstant mean curvature was formed due to weak localization of the junction point of two parent triblock terpolymers along the domain interface to release the conformational entropy losses of end blocks as well as centered S block. The I rods observed in this work are possibly generated by the same origin. Here we can notice that

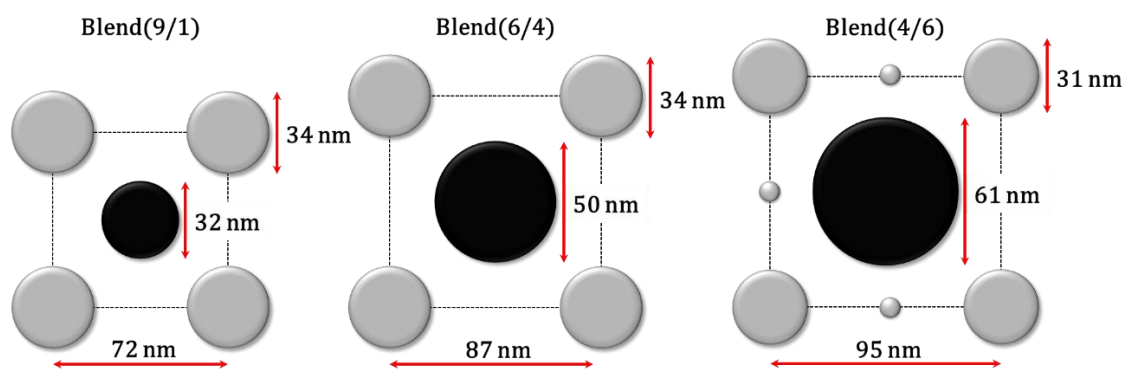
the size of I domain is getting larger with increasing blend ratios of ISP-Y. This trend reflects the molecular design; as increasing the ratio of ISP-Y with long I chain, the volume fraction of I phase increases as is evident in Table 5.2. This will lead us further into a consideration of SAXS patterns shown in Figure 5.7. The difference in the domain size makes a large contribution to the scattering pattern. It is clearly confirmed that the relative peak positions and the relative intensities of the diffraction peaks have been changed systematically depending on the blend ratios, even though all samples indicate tetragonal-packed cylinders. Hence, we conducted the calculation of scattering intensities of tetragonal-packed cylinders considering their domain sizes. For simplicity, the calculation was carried out based on the simplified structure factors, assuming both I and P domains possess cylindrical (circle) domains and the small P domains are neglected. See the Appendix for the details of the formulation



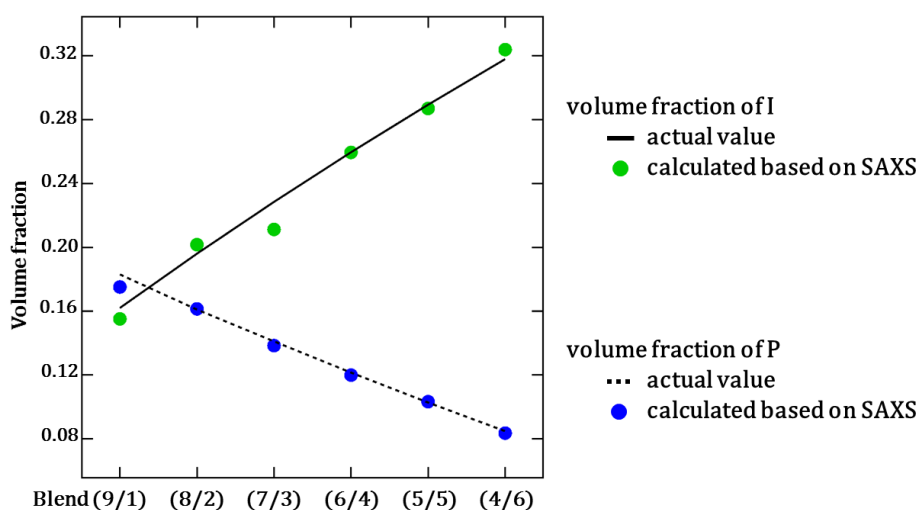
**Figure 5.9.** SAXS profiles of the blend samples and the intensity calculation results for each  $\sqrt{h^2 + k^2}$ , where  $h$  and  $k$  denote Miller index: (a) Blend(9/1), (b) Blend(8/2), (c) Blend(7/3), (d) Blend(6/4), (e) Blend(5/5), and (f) Blend(4/6). The vertical bars express the relative intensities calculated from eq 7 in Appendix considering the sizes of I and P cylinders. The red curves represent the calculated form factor of cylindrical domains based on eq 4.

Figure 5.9 compares the calculated diffraction strengths associated with eq 7 in Appendix and the experimental scattering profiles. As seen in Figure 5.9, the calculated intensities expressed with the vertical bars agree well with the SAXS data and the bumps of the calculated form factors fit closely with those of the experimental scattering patterns.

Especially in Blend (5/5) in which many peaks were detected, the relative intensities and peak positions at (10), (11), (20), (21), (22), and (30) reflections are in good agreement with the experimental results. The diameters of cylindrical domains determined from the calculation are summarized in Table 5.3. Schematic illustrations at three X/Y compositions based on Table 5.3 are shown in Figure 5.10. From the values in Tables 5.2 and 5.3, I have confirmed that the volume fractions evaluated from domain distance and domain size match well the exact volume fractions of the blend samples, as is clearly indicated in Figure 5.11. It is apparent from Table 5.3 that the diameter of I cylinder increases monotonically and that of P cylinder decreases very weakly as increasing the blend ratio of ISP-Y with long I chain and short P chain. These results can be understood by simply considering the number of chains within a unit cell increases from Blend(9/1) to (4/6). If the number of chains consisting in the  $72 \times 72$  nm<sup>2</sup> unit cell of Blend(9/1) is taken to be N, 1.6N chains would be required to construct the  $95 \times 95$  nm<sup>2</sup> unit cell of Blend(4/6), considering the total molecular weights of ISP-X and -Y and the blend ratios, and the estimated values are listed at the bottom of Table 5.3. This table tells the reason that the domain size of P spheres is almost constant even though the volume fraction of P component decreases, while that of I increases considerably with decreasing X/Y ratio. Thus, the present results suggest that the domain size directly depends on composition of samples even though all samples belong to the same space group (p2mm symmetry).



**Figure 5.10.** Schematic illustration of cross sections of tetragonally packed cylinders. The domain size and domain distance of each blend sample are based on the data in Table 5.3. Spherical small P domains located between P cylinders are added for Blend(4/6) as observed in Figures 5.8 and 5.12. Black and gray domains present I and P phases, respectively.



**Figure 5.11.** Volume fraction plots of various blends based on Table 5.2 and Table 5.3. Solid and dashed line indicate the exact volume fractions of I and P component according to Table 5.2, respectively. The volume fractions of I and P phases estimated from SAXS results are identified as green and blue circles.

Figure 5.11 shows the plot of various blends vs volume fraction of I and P components based on Table 5.2 and Table 5.3. The calculation results assuming all the I and P domains are cylinders are plotted as green and blue circles. Both circles are nearly on the lines of actual volume fraction of blend samples, which clearly indicates the volume fractions estimated from the calculation results match well with the exact volume fractions of the blend samples.

So far, I reported on the evident advantage of tetragonal-packed cylindrical or square-rod-like structures over others, even the case in which the size of I and P domains is highly asymmetric. There must be several reasons for this featured structure. One possible reason is the surface area difference. If Blend(6/4) is held up as an example, we notice the S/P surface area for the hexagonal arrangement is about  $\sqrt{2}$  times larger than the tetragonal one; this simply means the hexagonal pattern is unfavorable. In reality, the present blend system chose tetragonal arrangement by sacrificing the conformational entropy of S chains. The small difference in two interaction parameters, i.e.,  $\chi_{S-P} > \chi_{S-I}$ , probably helps to realize this size asymmetric pattern.<sup>26</sup> The other possibility is the repulsive force between I and P. Although these two components are not connected directly, in other words, no I/P interface exists, there might generate the long-range repulsive interaction between I and P, since these two components possess the highest interaction strength ( $\chi_{S-P} \gg \chi_{S-P} \cong \chi_{S-I}$ ). This could cause geometrically alternative domain packing of I and P phases in the matrix of S.

Moreover, we should not overlook the other specific features of the current morphologies. If we see the TEM images in Figure 5.8 (a)-(f) more carefully, quite small domains can be seen between I rods or P cylinders in Blend(5/5) and Blend(4/6). The small domains could not be observed in the other blend samples. Then we stained the blend samples with  $I_2$  only to investigate the exact locations of the small P domains.

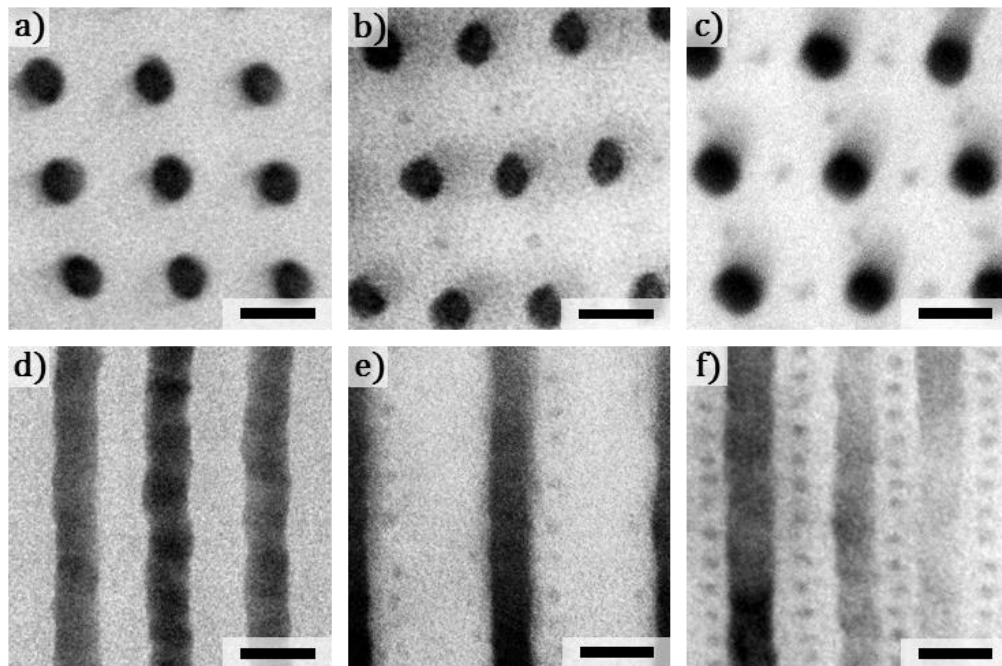


**Figure 5.12.** TEM images of blend samples stained with  $I_2$ : (a, d) Blend(6/4), (b, e) Blend(5/5), and (c, g) Blend(4/6). Top images show the cross-sectional view of P cylinders, and bottom ones present their side views. The transverse views of Blend(6/4) and Blend(4/6) were obtained by the projection of [100] direction, while that of Blend(5/5) was observed from the [110] direction. For thin films (film thickness < domain distance), the side-view projections of cylindrical structures significantly depend on the observing direction. All scale bars represent 50 nm.

Figure 5.12 compares the TEM images of Blend(6/4), Blend(5/5), and Blend(4/6) stained with  $I_2$ . The upper images represent the cross sections of P cylinders while the bottom ones show their transverse views. P cylinders with tetragonal symmetry were simply found in Blend(6/4). On the other hand, small domains were observed in addition to P cylinders in Blend(5/5) and Blend(4/6). From the images for Blend(4/6), every large domain is surrounded by four small ones. Interestingly, Blend(5/5) presents that the P spheres do not align with regularity as shown in Figure 5.12 (b) and (e). These results reveal that the number of the P

spherical domains increases as increasing the ratio of ISP-Y with short P chain, resulting in an ordered array. The diameter of P spheres estimated from TEM is about 10 nm, which is close to the size of P sphere formed from neat ISP-Y. This implies that the P spheres are simply composed of the short P chains of ISP-Y.

For the moment, we shall discuss the asymmetric double tetragonal domain orientation with coexistent phase of spheres and cylinders. This unusual morphology was highly extended for binary blends of ABC triblock terpolymers with asymmetric different chain length of two end blocks.

The number of small P spheres increases gradually with the increase of fraction of ISP-Y as shown in Figure 5.12, resulting in the periodic sequence of P spheres aligning along P cylinders with tetragonal symmetry. It is quite evident that short P chains of ISP-Y conform the P spheres because the size of P spheres is similar to that of neat ISP-Y as shown in Figure 5.2 (b). That is the excess short P chains can be expelled from P cylindrical domains, resulting in the formation of spherical domains. This phenomenon is analogous to coexisting phase for binary blends of AB diblock copolymers. Above a critical value of the length ratio of the constituent two diblock copolymers, the blend tends to choose two coexistent phases: one consists of two diblock copolymers, and the other is composed of the short diblock chains only. The critical value of the length ratio was predicted to be about 5.<sup>40,41</sup>

In the present work, the chain length difference of I chains is not large enough to cause the separation of short and long chains, while it is large enough for P component, and hence short P chains are split into two domains so as to form the unusual structures with coexistent phase. At the same time, P spheres are located at the intermediate position between P cylinders because of the geometrical constraint of S chains. The P spheres can help to fill space well and admits the blend system stays still within the category of co-tetragonally packed domain structure. Consequently, in the present work, we have found tetragonal-packed

cylinders at a wide range of  $\phi_P/\phi_I$  from 0.27 to 1.13.

## 5.4 Conclusion

In this study, we examined self-assembled structures from binary blends of ISP triblock terpolymers with asymmetric chain length of two end blocks. TEM and SAXS were used to investigate the morphological features. By blending the two ISP triblock terpolymers, nine blends from 9/1 to 1/9 were prepared, where coarrayed tetragonal packed cylinders were observed covering wide range of volume fraction. SAXS analysis revealed that tetragonal cylinders are stable up to the Blend(4/6), in which  $\phi_P/\phi_I$  is 0.27. This is unusual case for monodisperse ABC triblock terpolymers. What is interesting in this work is not only the fact that coarrayed tetragonal cylinders were displayed on a wide range of volume fraction but that there are additional specific features: (1) I cylindrical domains was metamorphosed into rod domains in which the interface has nonconstant mean curvature, (2) the cross-sectional area ratio of I domain/P domain is gradually increased with the volume fraction of each component, and (3) spherical and cylindrical domains of P component coexist. The different chain length is definitely attributed to these features, and we expect that more interesting and complex morphologies will be developed from blend systems with chain length difference.

## 5.5 Appendix

### Calculation of scattering intensities of cylindrical structures

We calculated the structure factor  $F(q)$  related to lattice structures in the scattering intensity  $I(q)$  considering the absolute size of cylinders. The scattering intensity  $I(q)$  can be expressed as

$$I(q) \propto |F(q)|^2 \quad (1)$$

$F(q)$  is referred as the structure factor

$$F(q) = \sum_j f_j \exp(-iq \cdot r_j) \quad (2)$$

$$f_j = \rho_{ej} f'_j \quad (3)$$

where  $j$  is the number of a scattering element in the unit cell,  $r_j$  is the  $j$ th domain position,  $f'_j$  is the form factor and  $\rho_{ej}$  is the electron density.

The expression of the form factor of cylindrical domain of radius  $R$  and length  $H$  is

$$f'_j = \int_0^{\pi/2} \left\{ \left[ \frac{2J_1(qR \sin \varphi)}{qR \sin \varphi} \right] \left[ \frac{\sin\left(\frac{qH}{2} \cos \varphi\right)}{\left(\frac{qH}{2} \cos \varphi\right)} \right] \right\}^2 \sin \varphi d\varphi \quad (4)$$

where  $J_1(x)$  is the first order Bessel function.  $\varphi$  is defined as the angle between cylinder axis and the scattering vector,  $q$ . The integral over  $\varphi$  averages the form factor over all possible orientations of the cylinder with respect to  $q$ . Applying the microdomain structures of ABC triblock terpolymer to Eq 2 leads to the following equation,

$$F(q) = \sum f_A \exp(-iq \cdot r_{jA}) + \sum f_B \exp(-iq \cdot r_{jB}) + \sum f_C \exp(-iq \cdot r_{jC}) \quad (5)$$

Therefore, we can rewrite Eq 5 as an equation considering the difference between the electron densities of A or C domains and that of B matrix domain

$$F(q) = \Delta\rho_{eAB} f'_A \sum \exp(-iq \cdot r_{jA}) + \Delta\rho_{eCB} f'_C \sum \exp(-iq \cdot r_{jC}) + \rho_{eB} \{ f'_A \sum \exp(-iq \cdot r_{jA}) + f'_B \sum \exp(-iq \cdot r_{jB}) + f'_C \sum \exp(-iq \cdot r_{jC}) \} \quad (6)$$

where  $\Delta\rho_{eAB} = \rho_{eA} - \rho_{eB}$  and  $\Delta\rho_{eCB} = \rho_{eC} - \rho_{eB}$ . We can neglect the third term regarding the scattering from B matrix domain because the term explains the structure factor from a unit

lattice with the uniform electron density of  $\rho_{eB}$ . The structure factor can be expressed with Miller index of the diffraction lattice face (hkl) as  $F(hkl)$ ,

$$F(hkl) = \Delta\rho_{eAB}f'_A \sum \exp[-2\pi i(x_{jA}h + y_{jA}k + z_{jA}l)] + \Delta\rho_{eCB}f'_C \sum \exp[-2\pi i(x_{jC}h + y_{jC}k + z_{jC}l)] \quad (7)$$

where  $(x_j, y_j, z_j)$  are the coordinates of the  $j$ th scattering element. In the case of ISP triblock terpolymer system ( $\rho_{eI}$ :0.512 electron/cm<sup>3</sup>,  $\rho_{eS}$ :0.565 electron/cm<sup>3</sup>,  $\rho_{eP}$ :0.608 electron/cm<sup>3</sup>),  $\Delta\rho_{eIS} = -0.053$  electron/cm<sup>3</sup> and  $\Delta\rho_{ePS} = 0.043$  electron/cm<sup>3</sup>, we did use  $\Delta\rho_{eIS} \neq -\Delta\rho_{ePS}$  to obtain the more accurate scattering intensity unlike our previous work.<sup>42</sup> In the present work, we can neglect  $l$  because cylindrical structure is a two-dimensional crystal.

## 5.6 References

- 1 Bates, F. S.; Fredrickson, G. H. Block Copolymers—Designer Soft Materials. *Physics Today* **1999**, *52*, 32-38.
- 2 Abetz, V.; Simon, P. F. W. Phase Behaviour and Morphologies of Block Copolymers. *Adv. Polym. Sci.* **2005**, *189*, 125–212.
- 3 Matsushita, Y. Studies on Equilibrium Structures of Complex Polymers in Condensed Systems. *J. Polym. Sci., Part B: Polym. Phys.* **2000**, *38*, 1645-1655.
- 4 Matsushita, Y.; Choshi, H.; Fujimoto, T.; Nagasawa, M. Preparation and Morphological Properties of a Triblock Copolymer of the ABC Type. *Macromolecules* **1980**, *13*, 1053-1058.
- 5 Richards, R. W.; Thomason, J. L. A small angle neutron scattering investigation of block copolymers of styrene and isoprene in the solid. *Polymer* **1981**, *22*, 581–589.
- 6 Helfand, E.; Wasserman, Z. R. Block Copolymer Theory. 4. Narrow Interphase Approximation. *Macromolecules* **1976**, *9*, 879-888.
- 7 Leibler, L. Theory of Microphase Separation in Block Copolymers. *Macromolecules* **1980**, *13*, 1602-1617.
- 8 Hasegawa, H.; Tanaka, H.; Yamasaki, K.; Hashimoto, T. Bicontinuous Microdomain Morphology of Block Copolymers. 1. Tetrapod-Network Structure of Polystyrene-Polyisoprene Diblock Polymers. *Macromolecules* **1987**, *20*, 1651-1662.
- 9 Bates, F. S.; Schulz, M. F.; Khandpur, A. K.; Forster, S.; Rosedale, J. H. Fluctuations, Conformational Asymmetry and Block Copolymer Phase Behaviour. *Faraday Discuss.* **1994**, *98*, 7-18.

## Chapter 5

- 10 Khandpur, A. K.; Forster, S.; Bates, F.S.; Hamley, I. W.; Ryan, A. J.; Bras, W.; Almdal, K.; Mortensen, K. Polyisoprene-Polystyrene Diblock Copolymer Phase Diagram near the Order-Disorder Transition. *Macromolecules* **1995**, *28*, 8796-8806.
- 11 Matsen, M. W. Effect of Architecture on the Phase Behavior of AB-Type Block Copolymer Melts. *Macromolecules* **2012**, *45*, 2161-2165.
- 12 Mogi, Y.; Kotsuji, H.; Kaneko, Y.; Mori, K.; Matsushita, Y.; Noda, I. Preparation and Morphology of Triblock Copolymers of the ABC Type. *Macromolecules* **1992**, *25*, 5808-5411.
- 13 Suzuki, J; Seki, M.; Matsushita, Y. The tricontinuous double-gyroid structure from a three-component polymer system. *J. Chem. Phys.* **2000**, *112*, 4862-4868.
- 14 Gido, S.P.; Schwark, D.W.; Thomas, E.L.; Goncalves, M.C. Observation of a Non-Constant Mean Curvature Interface in an ABC Triblock Copolymer. *Macromolecules* **1993**, *26*, 2636-2640.
- 15 Matsushita, Y.; Tamura, M.; Noda, I. Tricontinuous Double-Diamond Structure Formed by a Styrene-Isoprene-2-Vinylpyridine Triblock Copolymer. *Macromolecules* **1994**, *27*, 3680-3682.
- 16 Ishige, R.; Higuchi, T.; Jiang, X.; Mita, K.; Ogawa, H.; Yokoyama, H.; Takahara, A.; Jinnai, H. Structural Analysis of Microphase Separated Interface in an ABC-Type Triblock Terpolymer by Combining Methods of Synchrotron-Radiation GI-SAXS and EM. *Macromolecules* **2015**, *48*, 2697-2705.
- 17 Breiner, U.; Krappe, U.; Stadler, R. Evolution of the “knitting pattern” morphology in ABC triblock copolymers. *Macromol. Rapid Commun.* **1996**, *17*, 567-575.
- 18 Epps, T. H. III.; Cochran, E. W.; Hardy, C. M.; Bailey, T. S.; Waletzko, R. S.; Bates, F. S. Network Phases in ABC Triblock Copolymers. *Macromolecules* **2004**, *37*, 7085-7088.
- 19 Zhang, W.; Wang, Z.-G. Morphology of ABC Triblock Copolymers. *Macromolecules* **1995**, *28*, 7215-7223.
- 20 Tang, P.; Qiu, F.; Zhang, H.; Yang, Y. Morphology and phase diagram of complex block copolymers ABC linear triblock copolymers. *Phys Rev. E* **2004**, *69*, 031803.
- 21 Qin, J.; Bates, F. S.; Morse, D. C. Phase Behavior of Nonfrustrated ABC Triblock Copolymers: Weak and Intermediate Segregation. *Macromolecules* **2010**, *43*, 5128-5136.
- 22 Liu, M.; Li, W.; Qiu, F.; Shi, A.-C. Theoretical Study of Phase Behavior of Frustrated ABC Linear Triblock Copolymers. *Macromolecules* **2012**, *45*, 9522-9530.
- 23 Tureau, M. S.; Rong, L.; Hsiao, B. S.; Epps, T. H. III. Phase Behavior of Neat Triblock Copolymers and Copolymer Homopolymer Blends Near Network Phase Windows. *Macromolecules* **2010**, *43*, 9039-9048.
- 24 Suzuki, J.; Furuya, M.; Iinuma, M.; Takano, A.; Matsushita, Y. Morphology of ABC Triblock Copolymer homopolymer Blend Systems. *J. Polym. Sci., Part B: Polym. Phys.* **2002**, *40*, 1135-1141.

## Chapter 5

- 25 Sugiyama, M.; Shefelbine, T. A.; Vigild, M. E.; Bates, F. S. Phase Behavior of an ABC Triblock Copolymer Blended with A and C Homopolymers. *J. Phys. Chem. B* **2001**, *105*, 12448-12460.
- 26 Izumi, Y.; Yamada, M.; Takano, A.; Matsushita, Y. A New Periodic Pattern with Five-Neighbored Domain Packing from ABC triblock Terpolymer/B Homopolymer Blend. *J. Polym. Sci., Part B: Polym. Phys.* **2015**, *53*, 907-911.
- Note: In this work, it has been confirmed that ISP/S homopolymer blend system show asymmetric phase diagram. That is, ISP/S blends possess double hexagonal-packed cylindrical structure composed of large P cylinders surrounded by six thin I cylinders covering wide range of  $\phi_P/\phi_I$ , while  $\phi_P/\phi_I$  region for double hexagonal cylinders with thick I cylinders surrounded by six thin P cylinders is narrow. This asymmetric phase diagram could be originated from the difference in  $\chi$  values between S-I and S-P ( $\chi_{S-P} > \chi_{S-I}$ ).
- 27 Dotera, T. Tricontinuous Cubic Structures in ABC A C Copolymer and Homopolymer Blends. *Phys. Rev. Lett.* **2002**, *89*, 205502.
- 28 Goldacker, T.; Abetz, V. Core-Shell Cylinders and Core-Shell Gyroid Morphologies via Blending of Lamellar ABC Triblock and BC Diblock Copolymers. *Macromolecules* **1999**, *32*, 5165-5167.
- 29 Birshstein, T. M.; Polotsky, A. A.; Abetz, V. Mixed Supercrystalline Structures in Mixtures of ABC Triblock and ab(bc) Diblock Copolymers. *Macromol Theory Simul* **2001**, *10*, 700-718.
- 30 Goldacker, T.; Abetz, V.; Stadler, R.; Erukhimovich, I.; Leibler, L. Non-centrosymmetric superlattices in block copolymer blends. *Nature* **1999**, *398*, 137-139.
- 31 Wickham, R. A.; Shi, A.-C. Noncentrosymmetric Lamellar Phase in Blends of ABC Triblock and ac Diblock Copolymers. *Macromolecules* **2001**, *34*, 6487-6494.
- 32 Abetz, V.; Goldacker, T. Formation of superlattices via blending of block copolymers. *Macromol. Rapid Commun.* **2000**, *21*, 16-34.
- 33 Matsushita, Y.; Suzuki, J.; Izumi, Y.; Matsuoka, K.; Takahashi, S.; Y. Aoyama,; Mihira, Y.; Takano, A. A New Periodic Pattern with Five-Neighbored Domain Packing from ABC Triblock Terpolymer B Homopolymer Blend. *J. Chem. Phys.* **2010**, *133*, 194901.
- 34 Asai, Y.; Yamada, K.; Yamada, M.; Takano, A.; Matsushita, Y. Formation of Tetragonally-Packed Rectangular Cylinders from ABC Block Terpolymers Blends. *ACS Macro Letters* **2014**, *3*, 166-169.
- 35 Asai, Y.; Takano, A.; Matsushita, Y. Creation of Cylindrical Morphologies with Extremely Large Oblong Unit Lattices from ABC Block Terpolymers. *Macromolecules* **2015**, *48*, 1538-1542.
- 36 Matsen, M. W. Gyroid versus double-diamond in ABC triblock copolymer melts. *J. Chem. Phys.* **1998**, *108*, 785-796.

## Chapter 5

- 37 Tyler, C. A.; Qin, A.; Bates, F. S.; Morse, D. C. SCFT Study of Nonfrustrated ABC Triblock Copolymer Melts. *Macromolecules* **2007**, *40*, 4654-4668.
- 38 Dotera, T.; Kimoto, M.; Matsuzawa, J. Hard spheres on the gyroid surface. *Interface Focus* **2012**, *2*, 575-581.
- 39 Kirkensgaard, J. J. K. Kaleidoscopic tilings, networks and hierarchical structures in blends of 3-miktoarm star terpolymers. *Interface Focus* **2012**, *2*, 602-607.
- 40 Matsen, M.W. Immiscibility of large and small symmetric diblock copolymers. *J. Chem. Phys.* **1995**, *103*, 3268-3271.
- 41 Yamaguchi, D.; Hashimoto, T. A Phase Diagram for the Binary Blends of Nearly Symmetric Diblock Copolymers. 1. Parameter Space of Molecular Weight Ratio and Blend Composition. *Macromolecules* **2001**, *34*, 6495-6505.
- 42 Mogi, Y.; Nomura, M.; Kotsuji, H.; Ohnishi, K.; Matsushita, Y.; Noda, I. Superlattice Structures in Morphologies of the ABC Triblock Copolymers. *Macromolecules* **1994**, *27*, 6755-6760.

## CHAPTER 6

# Tricontinuous Double Diamond Networks from Binary Blends of ABC Triblock Terpolymers

### 6.1 Introduction

Cocontinuous structures formed from block copolymers have attracted much attention because of a wide range of possible technological application such as photonic crystals<sup>1,2</sup>, solar cells<sup>3,4</sup> and separations<sup>5</sup>. First observation of a cocontinuous structure was presented by Aggarwal in 1976,<sup>6</sup> where the TEM image shows a similar wagon-wheel pattern, but the nature of the structure was not discussed. A decade later, Alward *et al.* reported an ordered bicontinuous double diamond (OBDD) structure in a polystyrene-polyisoprene (PS-PI) starblock copolymer, in which they first used the phrase; “ordered bicontinuous”.<sup>7,8</sup> Around the same time, Hasegawa *et al.* reported a “tetra-pod” structure which is geometrically the same as an OBDD structure from linear PS-PI diblock copolymers,<sup>9</sup> and in 1992 Matsushita *et al.* developed an ordered tricontinuous double diamond (OTDD) structure from an ISP (I: polyisoprene, S: polystyrene, P: poly(2-vinylpyridine)) triblock terpolymer, which was the first discovery of the multiply continuous network structure from ABC triblock terpolymers.<sup>10</sup> On the other hand, two experimental<sup>11,12</sup> studies reported on the existence of new double gyroid (DG) structures in 1994, and furthermore Matsen *et al.* theoretically revealed that the double gyroid structure is more thermodynamically stable relative to the double diamond structure for simple block copolymers.<sup>13</sup> Later, Hajduk *et al.* re-examined the morphologies of PS-PI starblock copolymers previously identified as OBDD and reclassified those as OBDG by using

fully thermally-annealed samples<sup>14</sup>, whereas Suzuki *et al.* reported on an ordered tricontinuous double gyroid (OTDG) structure for an IS triblock terpolymer sample, also annealed for a long period. Considering this history as for cocontinuous network structures, these might be some possibility of structure misidentification in the past. It could be caused by low resolution of both scattering data and TEM images.

Double gyroid and double diamond structures have several structure similarities. Both structures have the triply continuous networks and are named after the periodic minimal surfaces; “Schoen G surface”<sup>15</sup> and “Schwarz D surface”<sup>16</sup>. In fact, domain interfaces of the double gyroid and double diamond structures are reasonably well represented by the two surfaces parallel to the Schoen G and Schwarz D surfaces. However, their domain interfaces of them have large deviations from the minimal surfaces with constant mean curvature because of the existence of the nodes.<sup>17,18</sup> Here it should be pointed out that gyroid networks are constructed by 3-fold nodes, whereas diamond networks possess 4-fold nodes. The node structures considerably affect the free energy of the morphology. In short, packing frustration in diamond networks is higher than that in gyroid networks because minority chains have to stretch more to fill the centers of the 4-fold nodes than that of 3-fold nodes.<sup>19,20</sup> From the standpoint of the interfacial energy, a gyroid structure is favored due to the lower distribution of mean curvature on the surface and the smaller interfacial area than those of a diamond network.<sup>18</sup>

Theoretical works presented that blends of block copolymer/homopolymer can stabilize double diamond structures,<sup>22,23</sup> where the homopolymer preferentially fills the center of 4-fold nodes to alleviate packing frustration. Furthermore, Martinez-Veracoechea *et al.*<sup>24</sup> and Dotera<sup>25</sup> suggested that a Plumber’s Nightmare phase, which includes 6-fold nodes, is predicted to be stable for AB diblock / A homopolymer and ABC triblock / A / C homopolymers blends, although the 6-fold nodes in the Plumber’s Nightmare phase cause even more higher

packing frustration than that in diamond networks. Experimentally, Takagi *et al.* have demonstrated that an OBDD structure was explicitly identified in PS-PI/PI homopolymer blends by using the scattering technique.<sup>26</sup> In addition, Chu *et al.* have found a OBDD structure in a syndiotactic polypropylene-polystyrene (sPP-PS), in which the helical segments in the sPP may reduce the packing frustration in 4-fold nodes.<sup>27</sup> Both the electron images and scattering patterns ensured the structure, which is the first real-space view of the OBDD structure. On the other hand, the OTDD structure has not yet been found in ABC/A/C blends although Suzuki *et al.* carefully investigated the phase behavior of the blend system.<sup>28</sup>

In order to obtain the DD structure, the following two energetic barriers have to be overcome; (1) packing frustration in 4-fold nodes, (2) non-constant mean curvature. Fortunately, we have already found the hints to solve the two problems in our previous works. We reported that ABC triblock terpolymer blends with different chain lengths of two end-blocks exhibit rectangular-shaped rods<sup>29,30</sup> and cylindrical morphologies with non-uniform domain sizes and shapes<sup>31</sup>. These structures reveal two important characteristics; non-uniform domain thickness and the interfaces with non-constant mean curvature, whereas domains with uniform thickness are favored to avoid packing frustration and the domain interface adopts constant mean curvature to minimize surface area for conventional block copolymers. It was concluded that localization of short and long chains within domains or unit lattices cause the specific structures to reduce the conformational entropy losses of the components on chain ends. So far, we have merely investigated the blend system with different chain length of the two end-blocks in the composition zone for the cylindrical morphologies.

In the present study, we extend our molecular design of “different chain length of two end-blocks in ABC triblock terpolymers” to the cocontinuous structure composition region and aim to look for the OTDD structure. Two asymmetric ISP triblock terpolymers were adopted, the difference in molecular weights for I chains is 6.9 and that for P chains is 4.6.

Here we estimate both the chain length differences are large enough to fill the center of the 4-fold nodes with longer block chains. Transmission electron microscopy (TEM), small angle X-ray scattering (SAXS) and TEM tomography are performed to observe the structures of well-annealed bulk films.

## 6.2 Experiments and Measurements

### 6.2.1 Molecular design

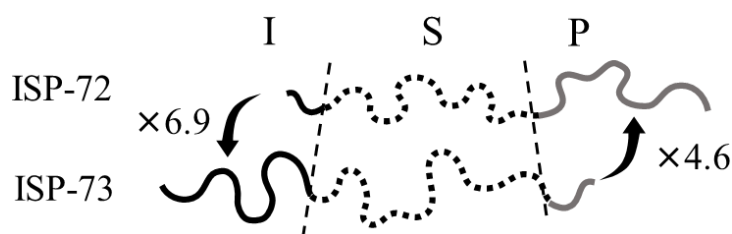


**Figure 6.1.** Schematic representation of the two ISP triblock terpolymers used in this study. Black, dashed, and gray chains represent I, S, and P, respectively.

Two kinds of poly(isoprene-*b*-styrene-*b*-2-vinylpyridine) (ISP) triblock terpolymers, ISP-72 and ISP-73, were synthesized via three-step anionic polymerizations as was mentioned in Chapter 2. SEC,  $^1\text{H-NMR}$ , MALLS and Osmometry were performed to determine their molecular informations. Table 6.1 summarizes the molecular characteristics of the two terpolymers, while their schematic illustrations are shown in Figure 6.1, in which black, dashed, and gray chains represent I, S, and P, respectively. These ISP triblocks have almost the similar total molecular weights and midblock (S) molecular weights but differ in the molecular weights of their I and P end-blocks. Binary blend samples of ISP-72 and ISP-73 are designated as Blend(X/Y), where X is the molar ratio of ISP-72 and Y is that of ISP-73. The characteristics of the binary mixtures are summarized in Table 6.2.

**Table 6.1.** Molecular characteristics of the poly(isoprene-*b*-styrene-*b*-(2-vinylpyridine))

(ISP) parent triblock terpolymers.

Sample	$M_w$ (kg/mol) <sup>a)</sup>	$M_n(I) : M_n(S) : M_n(P)$ (kg/mol) <sup>b)</sup>	$\varphi_I : \varphi_S : \varphi_P$ <sup>b)</sup>	$M_w/M_n$ <sup>c)</sup>
ISP-72	136	10.0 : 55.2 : 70.7	0.09 : 0.42 : 0.49	1.02
ISP-73	146	68.5 : 62.1 : 15.3	0.51 : 0.40 : 0.09	1.03

a) Determined by osmometry

b) Estimated from a combination of MALLS and <sup>1</sup>H NMR spectroscopy using the densities of I, S and P at room temperature ( $\rho_I$ :0.926 g/cm<sup>3</sup>,  $\rho_S$ :1.05 g/cm<sup>3</sup>,  $\rho_P$ :1.14 g/cm<sup>3</sup>).

c) Measured from a SEC chromatogram calibrated with polystyrene standards.

**Table 6.2.** Molecular characteristics of the blend samples in this study.

Sample Name	$\varphi_I : \varphi_S : \varphi_P$
Blend(9/1)	0.13:0.42:0.45
Blend(8/2)	0.18:0.42:0.40
Blend(7/3)	0.23:0.41:0.36
Blend(6/4)	0.27:0.41:0.32
Blend(5/5)	0.31:0.41:0.28
Blend(4/6)	0.35:0.41:0.24
Blend(3/7)	0.39:0.41:0.20
Blend(2/8)	0.43:0.41:0.16
Blend(1/9)	0.47:0.40:0.13

### 6.2.2 Preparation for blend samples

All sample films for the morphological observation were prepared by solvent casting from 3 wt % solution in THF, which is a nonselective solvent for all components. The solvent was slowly evaporated over 2 weeks in a Petri dish of PTFE at room temperature to achieve an equilibrium state. Subsequently, the films were dried under vacuum at room temperature for 1 day, followed by thermal annealing at 150 °C for 5 days. Detailed condition and procedure of the film preparation are mentioned in Chapter 2.

### 6.2.3 Measurements

TEM observation and SAXS measurement were performed to identify the self-assembled structures. The samples for TEM and SAXS were prepared following the previous reports.<sup>31</sup> For TEM observation, the ultrathin sections cut by an ultramicrotome were stained with osmium tetroxide ( $\text{OsO}_4$ ) vapor for 2 h at 70 °C and subsequently iodine ( $\text{I}_2$ ) vapor for 2 h at 50 °C to enhance the contrast. I component appears dark due to  $\text{OsO}_4$  and  $\text{I}_2$  is a selective staining reagent for P component. By staining with both the staining reagents, I, S and P phases appear dark, white and gray, respectively. TEM experiments were carried out using with a JEM-1400 (JEOL Co., Ltd., Japan), operated at an accelerating voltage of 120 kV. SAXS experiments were conducted using beamline BL-40B2 at Spring-8 (Hyogo, Japan) and BL-6A at Photon Factory (Tsukuba, Japan).

In order to affirmatively show the formation of the OTDD structure, TEM tomography (TEMT) was carried out using a JEM-2100Plus (JEOL Co., Ltd., Japan) operated at 200 kV. The sample for a TEMT observation was prepared in the following way. First, the small sample piece cut from the annealed bulk film was stained with  $\text{OsO}_4$  aqueous solution for 2 h at 70 °C. A rod-shaped specimen with a diameter of approximately 300 nm was fabricated by a focused-ion-beam (FIB) system. A series of a total of 165 TEM images were

taken at tilt angles ranging from  $-82^\circ$  to  $+82^\circ$  in  $1^\circ$  increment. The aligned micrographs were constructed using 3D reconstruction was given by filtered back projection method using a software, TEMography (System in Frontier, Inc., Japan).

### 6.3 Results and Discussion

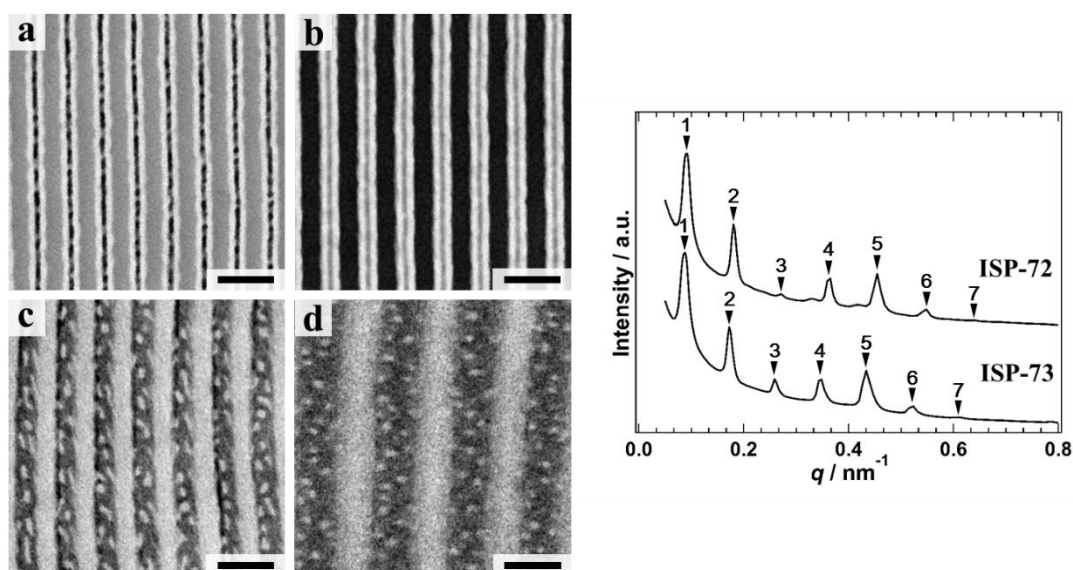


**Figure 6.2.** Representative TEM images of (a) ISP-72 and (b) ISP-73 stained with  $\text{OsO}_4/\text{I}_2$ , (c) ISP-72 stained with  $\text{OsO}_4$  and (d) ISP-73 stained with  $\text{I}_2$ . Images of (c) and (d) were taken perpendicular to lamellar surface with a slight tilt angle. All scale bars represent 100 nm. Right figure show the SAXS profiles of the parent triblocks. The profile of ISP-72 has been shifted vertically relative to that of ISP-73 for clarity. The inverted triangles point out the scattering peaks and the numbers indicate the peak positions relative to that of the first-order diffraction.

TEM micrographs of the two parent ISP triblock terpolymers are presented in Figure 6.2. Both the parent polymers create perforated lamellar structures. For ISP-72, perforated layers are composed of I component, while in ISP-73, P component forms a perforated phase, as shown in Figure 6.2 (c) and (d). Although the perforated lamellar structure is often believed

to be a metastable phase structure,<sup>32,33</sup> in the present work, they must be the thermal equilibrium structures because of the long solvent casting/annealing process and reproducibility. The morphologies are further confirmed by SAXS as shown in Figure 6.2. The scattering peaks are observed at integer values of the position of first order scattering maximum,  $q_m$ , indicating both the parent triblocks form alternative lamellar microdomains. The d-spacings of ISP-72 and ISP-73 are estimated to be 69 and 71 nm, respectively, which are consistent with the results of the real space images. The periodicity of the perforated phase generally can be identified by the scattering pattern, however, in this case, the peaks associated with the perforated phase are not obviously observed. This may be due to the poor-ordered perforated phase.

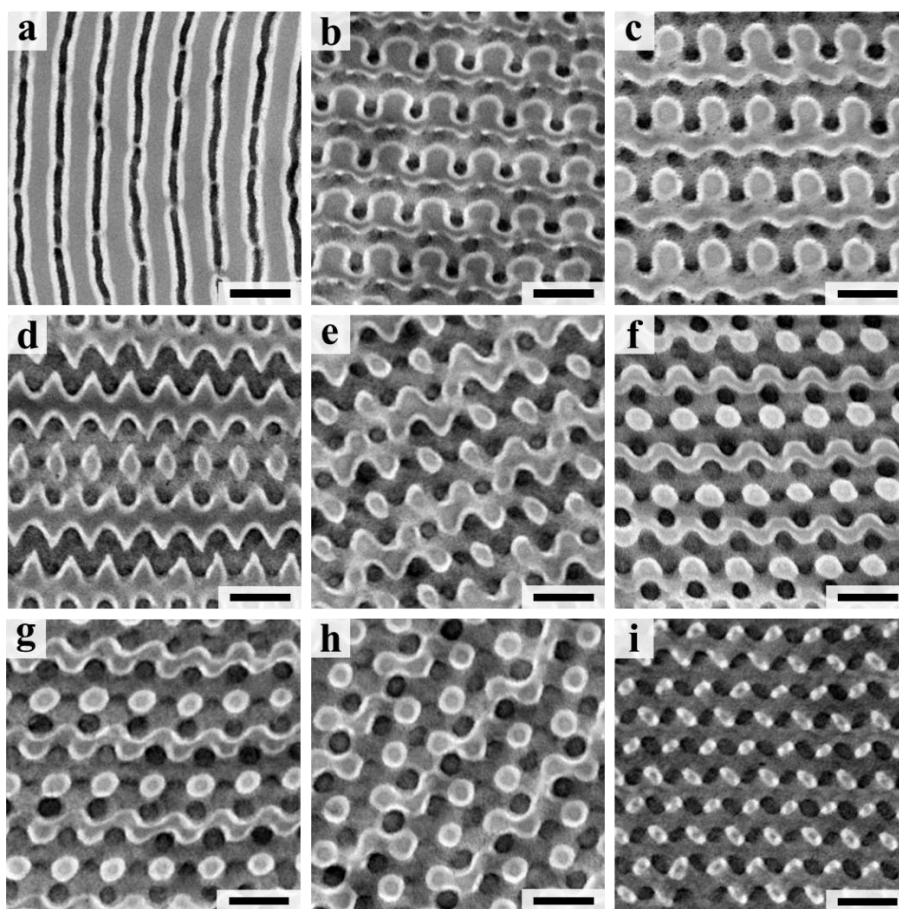


**Figure 6.3.** TEM images of the blend samples. (a) Blend(9/1), (b) Blend(8/2), (c) Blend(7/3),

## Chapter 6

(d) Blend(6/4), (e) Blend(5/5), (f) Blend(4/6), (g) Blend(3/7), (h) Blend(2/8) and (i) Blend(1/9).

All scale bars represent 100 nm.

TEM images of all blend samples are summarized in Figure 6.3. As a general observation, macrophase separation does not occur in any blend samples and the majority of the blends exhibit cocontinuous structures. In the case of Blend(9/1), the perforated lamellae phase was obtained, where I domain was thicker than that of ISP-72. A tilted TEM image of Blend(9/1) in Figure 6.4 reveals that the number of perforations reduces from ISP- $\alpha$  because of the higher volume fraction of I component than that of ISP-72. On the other hand, for other blend samples, typical continuous structure patterns, “wagon wheel” and “double wave”, were observed in their TEM images. However, it is quite hard to distinguish between OTDD and OTDG by only the two-dimensional (2D) micrographs because some of the 2D projections of the OTDD are similar to those of the OTDG, depending on the film thickness. Consequently, TEM simulation was performed to identify the structures. The TEM simulation was carried out using Mathematica (ver. 10). The Mathematica codes are presented in Appendix I. The calculation was carried out on the assumption that the cocontinuous structures possess the tricontinuous state in which I and P domains each form a diamond or a gyroid lattice embedded in an S matrix and that the interfaces of I/S and S/P are created by the parallel shift of the three-dimensional periodic minimal surfaces.<sup>34</sup> In order to perform the TEM simulation, four parameters are considered; (1) TEM contrasts, (2) volume fractions of three components, (3) the direction of projection, (4) thickness of a ultrathin film. The TEM contrasts meet the same situation as the TEM images stained with OsO<sub>4</sub>/I<sub>2</sub>; I (black) > P (gray) > S (white). The exact volume fractions of each sample, listed in Table 6.2, are employed for the calculation. The other two parameters are adjusted as needed. Appendix II summarizes the computer-generated 2D projections from various directions of projection with constant film thickness and volume

fractions to clarify the differences of TEM images between OTDG and OTDD.

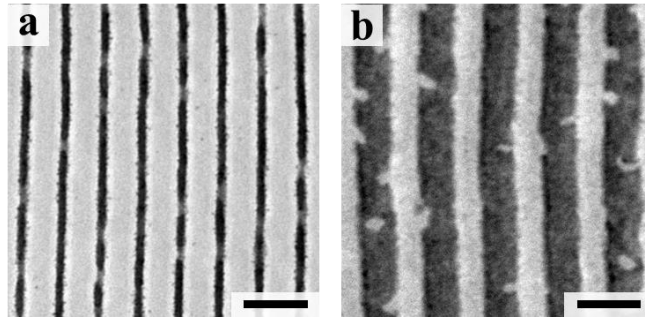


**Figure 6.4.** TEM images of Blend(9/1) stained with OsO<sub>4</sub>. Image of (b) was shot perpendicular to lamellar surface with a slight tilt. All scale bars represent 100 nm.

Here, let me compare the TEM simulation results with the TEM images for each blend sample in Figure 6.5 ~ 6.12. Inset capitals and numbers in simulation results express the type of cocontinuous structure and the direction of projection: e.g., G(122) indicates OTDG from the projection of (122) direction and D(112) represents OTDD from the projection of (112) direction.

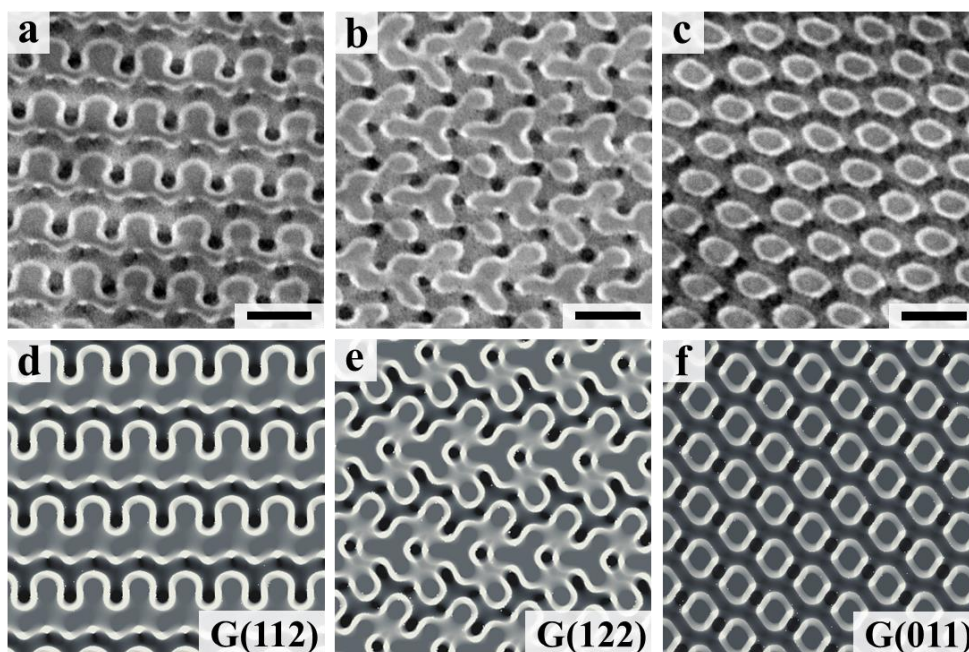


**Figure 6.5.** Comparison of TEM images (a)-(c) and computer-generated images (d)-(f) of Blend(8/2). The inset capitals in TEM simulations express the type of cocontinuous structure, i.e., G; Gyroid, D; Diamond. The numbers in the insets represent the direction of the simulated projection. All scale bars represent 100 nm.

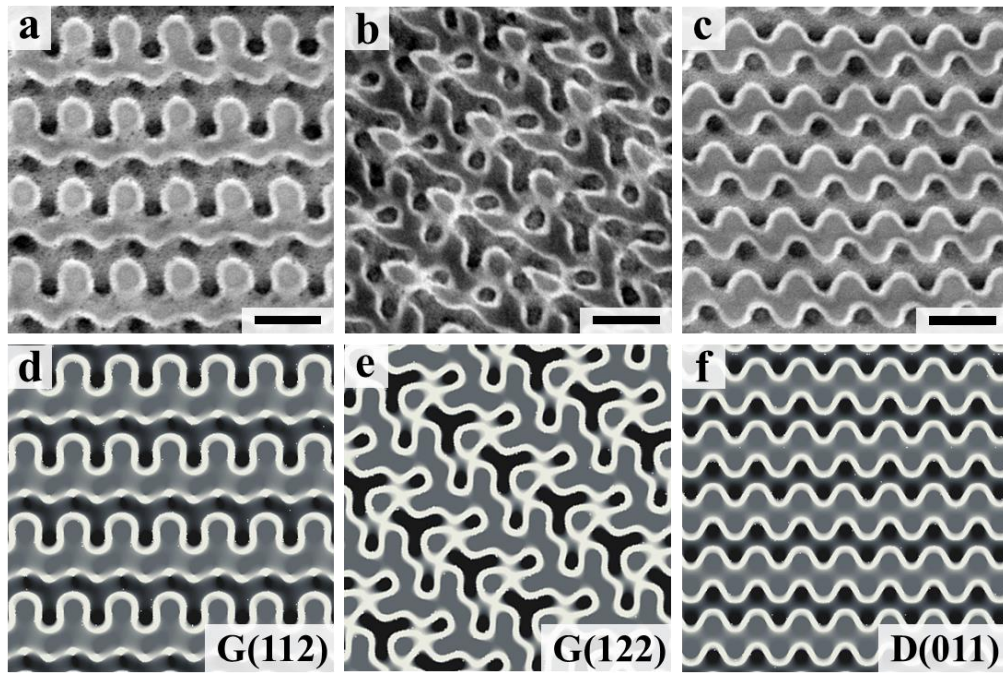


**Figure 6.6.** Comparison of TEM images (a)-(c) and computer-generated images (d)-(f) of Blend(7/3). The inset indicates the type of continuous structure and the direction of the simulated projection. All scale bars represent 100 nm.

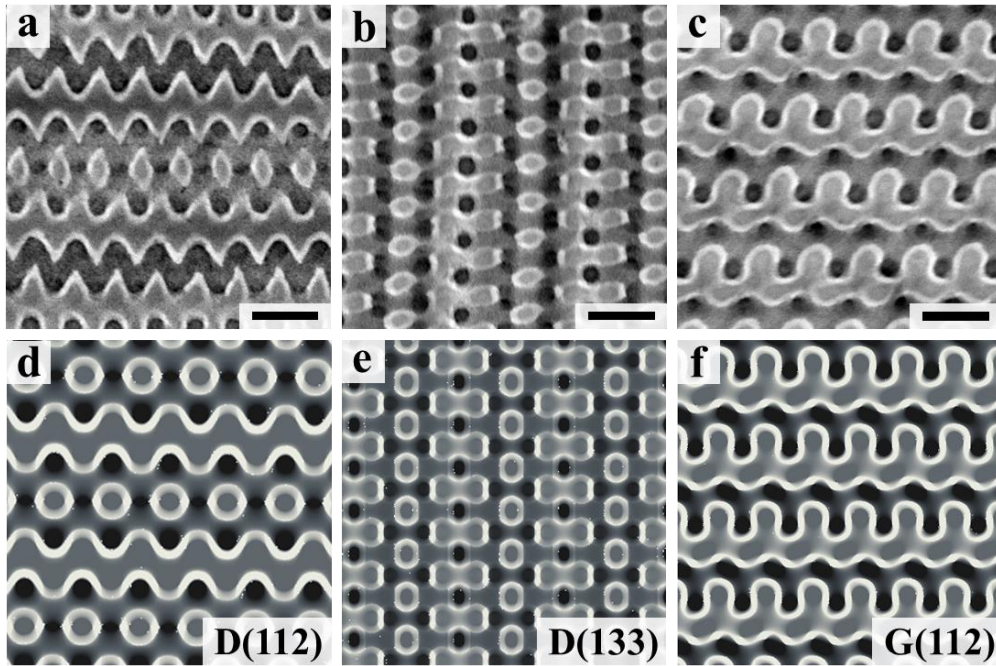


**Figure 6.7.** Comparison of TEM images (a)-(c) and computer-generated images (d)-(f) of Blend(6/4). The inset indicates the type of continuous structure and the direction of the simulated projection. All scale bars represent 100 nm.

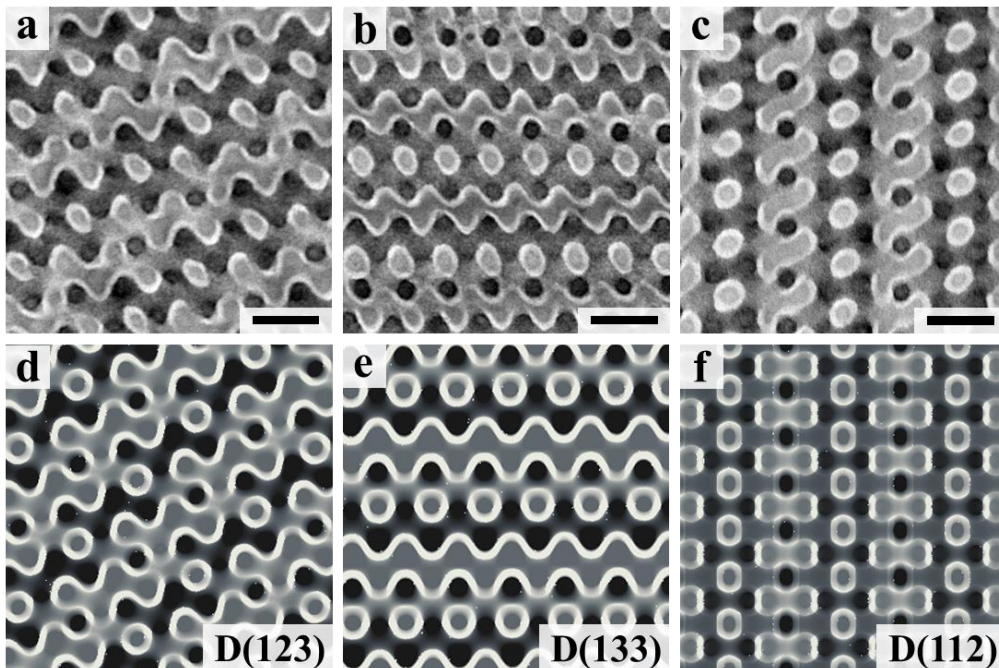


**Figure 6.8.** Comparison of TEM images (a)-(c) and computer-generated images (d)-(f) of Blend(5/5). The inset indicates the type of continuous structure and the direction of the simulated projection. All scale bars represent 100 nm.

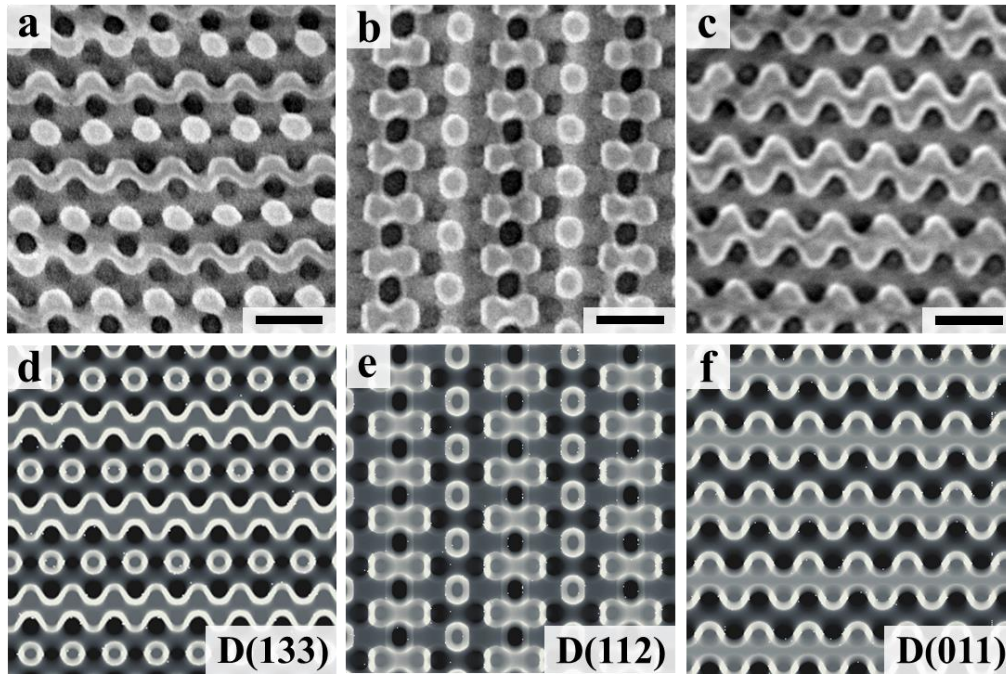


**Figure 6.9.** Comparison of TEM images (a)-(c) and computer-generated images (d)-(f) of Blend(4/6). The inset indicates the type of continuous structure and the direction of the simulated projection. All scale bars represent 100 nm.

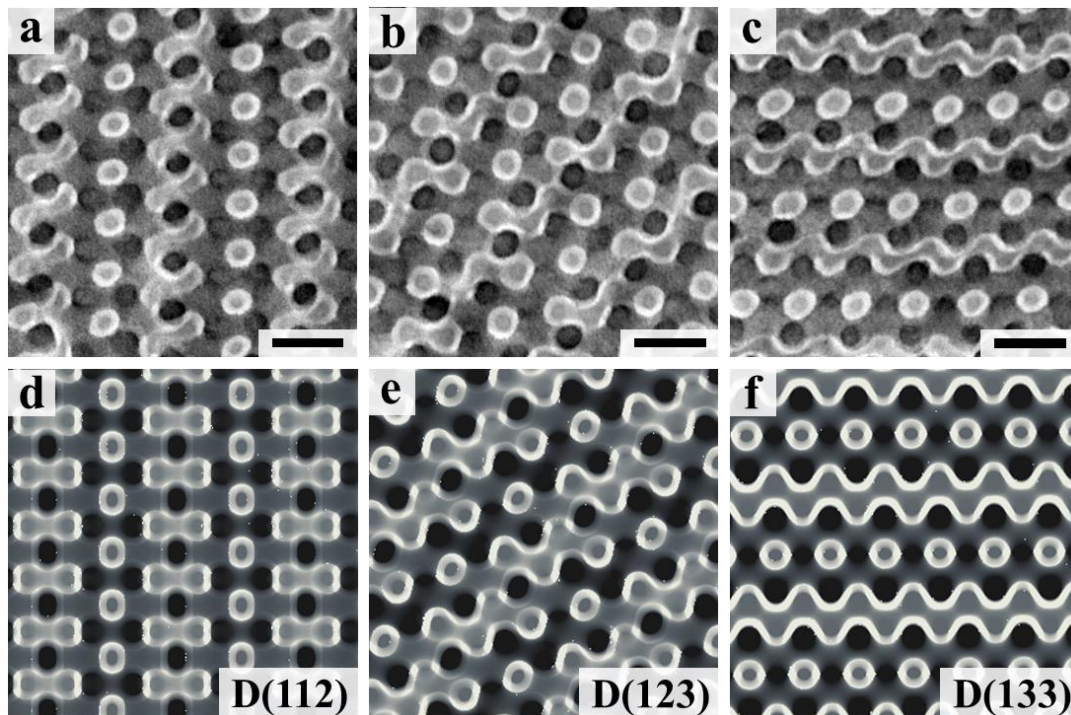


**Figure 6.10.** Comparison of TEM images (a)-(c) and computer-generated images (d)-(f) of Blend(3/7). The inset indicates the type of continuous structure and the direction of the simulated projection. All scale bars represent 100 nm.

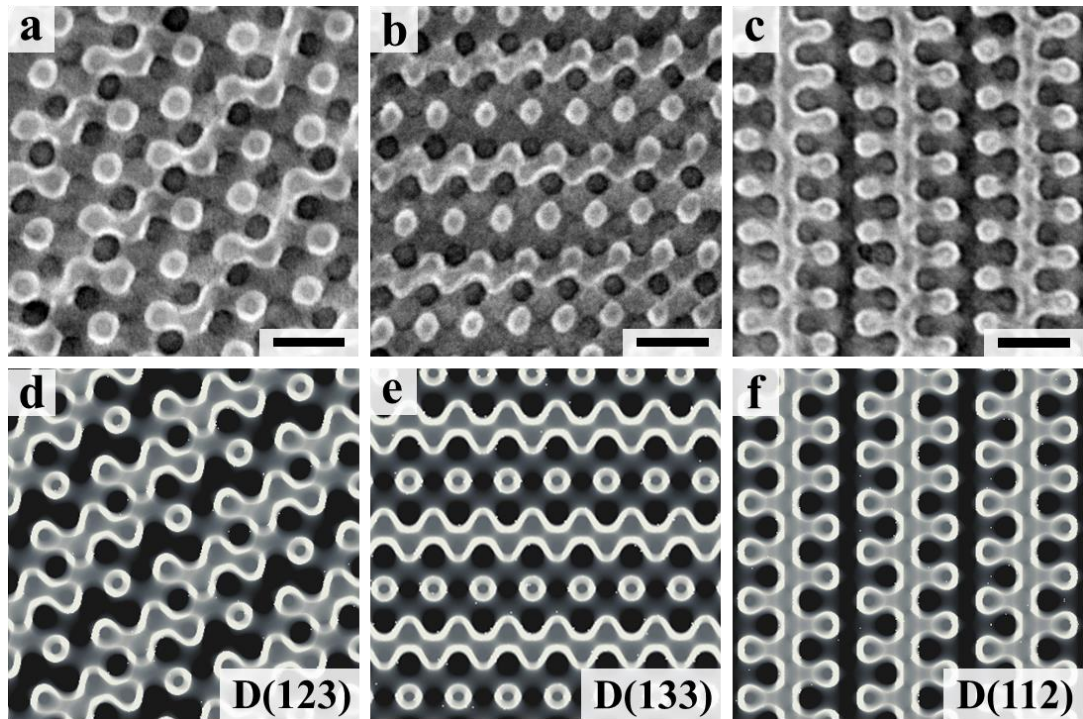


**Figure 6.11.** Comparison of TEM images (a)-(c) and computer-generated images (d)-(f) of Blend(2/8). The inset indicates the type of continuous structure and the direction of the simulated projection. All scale bars represent 100 nm.

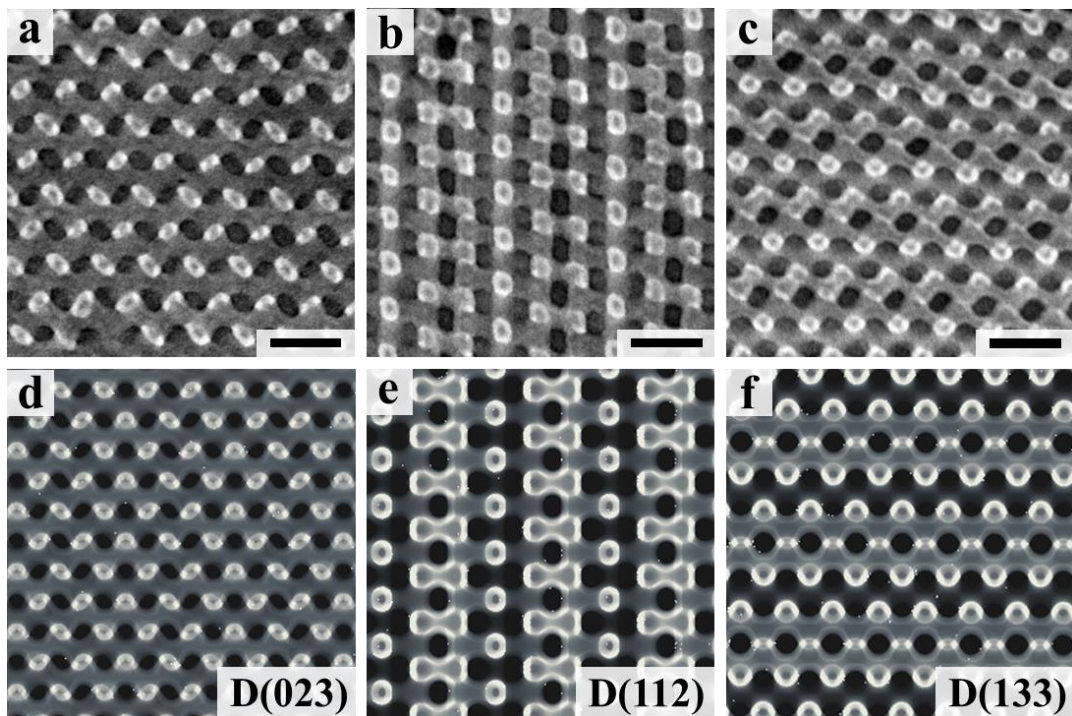


**Figure 6.12.** Comparison of TEM images (a)-(c) and computer-generated images (d)-(f) of Blend(1/9). The inset indicates the type of continuous structure and the direction of the simulated projection. All scale bars represent 100 nm.

## Chapter 6

Figure 6.5 ~ 6.12 show the comparison results between the TEM images with the TEM simulations for each sample. According to the comparison, Blend(8/2) and Blend(7/3) exhibit the OTDG structure, and the OTDD structures are found from Blend(6/4) to Blend(1/9). However, Blend(7/3) partially forms the OTDD and the OTDG is partly developed in Blend(6/4), suggesting that Blend(7/3) and Blend(6/4) are a transition region from OTDG to OTDD. All blend samples were prepared at least three times in the same way (solvent casting over 2 weeks and thermal annealing at 150 °C for 3 days) to confirm the reproducibility. TEM and SAXS data of the blend samples were reproducibly obtained with the exception of Blend(7/3) and (6/4) that are in the transition region. These results ensure that OTDD structures are the thermodynamically stable phase.

It should be stressed that the OTDD structure is found at a wide range of volume fractions:  $\phi_I:\phi_S:\phi_P=0.31:0.41:0.28 \sim 0.47/0.40/0.13$ . The blend samples keep the constant S volume fractions but have asymmetric volume fractions of end blocks as varying the blend ratios. In general, tricontinuous structures such as double gyroid and double diamond are believed to be stable when the alternative networks have the symmetric composition. Naturally, it is never predicted theoretically and observe experimentally that double gyroid and diamond structures stabilize in ABC triblock terpolymers with asymmetric end-block compositions. Contrary to the conventional wisdom, the OTDD was found from Blend(1/9), the volume fraction of which is  $\phi_I/\phi_S/\phi_P = 0.47/0.40/0.13$  and interestingly the majority I domain and the minority P domain alternate on a diamond lattice, although the volume fraction of I component is higher than that that S component, which is considered as a matrix phase in the diamond structure.

TEM experiment is a useful and powerful tool to identify the domain shapes and arrangement, but only obtain the local area of the structures. SAXS measurement can evaluate the averaged and long area because of the large beam size. Combination TEM with SAXS can

provide an explicit evidence. Azimuthally-integrated synchrotron SAXS profiles of the blends samples are shown in Figure 6.13. The sequence of peaks are pointed out by inverted triangles.

The relative peak positions and the  $q$  values of the primary peaks are listed in Table 6.3.

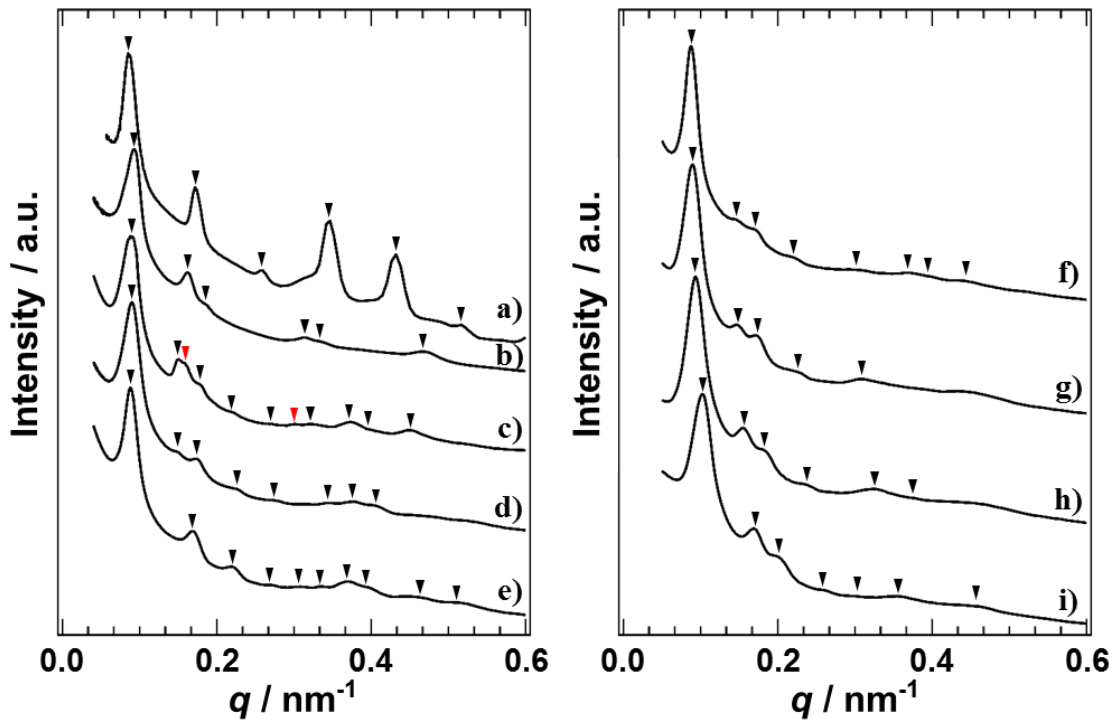


**Figure 6.13.** 1D synchrotron SAXS profiles of blend samples: (a) Blend(9/1), (b) Blend(8/2), (c) Blend(7/3), (d) Blend(6/4), (e) Blend(5/5), (f) Blend(4/6), (g) Blend(3/7), (h) Blend(2/8) and (i) Blend(1/9). The sequence of peaks are pointed out by inverted triangles. The red inverted triangles on the plot of Blend(3/7) is not followed by the relative intensity rule of OTDG.

**Table 6.3.** Observed Relative Peak Positions of Blend Samples.

Sample	$q^*[\text{nm}^{-1}]$	1 <sup>st</sup>	2 <sup>nd</sup>	3 <sup>rd</sup>	4 <sup>th</sup>	5 <sup>th</sup>	6 <sup>th</sup>	7 <sup>th</sup>	8 <sup>th</sup>	9 <sup>th</sup>	10 <sup>th</sup>	11 <sup>th</sup>
Blend(9/1)	0.085	1	2	3	4	5	6					
Blend(8/2)	0.093	$\sqrt{2}$	$\sqrt{6}$	$\sqrt{8}$	$\sqrt{22}$	$\sqrt{26}$	$\sqrt{50}$					
Blend(7/3)	0.088	$\sqrt{2}$	$\sqrt{6}$	-	$\sqrt{8}$	$\sqrt{12}$	$\sqrt{20}$	-	$\sqrt{26}$	$\sqrt{36}$	$\sqrt{38}$	$\sqrt{50}$
Blend(6/4)	0.090	$\sqrt{3}$	$\sqrt{8}$	$\sqrt{11}$	$\sqrt{19}$	$\sqrt{27}$	$\sqrt{43}$	$\sqrt{51}$	$\sqrt{59}$			
Blend(5/5)	0.088	$\sqrt{3}$	$\sqrt{11}$	$\sqrt{19}$	$\sqrt{27}$	$\sqrt{36}$	$\sqrt{43}$	$\sqrt{51}$	$\sqrt{59}$	$\sqrt{83}$		
Blend(4/6)	0.088	$\sqrt{3}$	$\sqrt{8}$	$\sqrt{11}$	$\sqrt{19}$	$\sqrt{36}$	$\sqrt{43}$	$\sqrt{59}$	$\sqrt{75}$			
Blend(3/7)	0.089	$\sqrt{3}$	$\sqrt{8}$	$\sqrt{11}$	$\sqrt{19}$	$\sqrt{36}$						
Blend(2/8)	0.093	$\sqrt{3}$	$\sqrt{8}$	$\sqrt{11}$	$\sqrt{19}$	$\sqrt{36}$	$\sqrt{48}$					
Blend(1/9)	0.103	$\sqrt{3}$	$\sqrt{8}$	$\sqrt{11}$	$\sqrt{19}$	$\sqrt{27}$	$\sqrt{36}$	$\sqrt{59}$				

$q^*$ :  $q$  value of the primary peak

All the SAXS profiles show the higher-ordered diffraction peaks. The structure assignment and unit lattice size of each sample determined by the SAXS profile are summarized in Table 6.4. The relative peak ratio of Blend(9/1) reveals a lamellar structure, whose domain spacing is estimated to be 73.7 nm from the primary peak ( $q^*$ ). The domain spacing observed from the TEM image in Figure 6.3 (a) is qualitatively consistent with that estimated from the SAXS. The domain distance is slightly increased by the small addition of ISP-73 with the higher total molecular weight. For Blend(8/2) and Blend(7/3), the relative peak positions at  $\sqrt{2}$ ,  $\sqrt{6}$ ,  $\sqrt{8}$  reflections correspond well to the representative relative peak positions of OTDG, suggesting that both the samples form OTDG. Look at the SAXS pattern of Blend(7/3) carefully. Some peaks pointed out by inverted red triangles are not followed by the rule of OTDG. That may be due to the partially-observed OTDD structure. The lattice

constant  $a$  of OTDG is estimated from  $a_{cubic} = \sqrt{\frac{d^2}{h^2+k^2+l^2}}$ , ( $d = \frac{2\pi}{q_{hkl}}$ ). The  $a$ s of Blend (8/2) and Blend(7/3) are 95.5 nm and 101 nm, respectively. From Blend(6/4) to Blend(1/9), the scattering data show reflections at relative positions of  $\sqrt{3}$ , ( $\sqrt{8}$ ),  $\sqrt{11}$ ,  $\sqrt{19}$ , ... The presence of a reflection at this relative position suggests the OTDD structures are obtained from Blend(6/4) to Blend(1/9). The estimated lattice constants from the primary peak ( $q_{111}$ ) are 121 nm, 124 nm, 124 nm, 122 nm, 117 nm and 106 nm for Blend(6/4) to Blend(1/9), respectively, which are in good agreement with the real space results. The relative intensities of the scattering peaks changes as varying the blend ratios even though all the samples exhibit an OTDD structure. This will lead us further into consideration of the SAXS pattern shown in Figure 6.13. It is well-known that the difference in the volume fractions (phase thickness) makes a significant contribution to the scattering intensity. Hence, the calculation of scattering intensities of OTDG and OTDD was conducted considering the volume fractions and the lattice constants. See the Appendix III for the detail of the formulation.

**Table 6.4.** Observed Relative Peak Positions of Blend Samples.

Sample	9/1	8/2	7/3	6/4	5/5	4/6	3/7	2/8	1/9
Structure	PL	DG	DG/DD	DD/DG	DD	DD	DD	DD	DD
Lattice [nm]	73.7	95.5	101	121	124	124	122	117	106

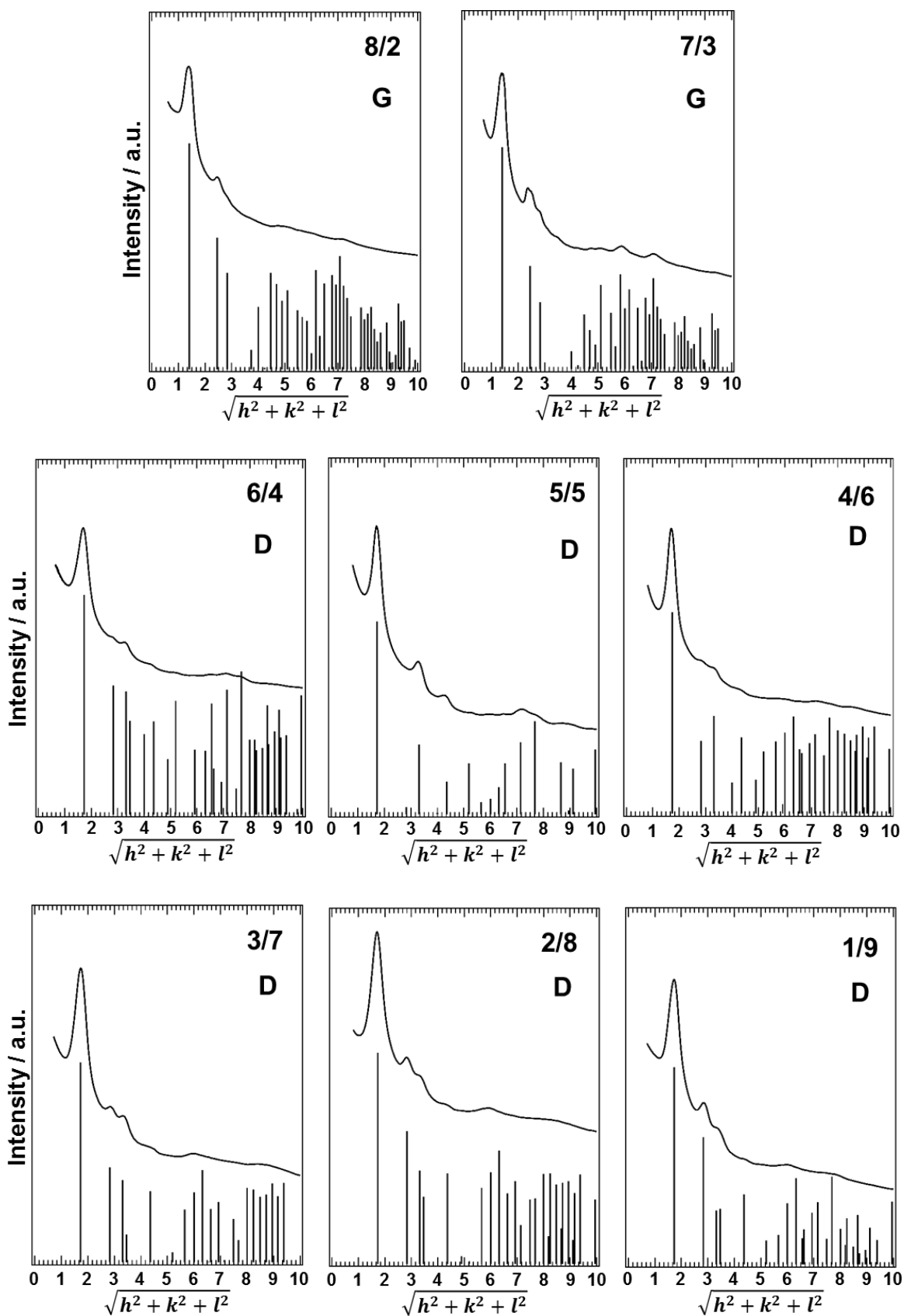
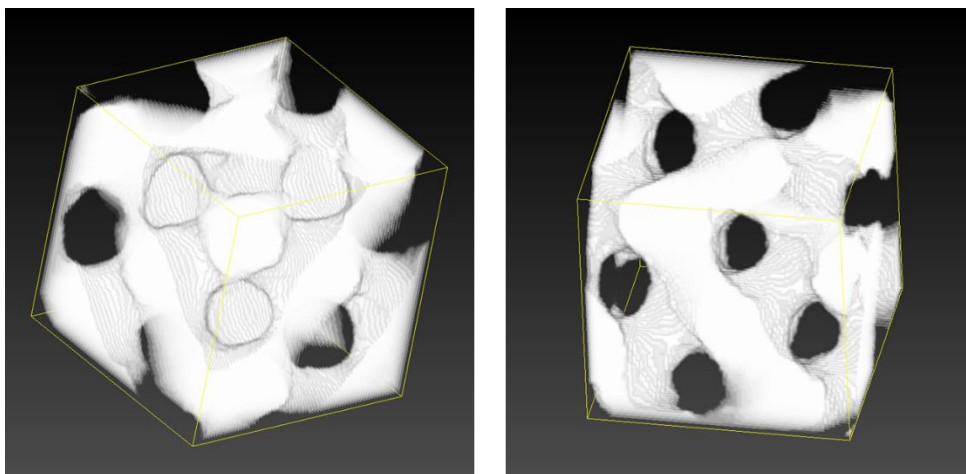


Figure 6.14. SAXS profiles of the blend samples and the intensity calculation results for each

$\sqrt{h^2 + k^2 + l^2}$ , where h, k and l denote Miller index. The inset numbers and characters express the sample name and the type of cocontinuous structure (G: OTDG, D: OTDD), respectively. The vertical bars represent the relative peak intensities calculated in Appendix III.

Figure 6.14 shows the comparison between the experimental SAXS profiles and the calculated results. The calculated intensities are taken into account the degree of duplication for the reflections. For the experimental SAXS patterns, the q-value is converted into  $\sqrt{h^2 + k^2 + l^2}$  for clarity. All the calculation results are qualitatively consistent with the corresponding experimental SAXS patterns.

The TEM images coupled with the SAXS results provide a solid evidence for the existence of an OTDD structure in the binary blends of ABC triblock terpolymers with different chain length of two-end blocks. However, these characterization techniques cannot provide the information of a tetrapod connection, which is a primary feature of a diamond structure. Consequently, TEM tomography was conducted to visualize the tetrapod connections. The tomography was carried out for Blend(1/9) that has the thickest I phase.



**Figure 6.15** 3D TEM images of the OTDD structure of Blend(1/9) where the highlighted microdomain is composed of I component.

Figure 6.15 shows the representative 3D images of Blend(1/9), where the microdomains are composed of I component. The images clearly observe the tetrapod connections that are interconnected with  $Fd\bar{3}m$  symmetry, revealing the double diamond structure. Furthermore, the inclined angle between two adjacent tetrapods is close to  $109.5^\circ$ , which agrees well with a model of a diamond structure. The TEM tomography images strongly corroborate the existence of OTDD in the present blend system.

OTDD has never been considered as an equilibrium structure for the conventional ABC triblock terpolymers because of the high packing frustration and the non-constant mean curvature, whereas OTDG is a well-known thermodynamical stable structure. Here, let me discuss why OTDD was observed in ISP triblock terpolymers with different chain length of the two end-blocks. In this blend system, the alternative diamond networks are composed of long and short block chains even when the volume fractions of I and P are highly asymmetric. As suggested in our previous works, the coexistence of long and short block chains within the same domains induces the chain localization of junction point at the domain interface to relieve the conformational entropy loss by mixing, resulting in non-constant mean curvature. The schematic representation of the possible chain localization at the 4-fold node is shown in Figure 6.16. The 4-fold pods contain a high fraction of the long chains, and the connected domains between the adjacent tetrapods are mainly filled with the short chains. The localization can release the entropic cost associated with chain stretching for short chains since the long chains compensate the further chain stretching of the shorter chains to reach the center of the tetrapods.

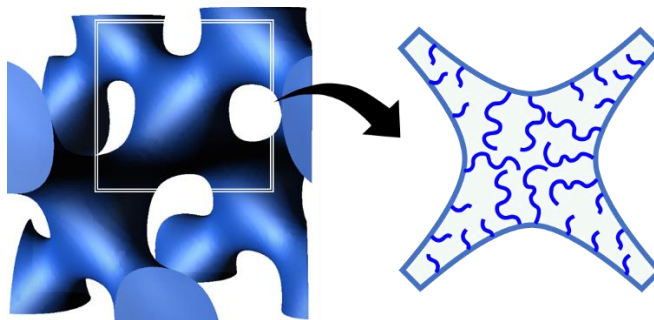


**Figure 6.15** Schematic illustration of possible chain orientation within tetrapods.

Furthermore, from the standpoint of the interfacial curvature, the chain localization leads to the stabilization of diamond network with non-CMC. Diamond networks can be divided into two parts; a tetrapod and a joint. The joint part connecting one tetrapod to another has a similar nature with cylinder, interpreting that the interfacial curvature of the joint part is higher than that of the tetrapod. A part of the tetrapod show nearly flat surface. The localization of long chains at the tetrapods naturally allows the flat surface and the existence of short chains within the joints induces curved interface.

#### 6.4 Conclusions

In this study, we have adopted the “different chain length” to the cocontinuous structure region. By blending the two ISP triblock terpolymers with different chain lengths of the two end-blocks, OTDD structure was obtained at wide range of compositions. Our TEM, SAXS and TEM tomography results all corroborate the existence of OTDD in the present blend system. The different chain length may help to alleviate the free energy penalty of interfacial tension and stretching energy. This is the first report to provide the solid evidence of the OTDD structure.

## 6.5 Appendix

### Appendix I

#### Mathematical Code for the TEM simulation of tricontinuous double gyroid structure.

```
t:=ArcCos[l/(h2+k2+l2)1/2];
```

```
u:=ArcCos[h/(h2+k2+l2)1/2];
```

```
X[x_,y_,z_]:=Simplify[(Cos[t]Cos[u])x+(-Sin[u])y+(Cos[u]Sin[t])z];
```

```
Y[x_,y_,z_]:=Simplify[(Cos[t]Sin[u])x+(Cos[u])y+(Sin[u]Sin[t])z];
```

```
Z[x_,y_,z_]:=Simplify[(-Sin[t])x+(0)y+(Cos[t])z];
```

```
f[x_,y_,z_]:=Sin[X[x,y,z]]Cos[Y[x,y,z]]+Sin[Y[x,y,z]]Cos[Z[x,y,z]]+Sin[Z[x,y,z]]Cos[X[x,y,z]]-n1;
```

```
g[x_,y_,z_]:=Sin[X[-x,-y,-z]]Cos[Y[-x,-y,-z]]+Sin[Y[-x,-y,-z]]Cos[Z[-x,-y,-z]]+Sin[Z[-x,-y,-z]]Cos[X[-x,-y,-z]]-n2;
```

```
a[x_,y_,z_]:= (Sign[f[x,y,z]]+1)/2;
```

```
b[x_,y_,z_]:= (Sign[g[x,y,z]]+1)/2;
```

```
m[x_,y_,z_]:= (Sign[f[x,y,z]g[x,y,z]]+1)/2;
```

```
A[x_,y_]:=Sum[a[x,y,z]/100,{z,w,w+d,d/(99)}];
```

```
B[x_,y_]:=Sum[b[x,y,z]/100,{z,w,w+d,d/(99)}];
```

```
M[x_,y_]:=Sum[m[x,y,z]/100,{z,w,w+d,d/(99)}];
```

```
H[x_,y_]:=Exp[-1.0 A[x,y]-0.5B[x,y]-0.1M[x,y]];
```

(\*h,k,l: miller index, d: thickness, w: start point, n1, n2: the position of the interface \*)

```
h:=1;
```

```
k:=0;
```

```
l:=0;
```

```
d:= √3π/8;
```

```
w:= √3 π/8;
```

```
n1=0.623;
```

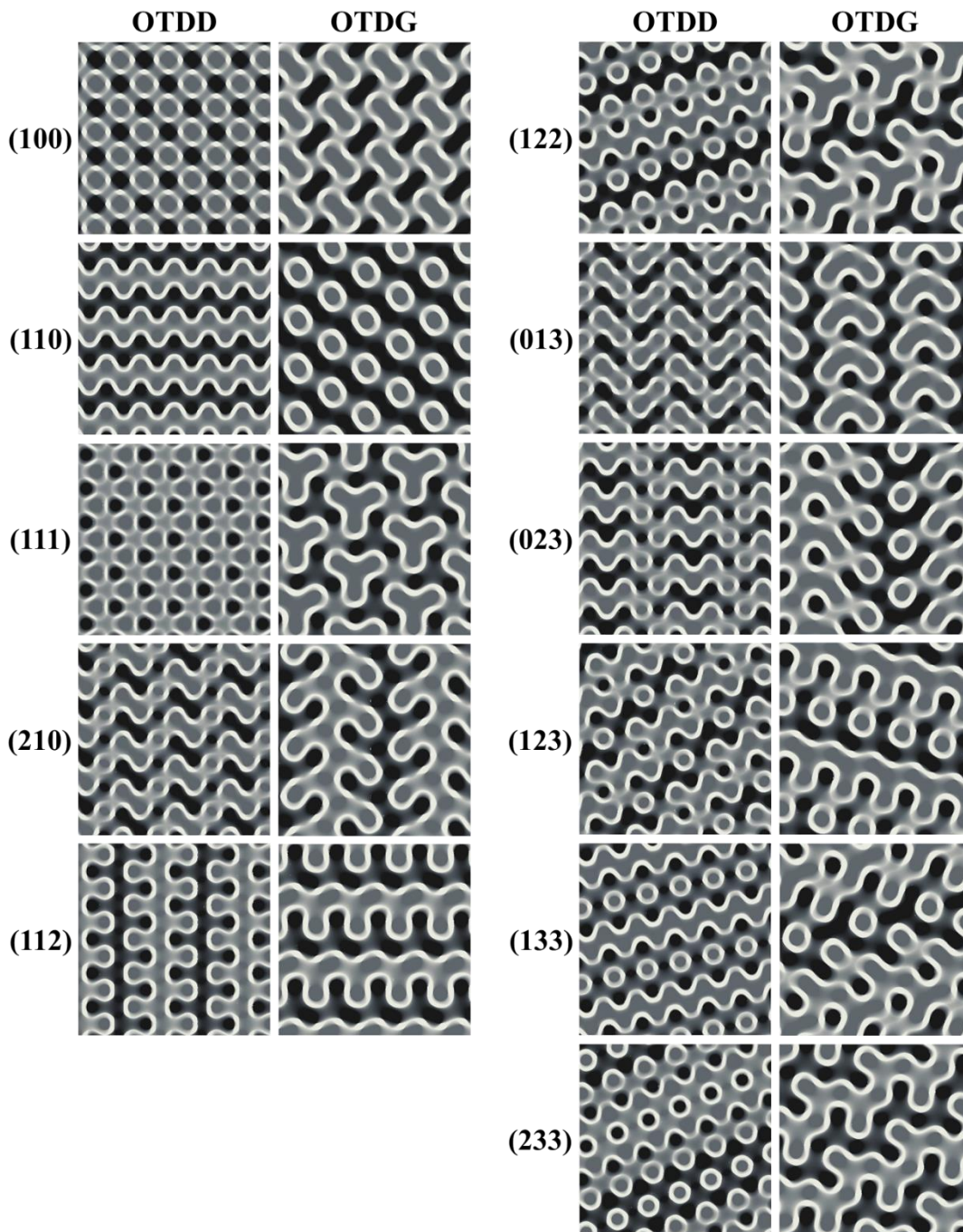
```
n2=0.623;
```

```
Gra=ContourPlot[Evaluate[H[x,y]],{x,-π,π},{y,-π,π},ContourStyle->None,Contours->50,PlotPoints->80,ColorFunction->ColorData["GrayTones"]];
```

```
image=Show[Gra,ImageSize->Full]
```

## Appendix II

Appendix II compares 2D projections of OTDD and OTDG. The projections were generated by the TEM simulations as described in Appendix I. The calculation conditions are given as follows; (1) volume fraction:  $\varphi_A:\varphi_B:\varphi_C=0.3:0.4:0.3$  ( $n_1=n_2=0.623$ ), (2) contrast: A(black) > C(dark) > B(white), (3) start point, thickness:  $w=0$ ,  $d=2\sqrt{3}\pi/8$ . The direction of projection is denoted on the left of each image.



**Appendix III****Mathematical Code for the intensity calculation of double gyroid structure.**

```

RhoGyroid[x_,y_,z_]:=Module[{r,X,Y,Z,g,rho},
  r1=0.623>(*the position of the I/S interface*)
  r2=0.623>(* the position of the S/P interface *)
  X=x*2Pi;
  Y=y*2Pi;
  Z=z*2Pi;
  g=Sin[X] Cos[Y]+Sin[Y] Cos[Z]+Sin[Z] Cos[X];
  rho=0.565; (*electron density of styrene*)
  rho=If[g >r1,0.512(*isoprene*),
    If[g<(-r2),0.608(*pyridine*),0.565(*styrene*)]];
  Return[rho];
];
n=20;
GyIntS[h_,k_,l_]:=
Module[{s,X,Y,Z,x,y,z},
  s=0;
  For[X=0,X<n,X++,
    For[Y=0,Y<n,Y++,
      For[Z=0,Z<n,Z++,
        x=X/n+1/(2 n);
        y=Y/n+1/(2 n);
        z=Z/n+1/(2 n);
        s=s+RhoGyroid[x,y,z]*Sin[2 Pi (h x+k y +l z)];
      ]]];
  Return[s];
];
GyIntC[h_,k_,l_]:=
Module[{c,X,Y,Z,x,y,z},
  c=0;
  For[X=0,X<n,X++,
    For[Y=0,Y<n,Y++,
      For[Z=0,Z<n,Z++,
        x=X/n+1/(2 n);
        y=Y/n+1/(2 n);

```



## 6.6 References

1. Edrington, A. C.; Urbas, A. M.; DeRege, P.; Chen, C. X.; Swager, T. M.; Hadjichristidis, N.; Xenidou, M.; Fetters, L. J.; Joannopoulos, J. D.; Fink, Y.; Thomas, E. L. Polymer-Based Photonic Crystals. *Adv. Mater.* **2001**, 13, 421-425.
2. Dolan, J. A.; Wilts, B. D.; Vignolini, S.; Baumberg, J. J.; Steiner, U.; Wilkinson, T. D. Optical Properties of Gyroid Structured Materials From Photonic Crystals to Metamaterials. *Adv. Optical Mater.* **2015**, 3, 12-32.
3. Crossland, E. J. W.; Kamperman, M.; Nedelcu, M.; Ducati, C.; Wiesner, U.; Smilgies, D.-M.; Toombes, G. E. S.; Hillmyer, M. A.; Ludwigs, S.; Steiner, U.; Snaith, H. J. A Bicontinuous Double Gyroid Hybrid Solar Cell. *Nano Lett.* **2009**, 9, 2807-2812.
4. Docampo, P.; Stefik, M.; Guldin, S.; Gunning, R.; Yufa, N. A.; Cai, N.; Wang, P.; Steiner, U.; Snaith, H. J. Triblock-Terpolymer-Directed Self-Assembly of Mesoporous TiO<sub>2</sub>: High-Performance Photoanodes for Solid-State Dye-Sensitized Solar Cells. *Adv. Energy Mater.* **2012**, 2, 676-682.
5. Schacher, F. H.; Ruper, P. A.; Manners, I. Functional Block Copolymers: Nanostructured Materials with Emerging Applications. *Angew. Chem. Int. Ed.* **2012**, 51, 7898-7921.
6. Aggarwal, S. L. Structure and properties of block polymers and multiphase polymer systems: an overview of present status and future potential. *Polymer* **1976**, 17, 938-956.
7. Alward, D.B.; Kinning, D. J.; Thomas, E. L.; Fetters, L. J. Effect of Arm Number and Arm Molecular Weight on the Solid-State Morphology of Poly(styrene-isoprene) Star Block Copolymers. *Macromolecules* **1986**, 19, 215-224.
8. Thomas, E. L.; Alward, D. B.; Kinning, D. J.; Martin, D. C. Ordered Bicontinuous Double-Diamond Structure of Star Block Copolymers: A New Equilibrium Microdomain Morphology. *Macromolecules* **1986**, 19, 2197-2202.
9. Hasegawa, H.; Tanaka, H.; Yamasaki, K.; Hashimoto, T., Bicontinuous Microdomain Morphology of Block Copolymers. 1. Tetrapod-Network Structure of Polystyrene-Polyisoprene Diblock polymers. *Macromolecules* **1987**, 20, 1651-1662.
10. Mogi, Y.; Kotsuji, H.; Kaneko, Y.; Mori, K.; Matsushita, Y.; Noda, I. Preparation and Morphology of Triblock Copolymers of the ABC Type. *Macromolecules* **1992**, 25, 5408-5411.
11. Hajduk, D. A.; Harper, P. E.; Gruner, S. M.; Honeker, C. C.; Kim, G.; Thomas, E. L.; Fetters, L. J. The Gyroid A New Equilibrium Morphology in Weakly Segregated Diblock Copolymers. *Macromolecules* **1994**, 27, 4063-4075.
12. Schulz, M. F.; Bates, F. S.; Almdal, K.; Mortensen, K. Epitaxial Relationship for Hexagonal-to-Cubic Phase Transition in a Block Copolymer Mixture. *Phys. Rev. Lett.* **1994**, 73, 86-89.
13. Matsen, M. W.; Schick, M. Microphase Separation in Starblock Copolymer Melts. *Macromolecules* **1994**, 27, 6761-6767.
14. Hajduk, D. A.; Harper, P. E.; Gruner, S. M.; Honeker, C. C.; Kim, G.; Thomas, E. L.; Fetters, L. J. A Reevaluation of Bicontinuous Cubic Phases in Starblock Copolymers. *Macromolecules* **1995**, 28,

- 2570-2573.
15. Schoen, A. H. Infinite Periodic Minimal Surfaces without Self-Intersections. *NASA TN D-5541* **1970**.
  16. Gandy, P. J. F.; Cvijovic, D.; Mackay, A. L.; Klinowski, J. Exact computation of the triply periodic D ('diamond') minimal surface. *Chem. Phys. Lett.* **1999**, 314, 543-551.
  17. Jinnai, H.; Nishikawa, Y.; Spontak, R. J.; Smith, S. D.; Agard, D. A.; Hashimoto, T. Direct Measurement of Interfacial Curvature Distributions in a Bicontinuous Block Copolymer Morphology. *Phys. Rev. Lett.* **2000**, 84, 518-521.
  18. Matsen, M. W.; Bates, F. S. Origins of Complex Self-Assembly in Block Copolymers. *Macromolecules* **1996**, 29, 7641-7644.
  19. Matsen, M. W.; Bates, F. S. Block copolymer microstructures in the intermediate-segregation regime. *J. Chem. Phys.* **1997**, 106, 2436-2448.
  20. Matsen, M. W.; Bates, F. S. Origins of Complex Self-Assembly in Block Copolymers. *Macromolecules* **1996**, 29, 7641-7644.
  21. Matsen, M. W. Gyroid versus double-diamond in ABC triblock copolymer melts. *J. Chem. Phys.* **1998**, 108, 785-796.
  22. Matsen, M. W. Phase Behavior of Block Copolymer Homopolymer Blend. *Macromolecules* **1995**, 28, 5765-5773.785-796.
  23. Padmanabhan, P.; Martinez-Veracoechea, F.J.; Escobedo, F. A. Computation of Free Energies of Cubic Bicontinuous Phases for Blends of Diblock Copolymer and Selective Homopolymer. *Macromolecules* **2016**, 49, 5232-5243.
  24. Martinez-Veracoechea, F.J.; Escobedo, F. A. The Plumber's Nightmare Phase in Diblock Copolymer/Homopolymer Blends. A Self-Consistent Field Theory Study. *Macromolecules* **2009**, 42, 9058-9062.
  25. Dotera, T. Tricontinuous Cubic Structures in ABC/A/C Copolymer and Homopolymer Blends. *Phys. Rev. Lett.* **2002**, 89, 205502.
  26. Takagi, H.; Yamamoto, K.; Okamoto, S. Ordered-bicontinuous-double-diamond structure in block copolymer homopolymer blends. *Europhys. Lett.* **2015**, 110, 48003.
  27. Chu, C. Y.; Jiang, X.; Jinnai, H.; Pei, R. Y.; Lin, W. F.; Tsai, J. C.; Chen, H. L. Real-space evidence of the equilibrium ordered bicontinuous double diamond structure of a diblock copolymer. *Soft Matter* **2015**, 11, 1871-1876.
  28. Suzuki, J.; Furuya, M.; Iinuma, M.; Takano, A.; Matsushita, Y. Morphology of ABC Triblock Copolymer/Homopolymer Blend Systems. *J. Polym. Sci. B.* **2002**, 40, 1135-1141.
  29. Asai, Y.; Yamada, K.; Yamada, M.; Takano, A.; Matsushita, Y. Formation of Tetragonally-Packed Rectangular Cylinders from ABC Block Terpolymers Blends. *ACS Macro Letters* **2014**, 3, 166-169.
  30. Asai, Y.; Takano, A.; Matsushita, Y. Asymmetric Double Tetragonal Domain Packing from ABC Triblock Terpolymer Blends with Chain Length Difference. *Macromolecules* **2016**, 49, 6940-6946.

## Chapter 6

31. Asai, Y.; Takano, A.; Matsushita, Y. Creation of Cylindrical Morphologies with Extremely Large Oblong Unit Lattices from ABC Block Terpolymers. *Macromolecules* **2015**, *48*, 1538-1542.
32. Lai, C.; Loo, Y-L.; Register, R. A.; Adamson, D. H. Dynamics of a Thermoreversible Transition between Cylindrical and Hexagonally Perforated Lamellar Mesophases. *Macromolecules* **2005**, *38*, 7098-7104.
33. Bailey, T. S.; Hardy, C. M.; Epps, T. H.; Bates, F. S. A Noncubic Triply Periodic Network Morphology in Poly(isoprene-*b*-styrene-*b*-ethylene oxide) Triblock Copolymers. *Macromolecules* **2002**, *35*, 7007-7017.
34. Yushu, M.; Suzuki, J.; Seki, M. Surfaces of tricontinuous structure formed by an ABC triblock copolymer in bulk. *Physica B* **1998**, *248*, 238-242.

## CHAPTER 7

### Summary

In this thesis, the effects of composition distribution of ABC linear triblock terpolymer on the formation of periodic structures were systematically investigated by varying the degree of the distribution. Especially in the binary blend systems which have the extremely large distribution, exhibited many characteristic morphologies that have never been observed experimentally and predicted theoretically. The summaries of the findings of this theory are listed below.

In Chapter 1, general introduction for morphological studies of many types of block copolymers was given.

In Chapter 2, the synthetic procedures and the characterization technique were described. In addition, the principles of some analysis were explained.

In Chapter 3, effect of composition distribution of ISP linear triblock terpolymers on the creation of periodic structures was investigated. Five ISP triblock terpolymers with almost constant total molecular weights and center-block fraction, but with different compositions of end-blocks, were blended with various blend ratios. Combination of TEM, SAXS and 3D-TEM experiments revealed that rectangular-shaped rods with 4-fold symmetry were observed in binary equimolar mixtures of two ISP triblocks with the largest distribution. The new structure with nonconstant mean-curvature, could be formed due to the localization of component polymer chains along the domain interfaces.

In Chapter 4, the phase behavior of the binary blends of ISP triblock terpolymers with different chain lengths of the two end-blocks as a function of  $\phi_P/\phi_I$  was investigated. The two

## Chapter 7

characteristic cylindrical morphologies with new tiling patterns have been observed. The morphologies are characterized by two essential and common features: (1) domains with nonconstant shapes and sizes, (2) tiling patterns consisting of triangles and pentagons. The shape of a unit lattice changed and the unit lattice size was dramatically increased depending on  $\phi_P/\phi_I$ . Ultimately, oblong shape unit lattices were obtained, which can be considered as the pseudodecagonal phase. The present results have the potential that a decagonal quasicrystal could be found in the vicinity of this study.

In Chapter 5, morphology of binary blends of ISP triblocks with asymmetric chain lengths of two end-blocks was investigated. Although the sizes of I and P cylinders were highly asymmetric, co-arrayed tetragonally packed cylinders were obtained on a wide range of volume fractions. There are three specific features of the morphologies: (1) I cylinders were metamorphosed into rod domains; (2) the cross-sectional area ratio of I/P domain is qualitatively changed depending on the volume ratio of I/P, and (3) P phase was divided into cylindrical and spherical microdomains. The Asymmetric chain lengths of two end-blocks must lead to these new morphologies.

In Chapter 6, we extended the molecular design of “different chain length” to the cocontinuous structure composition region to achieve OTDD structure. By blending the two ISP triblock terpolymers with different chain lengths of the two end-blocks, the existence of OTDD structure was explicitly confirmed by TEM, SAXS and TEM tomography experiments. The different chain length may help to alleviate the free energy penalty of interfacial tension and stretching energy.

## List of Publications

1. **Yusuke, Asai.**; Kotaro, Yamada.; Mutsuhiko, Yamada.; Atsushi, Takano.; Yushu, Matsushita. Formation of Tetragonally-Packed Rectangular Cylinders from ABC Block Terpolymers Blends. *ACS Macro Letters* **2014**, 3, 166-169.
2. **Yusuke, Asai.**; Atsushi, Takano.; Yushu, Matsushita. Creation of Cylindrical Morphologies with Extremely Large Oblong Unit Lattices from ABC Block Terpolymer Blends. *Macromolecules* **2015**, 48, 1538-1542.
3. **Yusuke, Asai.**; Atsushi, Takano.; Yushu, Matsushita. Asymmetric Double Tetragonal Domain Packing from ABC Triblock Terpolymer Blends with Chain Length Difference. *Macromolecules* **2016**, 49, 6940-6946.
4. **Yusuke, Asai.**; Jiro Suzuki.; Yoshitaka, Aoyama.; Hideo, Nishioka.; Atsushi, Takano.; Yushu, Matsushita. Tricontinuous Double Diamond Networks from Binary Blends of ABC Triblock Terpolymers. *in preparation*.
5. **Yusuke, Asai.**; Atsushi, Takano.; Yushu, Matsushita. Reproducible Nanoporous Materials from Pyridine Ring-contained Block Copolymers via A Facile Method. *in preparation*.
6. Haruko, Miyase.; **Yusuke, Asai.**; Atsushi, Takano.; Yushu, Matsushita. Kaleidoscopic Tiling Patterns with Large Unit Cells from ABC Star-Shaped Terpolymer / Diblock Copolymer Blends with Hydrogen Bonding Interaction. *submitted*.
7. Madalyn R, Radlauer.; Christophe, Sinturel.; **Yusuke, Asai.**; Akash, Arora.; Frank S, Bates.; Kevin D, Dorfman.; Marc A, Hillmyer. Morphological consequences of frustration in ABC triblock polymers. *Macromolecules* **2017**, 50, 446-458.

## Acknowledgement

This thesis is based upon the result of work carried out between Jun 2013 and March 2017 under the guidance of Prof. Yushu Matsushita at the Department of Applied Chemistry, Graduate School of Engineering, Nagoya University.

First of all I would like to express my great gratitude and appreciation to my supervisor Prof. Yushu Matsushita (Department of Applied Chemistry, Graduate School of Engineering, Nagoya University) for his fruitful help and support through the Ph. D course. He gave me a lot of valuable opportunities including the research visit to University of Minnesota, the application for the scientific research fund and so on.

I also thank Prof. Masami Kamigaito (Department of Applied Chemistry, Graduate School of Engineering, Nagoya University) and Prof. Yuichi Masubuchi (Research Group on Physics of Rheology, Graduate School of Engineering, Nagoya University) for their kind suggestions and their care in serving as the dissertation committee. I greatly thank Associate Prof. Atsushi Takano for his help in synthesizing polymers and his fruitful discussion. Thanks to him, I got to meet all kinds of incredible people who inspired me. I also thank Assistant Prof. Noro for his kind help in research life. I am greatly indebted to my former advisor, Associate Prof. Daisuke Kawaguchi (Kyushu University) for his support, guide and patience. In my undergraduate and master's course, he always said to me "*let the data speak for themselves*". (This may be based on the phrase "*let the facts speak for themselves*" in *Science as a Vocation* written by Max Weber Gesamtausgabe.) I still recall the phrase whenever I face with a difficult, and it has driven me to pursue science at a higher level.

This thesis was also supported by many researchers in other research institutions. Many thanks to Associate Prof. Jiro Suzuki (KEK, J-PARC), Assistant Prof. Daichi Ida (Department of Polymer Chemistry, Kyoto University), Dr. Yoshitaka Aoyama (JEOL Ltd.), Hideo Nishioka (JEOL Ltd.), Tatsuo Hikage (High Intensity X-ray Diffraction Laboratory, Nagoya University), Ikuo Hayashi (Instrumental analysis factory, Nagoya University), Noboru Ohta (JASRI) and Noritaka Horii (SYSTEM IN FRONTIER Inc.) for all the valuable discussions and fruitful collaborations. I could not have done these works without their supports.

## Chapter 7

I would also love to thank Prof. Marc A. Hillmyer (University of Minnesota, USA) for the acceptance of my research visit and giving me the valuable opportunities. I am indebted to a number of my colleagues at University of Minnesota, especially to Madalyn Radlauer (University of Minnesota, USA), Prof. Christophe Sinturel (Universite d'Orleans, France), who always helped me and I greatly respect their sincere efforts to science.

My study was financially supported by the Program for Leading Graduate Schools at Nagoya University entitled “Integrative Graduate Education and Research Program in Green Natural Sciences,” and by JSPS Research Fellowships for Young Scientists (No. 15J04554). I am thankful for all the supports.

I cannot miss the opportunity to thank the Matsushita lab members, especially Arisa Asano, Yuki Kobayashi, Hiroki Sawaki, Satoru Matsushima and Akiko Minami, who are in the same year as. They always influenced me positively and gave me a great working atmosphere in the lab and daily life.

Finally, I would like to express my gratitude to my family.

Yusuke Asai

淺井 裕介